Alma Mater Studiorum – Università di Bologna

DOTTORATO DI RICERCA IN

Ingegneria Civile, Chimica, Ambientale e dei Materiali

Ciclo XXXI

Settore Concorsuale: 08/A1

Settore Scientifico Disciplinare: ICAR/01

SUSTAINABLE GROUNDWATER MANAGEMENT BASED ON PROBABILISTIC RISK ANALYSIS

Presentata da: Ilaria Lauriola

Coordinatore Dottorato	**Supervisore**
Prof. Luca Vittuari	**Prof.ssa Valentina Ciriello**

Co-Supervisori

Prof. Vittorio Di Federico
Prof. Daniel M. Tartakovsky

Esame finale anno 2019

Contents

Abstract

Risk assessment related to the qualitative/quantitative status of groundwater is a controversial issue, compared to which it is difficult to identify a univocal and exhaustive approach. A key factor for assessing the vulnerability of an aquifer is the analysis of the natural renewal capacity associated with the quantity of available resource and compared to the overall water demand. In general, groundwater recharge is a complex process to analyze because it varies in space and time, and may be severely affected by future scenarios related to climate change and population dynamics. At the same time, local and diffuse contaminations may threaten the quality of groundwater availability with respect to the standards provided to the different uses and represent a critical environmental issue.

Consequently, even if there are many studies dealing with groundwater vulnerability, the definition of a shared approach capable of (i) exhaustively describing in an integrated framework the phenomena occuring in different hydrogeological and climatic contexts and (ii) considering all the significant uncertainties according to a stochastic method, has not yet been achieved. In order to address these points, this thesis suggest an innovative methodological framework in which application of

uncertainty quantification is applied both to parametric uncertainty, which is relevant to subsurface flow and transport processes, and to the projections of climate change scenarios. In support of this, an algorithm is applied and further developed based on metamodelling techniques to accelerate risk and global sensitivity analysis. The algorithm is applied to different case studies in order to provide an insight on some of the main quantitative/qualitative processes that affect groundwater status, leading to potentially risk conditions. Ultimately, results presented in this work lay the basis for the computation of indicators which can be used for the assessment of the vulnerability of groundwater at different scales, in accordance with the requirements of current European and National Regulations on water resources.

Sommario

La valutazione del rischio relativo allo stato qualitativo/quantitativo delle acque sotterranee è una questione controversa, rispetto alla quale è difficile identificare un approccio univoco ed esaustivo. Un fattore chiave per la valutazione della vulnerabilità di un sistema acquifero è senz'altro rappresentato dall'analisi della capacità di rinnovamento associata alla risorsa in esso inclusa rispetto ai prelievi agenti sul sistema. In generale, la ricarica delle acque sotterranee è un processo complesso da analizzare perché varia nello spazio e nel tempo e può essere seriamente compromesso dagli scenari futuri relativi ai cambiamenti climatici e alle dinamiche demografiche. Di conseguenza, anche se molti sono gli studi condotti a riguardo, non si è ancora giunti alla definizione di una metodologia riconosciuta, capace di (i) descrivere in maniera esaustiva e integrata i fenomeni presenti nei diversi contesti idrogeologici e climatici e di (ii) contemplare tutte le significative incertezze in gioco secondo un approccio di tipo stocastico. Nella seguente tesi si propone, come aspetto innovativo del progetto di ricerca, l'applicazione della quantificazione dell'incertezza sia per l'incertezza parametrica, che è rilevante nei processi di flusso e trasporto sotterranei, sia per la trattazione delle proiezioni di scenari di cambiamento

climatico. A supporto di ciò, un algoritmo basato su tecniche di meta-modellazione viene applicato e ulteriormente sviluppato per accelerare l'analisi di rischio e di sensitività globale. L'algoritmo verrà applicato ai diversi casi di studio al fine di fornire una panoramica su alcuni dei principali processi quantitativi/qualitativi che influenzano e possono compromettere lo stato ambientale delle acque sotterranee. In definitiva, i risultati presentati in questo lavoro potranno essere di ausilio per la formulazione di indicatori che possono essere utilizzati per la valutazione della vulnerabilità della risorsa sotterranea alle diverse scale, in accordo con quanto richiesto dalle vigenti norme europee e nazionali in materia di acque.

Chapter 1

Introduction

Sommario

Il tema della gestione dei corpi idrici sotterranei, in un'ottica di sostenibilità, è un tema alquanto complesso, specialmente se inquadrato all'interno dell'analisi di scenari futuri di cambiamento climatico e pressioni antropiche. In generale, lo studio di scenari futuri va inquadrato all'interno di un'analisi di rischio, come indicato peraltro dalla normativa Europea di riferimento. Tuttavia, ad oggi, non esistono approcci condivisi e generalizzabili, capaci di rispondere a questa esigenza.

In questo contesto, il presente capitolo fornisce un breve richiamo della Direttiva Europea in materia di risorse idriche sotterranee, e di quanto in esso stabilito in termini di target e procedure. A ciò fa seguito una breve descrizione di alcuni indicatori di vulnerabilità presenti in letteratura e un'analisi critica dei problemi aperti connessi allo stato

dell'arte e di come questa tesi si propone di superarli.

1.1   Water Framework Directive

The Water Framework Directive 2000/60/EC (WFD) is a comprehensive set of rules defining environmental standards for all waters in Europe. The WFD requires a sustainable and integrated river basin management which includes objectives and a comprehensive program of severe measures whose adoption is an open challenge for all the countries, institutions and stakeholders involved. In particular, the WFD establishes the final goal of achieving a good qualitative and quantitative status for all water bodies (EP, 2000). The working groups supporting the WFD implementation policies (WFD Common Implementation Strategy Groups) have developed specific guidelines for the pratical implementation of the WFD and the Groundwater Directive 2006/118/EC (GWD) (e.g. EC, 2003; EP, 2006; EC, 2007c; EC, 2007b; EC, 2007a; EC, 2009; EC, 2010).
In the following, the main content of guidelines No. 18 and No. 26 on groundwater status assessment and risk assessment, respectively, are briefly summarized.

1.1.1   Groundwater status assessment

With reference to groundwater bodies, the program described in Guidance Document No. 18 (EC, 2009) defines the operational tests required for the verification of conditions established by the WFD and GWD, aimed at determining the quantitative and qualitative status. The management of groundwater bodies is divided into cycles of 6

years, and is practically realized through the River Basin Management Plans (RBMPs). Status assessment is undertaken at the end of each RBMP to verify the efficiency of the program of measures included in it.

As shown in Figure 1.1, the assessment of good status for groundwater bodies involves meeting a series of classification tests, four tests for the quantitative status and five for the qualitative one. In accordance with Document No.18, a good quantitative status occurs when the groundwater body is not subjected to withdrawals for an amount of resource higher than its natural renewal capacity. Moreover, even if this condition is satisfied, a good status is realized only when changes in the piezometric level, due to anthropic factors, do not quantitatively compromise surface water bodies and terrestrial ecosystems depending on the groundwater body. Lastly, it is necessary that the same level variations do not cause saline intrusion or other contamination problems that would decrease freshwater availability.

Regarding good qualitative status, it occurs when (i) concentrations of pollutants compared to threshold and background level values, reveal that contamination processes due to human activities are not present and (ii) there is no evidence of intrusions. Moreover, it must be verified no transfers of contaminants between the groundwater body and the surface water bodies and terrestrial ecosystems depending on it; finally, drinking water quality thresholds for human consumption must be observed.

Only when all these conditions are satisfied, then the status is classifiable as good under the WFD.
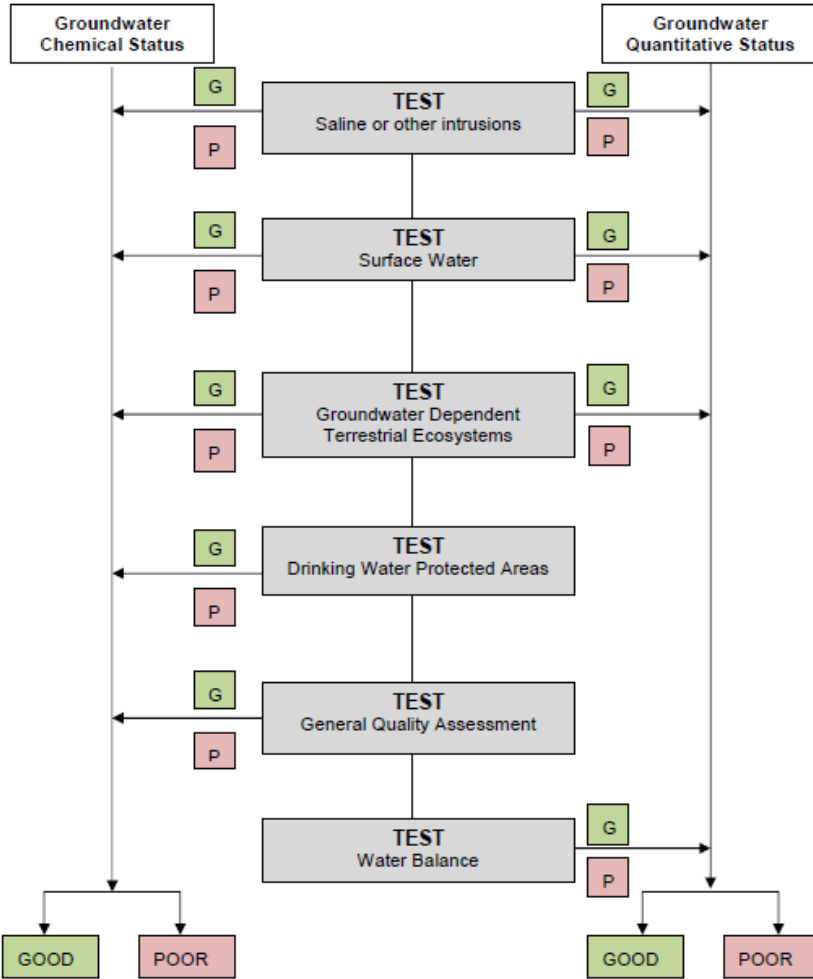
Figure 1.1: Classification tests for assessing groundwater status in accordance with EC, 2009.

1.1.2 Groundwater risk assessment

Risk assessment is undertaken at the beginning of each RBMP to identify pressures insisting on groundwater body and predict the status at the end of the cycle. In order to prevent the non-achievement of a good status, environmental agencies are called to develop remediation measures and to improve planning of monitoring actions. Risk assessment is a complex phase as it requires integrated analysis of the groundwater body at different scales, from the site scale (local) up to the basin scale. Furthermore, such assessment is plagued by different sources of uncertainty (in data and models and due to the lack of knowledge on heterogeneous subsurface environment).
To assist environmental agencies in this phase, Guidance Document No.26 (EC, 2010) suggests the use of groundwater conceptual models as useful tools to conduct risk and status assessment. Specifically, a preliminary conceptualization can be used to (i) provide a reliable basis for simulating and predicting processes in groundwater with mathematical or numerical models (ii) plan monitoring campaigns and remediation actions and (iii) assess the effects of the selected strategies.

1.2 Water Indices

The potential consequences of water scarcity have pushed the european governance and scientific community towards the development of strategies aimed at the sustainable management of water resources. The environmental and anthropic impacts on water resources are generally divided into: (i) impacts related to the quantitative aspect and (ii) impacts related to the qualitative aspect. However, as highlighted

by Guidance Documents, the two aspects are often complementary and therefore would require an integrated analysis to assess water vulnerability. In the literature, several studies are focused on the evaluation of groundwater status, but it results still difficult to identify a comprehensive and generalizable methodology (Wada et al., 2010; Gleeson et al., 2012; Kounina et al., 2013) in line with the directives and able to account for predictive uncertainty.

Water Indices are often used as descriptors that provide information on the use of water resources and to support their management. For example, a category of indices considers the exhaustion of the resource as directly related to the degradation of ecosystems (Smakhtin, Revenga, and Döll, 2004). Other indices aim to represent the vulnerability of water resources by combining geospatial tools and climatic variations (Vörösmarty et al., 2000; Vörösmarty et al., 2005). There are also indices that relate the extent of the withdrawals with water availability, at the basin scale and/or at national scale (Alcamo, Henrichs, and Rösch, 2000); others consider the availability of the resource as linked to the quantity of the same that is returned to the system (Boulay et al., 2011).

Generally, the indices proposed in the literature are lacking in terms of integrated qualitative and quantitative evaluations regarding the availability of the resource. Moreover, the evaluations based on these indices are often conducted through global budgets where the amounts of water coming from the subsoil are not distinguished from the superficial ones. Therefore, despite the primary importance of groundwater, these instruments are not capable of assessing the vulnerability associated with subsurface water bodies. In addition, the indices are usually

associated with average conditions and do not account for predictive uncertainty.

1.3 Final remarks

In this thesis, a set of models and tools, belonging to an integrated stochastic framework, are employed and developed in order to facilitate the assessment and management of groundwater bodies, while overcoming the limits described above.

The methodological framework, able to account for predictive uncertainty, is described in Chapter 2. Subsequently, a set of case studies referred to the vulnerability of groundwater resources at different scales are analyzed in order to:

   i provide an insight on some of the most common mechanisms of groundwater depletion;

  ii show how these mechanisms can be potentially aggregate into a probabilistic risk analysis framework to quantify the overall vulnerability associated with a given groundwater body;

 iii show the importance to account for predictive uncertainty when assessing groundwater status especially under future scenarios;

 iv provide approaches able to incorporate uncertainty quantification methods and implement the goals of the European Directives at the same time;

  v show how it is possible to define vulnerability indicators on the basis of these approaches.

Chapter 2

Materials and Methods

Sommario

In questo capitolo viene introdotto il problema della quantificazione dell'incertezza parametrica, particolarmente significativa nell'ambito dell'idrologia sotterranea ed, in generale, nella trattazione delle tematiche di flusso e trasporto nei mezzi porosi naturali.

Ai fini di una migliore comprensione dei fenomeni in gioco, strumenti quali l'Analisi di Rischio e l'Analisi di Sensitivitá Globale svolgono un ruolo fondamentale per la quantificazione e la caratterizzazione dell'incertezza associata alle previsioni. Usualmente tali strumenti si avvalgono di metodi di simulazioni onerosi dal punto di vista computazionale, uno fra tutti, il metodo Monte Carlo, da cui sono state derivate in seguito tecniche di campionamento intelligenti, allo scopo di diminuire il numero di simulazioni necessarie per arrivare a convergenza.

Nota la complessitá che accompagna questo tipo di analisi, sono state individuate alternative adeguate capaci di coniugare un elevato grado di precisione con tempi di calcolo alquanto piú ridotti. Da questo presupposto sono nate tecniche di riduzione dei modelli fra le quali, particolare interesse ha suscitato il metodo dell'espansione in Caos Polinomiale, che consente di disporre di un modello surrogato in forma polinomiale, ottenuto dalla proiezione del modello di partenza in uno spazio probabilistico opportunamente individuato. Adottando questa tecnica si evita di dover ricorrere alla sostituzione del modello originale con un modello semplificato che, pur mantenendo le caratteristiche essenziali del problema, non ne rappresenta le dinamiche esatte; piuttosto si riesce ad ottenere un'ottima approssimazione del modello di partenza in una forma che garantisce tempi di calcolo trascurabili. Questo capitolo ripercorrerà, dunque, i concetti chiave legati alla quantificazione e caraterizzazione dell'incertezza parametrica e descriverà la tecnica dell'espansione in Caos Polinomiale, contribuendo a definire l'inquadramento teorico sul quale è stato sviluppato il presente lavoro di tesi.

2.1   Uncertainty Quantification in subsurface Hydrology

In the context of subsurface hydrology, accuracy of prediction is generally affected by: (i) heterogeneity characterizing the subsurface environment, (ii) the lack of adequate site monitoring, (iii) the inadequacy of models used to mimic relevant processes (Tartakovsky, 2007). Typically, the nature of uncertainty is dual because it can derive both

from the lack of an exhaustive knowledge about the dynamics of real systems (epistemic uncertainty), and from the randomness of physical phenomena (aleatory uncertainty) (Bedford and Cooke, 2006). In the following, the focus is on parametric uncertainty even if some concepts can be employed also to treat model uncertainty.

Because of the high spatial variability of geological properties in the subsurface environment and the scarcity of measures, key hydrogeological parameters (useful to describe the properties of the medium in the equivalent continuous approach) can not be accurately characterized and therefore must be modeled as random variables or random fields. These parameters significantly influence groundwater flow and transport, thus making these processes affected by uncertainty as well, while the equations describing them assume a stochastic character (Rubin, 2003). In this context, the interest of the scientific community has focused mainly on developing methods of analysis to quantify and characterize parametric uncertainty. Specifically, these methods try (i) to study the way in which the uncertainty in model input parameters is propagated towards the output variables, (ii) to capture which sources of uncertainty mainly influence the response of the models, (iii) and finally to derive the probability density function associated with the model response. Note that these methods can be properly applied also with regards to those parameters/variables affected by uncertainty associated with the prediction of future scenarios (Linkov and Burmistrov, 2003).

2.2   Probabilistic Risk Analysis (PRA)

A valid tool for quantifying uncertainty is Risk Analysis (RA), since the concept of uncertainty is closely linked to that of "risk" and "hazard" (Tartakovsky, 2013). In literature there is a multitude of its applications to many sectors (construction, energy, environment, chemical processing, aerospace) (Bedford and Cooke, 2006).

In recent years, this methodology has received increasing attention into the regulatory framework of the government agencies, (e.g.EPA, 2000; NRC, 2010; NRC, 1997; EC, 2003) where deterministic approaches have been replaced by probabilistic ones, thus leading to the so called Probabilistic Risk Analysis which can be grouped into two macro families: unstructured PRA and structured PRA.

2.2.1   Unstructured PRA

In the unstructured PRA category the most used method is the Monte Carlo method (EPA, 1997), which allows to solve an input-output model in probabilistic terms. In fact, by attributing a probability distribution function to each input, instead of a deterministic value, it is possible to obtain a similar function for the output of the model that is n-times deterministically calculated (Haas, Anotai, and Engelbrecht, 1996; Skaggs and Barry, 1997; Troldborg et al., 2008; Zhang, Vouzis, and Sahinidis, 2011). However, the computational cost associated with this type of simulation is often unfordable, especially when the model is numerically complex and/or characterized by a large number of uncertain parameters (Lahkim and Garcia, 1999). Therefore, in order to reduce the number of simulations and

the computational burden to achieve convergence, several alternative smart sampling techniques have been proposed, such as quasi MCS approaches, e.g. Latin hypercube sampling ,(Lahkim, Garcia, and Nuckols, 1999), or approaches which identify "critical realizations", (e.g. Bayer, Burger, and Finkel, 2008; Bayer, de Paly, and Burger, 2010). As described below, when the computational cost remains too high to be acceptable, a viable solution is provided by metamodeling techniques.

2.2.2 Structured PRA

Structured PRA approach has been recently introduced in hydrogeology to deal with the risk related to groundwater contamination e.g.(Kessler and McGuire, 1999; Bolster et al., 2009; Rodak and Silliman, 2011). This is a powerful tool for the rigorous quantification of uncertainties inherent in predictions of subsurface flow and transport. Typically, a structured PRA starts by identifying relevant components influencing the system state and proceeds by using uncertainty quantification techniques to estimate probabilities of occurrence of undesirable events associated with these components (Jurado et al., 2012). This is practically realized by means of Fault Tree Analysis (FTA), which is a deductive approach that depicts the functional cause-effect relations between the events through the realization of a "tree" logical scheme (Vesely and Roberts, 1981). In the FTA scheme, probability of basic events can be estimated with different degrees of complexity, e.g. by resorting to the judgment of an expert, by means of statistical techniques such as Kernel Density Estimation (KDE) (Moon, Rajagopalan, and Lall, 1995), or by applying uncertainty quantifica-

tion to selected interpretative models. These include, in particular: (i) physically based models (analytical, numerical), (ii) data-driven models (neural networks, traditional statistical tools), and (iii) "hybrid" models resulting from the merging of previous approaches (Di, Yang, and Wang, 2014).

Once the interpretative model has been established, the probability of occurrence of different scenarios of interest can be computed by means of Monte Carlo simulations (or similar), or in case of highly complex formulations, it is possible to apply innovative metamodeling techniques aimed at reducing the cost of the analysis (e.g. Ciriello et al., 2013c).

2.3   Global Sensitivity Analysis (GSA)

In the last years, Global Sensitivity Analysis (GSA) has been increasingly employed to analyze the influence of random parameters on the uncertainty of model responses. The main idea of GSA is to jointly consider the variability of all the uncertain input parameters to overcome the limits imposed by local approaches, typically performed by considering one parameter at a time, relying on the assumptions of model linearity. As such, GSA provides a complete description of how the uncertainty in the model response can be apportioned to the different parameters and their interactions (Saltelli, Tarantola, and Campolongo, 2000, and reference therein). This is critical to identify which sources of uncertainty need additional data collection to narrow the degree of uncertainty in the response. In spite of the onerous computational cost, GSA represents a necessary component of a

quality risk assessment report and has shown to provide relevant information to support model calibration and selection (Ciriello et al., 2013a; Ciriello et al., 2015).

2.3.1 Variance-based GSA

Variance-based GSA is aimed at defining the relevance of each uncertain model parameter based on the contribution provided to the variance of model response. In this context, the Sobol indices (Sobol', 1993) are widely used as sensitivity metrics as they do not require any assumption of model linearity. Their definition relies on the ANOVA decomposition (Archer, Saltelli, and Sobol, 1997).

Let's consider a model function $y = f(x)$, where x is a vector collecting n independent random parameters. If $f(x)$ belongs to the space of square-integrable functions, the total variance, V, of model response can be computed as follows:

$$V = \int f^2(x)\, dx - f_0^2 = \sum_{s=1}^{n} \sum_{i_1 < ... < i_s}^{n} V_{i_1,...,i_s}, \quad V_{i_1,...,i_s} = \int f_{i_1,...,i_s}^2\, dx_{i_1}...dx_{i_s},$$

$$(2.1)$$

where $V_{i_1,...,i_s}$ is the generic partial variance due to the contribution of a given subset of model parameters. The correspondent Sobol index is given by (*Sobol*, 1993):

$$S_{i_1,...,i_s} = \frac{V_{i_1,...,i_s}}{V}.$$

$$(2.2)$$

Indices defined by (2.2) sum up to unity.

A complete variance-based GSA requires the numerical estimation of 2^n integrals of the kind reported in (2.1). This is typically performed

in a Monte Carlo framework (Sobol', 2001). Nevertheless, also in this case, the computational cost can be prohibitive when the model is complex and the number of uncertain parameters is large (e.g. Sudret, 2008).

2.3.2   Distribution-based GSA

Variance of model response does not provide a complete information on output variability. In order to analyze the influence of uncertain input parameters on the entire distribution of model response, it is necessary to define other sensitivity metrics not dependent on a specific moment. To this end, Borgonovo (Borgonovo, 2007) introduced a global sensitivity indicator that reads as follow

$$\delta_i = \frac{1}{2} E\left[s\left(X_i\right)\right] = \int_{D_{X_i}} f_{X_i}\left(x_i\right) s\left(X_i\right) dx_i, \qquad (2.3)$$

where $s\left(X_i\right)$ represents the shift between $f_Y\left(y\right)$ and $f_{Y|X_i}\left(y\right)$:

$$s\left(X_i\right) = \int_{D_Y} \left|f_Y\left(y\right) - f_{Y|X_i}\left(y\right)\right| dy. \qquad (2.4)$$

The metric δ_i, of a given parameter x_i, may assume a value within the range $[0, 1]$, by definition; at the same time, $\delta_{1,2,...,M} = 1$ (see Borgonovo, 2007, for more details).
Computation of integrals in (2.3) and (2.4) may be conveniently performed relying on the quadrature rules. Nevertheless, the number of model runs required to this end is significantly high and the resulting computational cost increases, as for variance-based approaches, with the number of parameters and model complexity.

2.4 Model reduction techniques

Model reduction techniques provide an alternative to overcome the computational limitations in the develompment of PRA and GSA for complex models. Metamodels typically relies on the capability of approximating a more complex mathematical conceptualization (or "simulator") to account for parameter uncertainty and determine the way in which this propagates towards the quantity of interest. This is critical when the computational time associated with the simulator renders it unsuitable to perform time consuming analysis (e.g. Ciriello et al., 2013c; Ciriello et al., 2017). Among metamodels, the Polynomial Chaos Expansion (PCE) (Wiener, 1938; Ghanem and Spanos, 1991) has received particular attention in the last decade (e.g. Laloy et al., 2013; Ashraf, Oladyshkin, and Nowak, 2013; Ciriello et al., 2013a; Deman et al., 2015; Marrel, Perot, and Mottet, 2015; Ciriello et al., 2015). In particular, PCE has been widely used to estimate variance-based sensitivity metrics such as the Sobol indices (Sobol', 1993; Archer, Saltelli, and Sobol, 1997; Sobol', 2001; Sudret, 2008). Nevertheless, there are a few examples in literature on the use of PCE to perform moment independent GSA (Rajabi, Ataie-Ashtiani, and Simmons, 2015).

2.4.1 Polynomial Chaos Expansion (PCE)

Let's consider a response y provided by a simulator $f(\cdot)$ depending on a set of M input parameters collected in $\mathbf{x}$. If these parameters are affected by uncertainty, $f(\cdot)$ can be defined a stochastic model. Following the Polynomial Chaos theory and assuming parameters to be

independent, if variance of y is finite, a spectral representation of the response surface can be obtained by means of a basis of multivariate polynomials (for more details, Wiener, 1938; Ghanem and Spanos, 1991; Xiu and Karniadakis, 2002). The Polynomial Chaos Expansion (PCE) $\hat{y}$ reads as follows:

$$\hat{y} = \sum_{\mathbf{a} \in N^M} s_{\mathbf{a}} \Psi_{\mathbf{a}}(\mathbf{x}) \tag{2.5}$$

where multi–indices $\mathbf{a} \in N^M, \mathbf{a} = \{a_1, ..., a_M\}$ are associated with the multivariate polynomial $\Psi_{\mathbf{a}}(\mathbf{x})$ of degree $|\mathbf{a}| = \sum_{i=1}^{M} a_i$, given by

$$\Psi_{\mathbf{a}}(\mathbf{x}) = \prod_{i=1}^{M} \Gamma_{a_i}^{(i)}(x_i). \tag{2.6}$$

Polynomials $\Gamma_k^{(i)}, k \in N$, respect condition of orthogonality $\left\langle \Gamma_{k_1}^{(i)}, \Gamma_{k_2}^{(i)} \right\rangle = a_j^i \delta_{k_1 k_2}$ and are properly selected based on the input *pdf*s.

Coefficients $s_{\mathbf{a}}$ in (2.5) represent the deterministic coordinates of the spectral decomposition, while multivariate polynomials, defined in (2.6), constitute a orthonormal basis with respect to the joint input *pdf*, i.e. $E[\Psi_{\mathbf{a}}(\mathbf{x}), \Psi_{\mathbf{b}}(\mathbf{x})] = \delta_{\mathbf{ab}}$ (Xiu and Karniadakis, 2002).

The PCE can be rewritten as

$$\hat{y} = \sum_{j=0}^{P-1} s_j \Psi_j(\mathbf{x}) \tag{2.7}$$

where $P = \frac{(M+p)!}{M!p!}$ and p the maximum degree of the expansion, i.e. $|\mathbf{a}| \leqslant p, \forall \mathbf{a} \in N^M$.

Table 2.1 shows an example of the terms involved in a second-order Legendre PCE in case of 3 uniformly distributed uncertain input parameters.

Table 2.1: Terms of the PCE: case of Legendre Polynomials, $M = 3$ and $p = 2$.

$\mathbf{a}$	$|\mathbf{a}|$	j	$\Psi_{\mathbf{a}}(\mathbf{x})$
(000)	0	0	1
(100)	1	1	x_1
(010)	1	2	x_2
(001)	1	3	x_3
(200)	2	4	$\frac{1}{2}\left(3x_1^2 - 1\right)$
(110)	2	5	$x_1 x_2$
(101)	2	6	$x_1 x_3$
(020)	2	7	$\frac{1}{2}\left(3x_2^2 - 1\right)$
(011)	2	8	$x_2 x_3$
(002)	2	9	$\frac{1}{2}\left(3x_3^2 - 1\right)$

2.4.2 Computation of PCE coefficients

Among non-intrusive methods for the computation of PCE coefficients, a regression-based approach, comparable with the widely used stochastic response surface method (SRSM), can be employed to minimize the variance of a suitable residual, $\varepsilon = |\hat{y} - y|$ with respect to the vector of the unknown coefficients (Sudret, 2008).
The optimum set of regression points in the (random) parameter space is determined on the basis of the same arguments adopted for integral estimation through Gaussian quadrature. To this end, the Stochastic Collocation Method (SCM) (Webster, Tatang, and McRae, 1996; Huang, Mahadevan, and Rebba, 2007) employs the roots of the polynomial of one order higher than p, to assure proper sampling of the

region associated with the largest probability according to the distributions of input parameters.

2.5   Algorithm development

This section is devoted to the presentation of a computational framework based on PCE to efficiently compute moment-indipendent indices; there are very few examples of this application in literature (Rajabi, Ataie-Ashtiani, and Simmons, 2015). A suite of routines to compute distribution-based GSA has been added into an existed MatLab Toolbox that provide stochastic analysis via PCE for variance-based GSA and PRA(Ciriello, 2013).

2.5.1   Analytic update of PCE coefficients

For the sake of simplicity, the Borgonovo index (Borgonovo, 2007) is used as distribution-based metric. As shown in Section (2.3.2), it is made by an internal integral representing the shift between the pdf of the response when all the parameters are uncertain and when the actual parameter is fixed. The external integral is over the domain of variability of the actual parameters.

If one of the input parameters, x_i, is set to a given value, $\bar{x}_i$, approximation of the response surface, provided by PCE (2.7), changes as follows:

$$\hat{y} = \sum_{j=0}^{P'-1} q_j \Psi_j \left(\mathbf{x}_{-i} \right) \tag{2.8}$$

where number of terms decreases to $P' = \frac{(M-1+p)!}{(M-1)!p!}$ and $\mathbf{x}_{-i}$ is the vector of input parameters excluding x_i. Computation of coefficients q_j requires a given number of evaluations of $f(\cdot)$ as described in the Section (2.4.2). Alternatively, it is possible to update value of coefficients s_j in (2.7), avoiding additional full model runs. Let's denote with s_0' the updated zero-order coefficient; it is given by

$$s_0' = s_0 + \left[\sum_{\mathbf{a} \in N^M | a_k \neq 0 \Leftrightarrow k=i} s_{\mathbf{a}} \Psi_{\mathbf{a}}(\mathbf{x}) \right]_{x_i = \bar{x}_i} \tag{2.9}$$

while the other coefficients result

$$if \; a_i \neq 0 \Rightarrow s_{\mathbf{a}}' = 0 \tag{2.10}$$

$$if \; a_i = 0 \Rightarrow s_{\mathbf{a}}' = s_{\mathbf{a}} + \left[\sum_{\mathbf{b} \in N^M | b_i \neq 0, b_{k \neq i} = a_k} s_{\mathbf{b}} \Gamma_{b_i}^{(i)}(\mathbf{x}) \right]_{x_i = \bar{x}_i} \tag{2.11}$$

Table 2.2 shows the implementation of the previous equations based on the example reported in Table 2.1, when x_1 is fixed.

2.5.2 Algorithm workflow

The main steps of the approach are summarised in Figure 2.1. The algorithm computes both the integrals, described in Section 2.5.1, through Gaussian Quadrature (GQ), while the pdfs are obtained by applying Kernel Density Estimation (KDE) on PCE metamodels, whose coefficients are automatically updated at each value assigned to the actual parameter. It is possible to observe that the only relevant computational time is required by the initial definition of the PCE providing the approximation, $\hat{y}$, of the model response. Subsequently, all the

Table 2.2: Automatic update of PCE coefficients: case of 3.1, x_1 is fixed.

a	eq. of s_j'	s_j'
(000)	(2.9)	$s_0 + s_1\bar{x}_1 + s_4\frac{1}{2}\left(3\bar{x}_1^2 - 1\right)$
(100)	(2.10)	0
(010)	(2.11)	$s_2 + s_5\bar{x}_1$
(001)	(2.11)	$s_3 + s_6\bar{x}_1$
(200)	(2.10)	0
(110)	(2.10)	0
(101)	(2.10)	0
(020)	(2.11)	s_7
(011)	(2.11)	s_8
(002)	(2.11)	s_9

other steps consists in analytical post-processing or in efficient computational schemes (e.g., GQ, KDE) that are associated with a virtually negligible computational cost, when applied to the PCE approximation. This original strategy sensibly reduces the computational cost of analysis.

2.5.3   Application example

We apply the methodology to the computation of a drought index, the Reconnaissance Drought Index (RDI) (Tsakiris and Vangelis, 2005; Tsakiris, Pangalou, and Vangelis, 2007) which is widely used in literature since it is strictly connected to the Aridity Index (UNESCO,
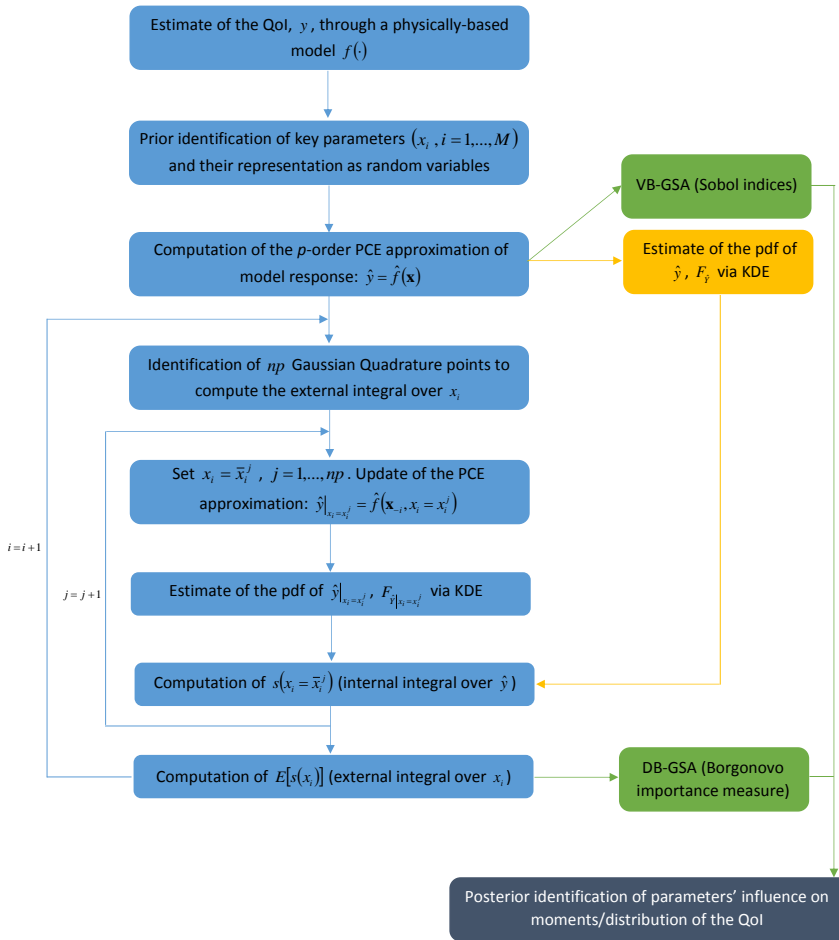
Figure 2.1: Approach to perform VB and DB-GSA via PCE.

1979) and it is defined as follows:

$$\alpha_0^i = \frac{\sum_{j=1}^{12} P_{ij}}{\sum_{j=1}^{12} PET_{ij}}, \tag{2.12}$$

where P_{ij} and PET_{ij} are the average precipitation and potential evapotranspiration for the $j-$th month of the $i-$th year, respectively; $i = 1 \div n$ and $j = 1 \div 12$.

Based on (2.12), a correspondent normalized index can be derived as:

$$RDI_n^i = \frac{\alpha_0^i}{\bar{\alpha}_0}, \tag{2.13}$$

where $\bar{\alpha}_0$ is the arithmetic mean of α_0 values calculated for n years of data.

We focus on the Emilia-Romagna Region (Italy) and we select 25 stations uniformly distributed in space as depicted in Figure 2.2. Characteristics of the selected stations are summarized in Table 3.2.

At the selected stations, we collect monthly averaged data of daily precipitation and minimum/maximum temperature for a 30-years reference period $1971 - 2000$ (Antolini et al., 2017). Hereinafter, these data will be referred to as P_{ijk}, $T_{max_{ijk}}$, and $T_{min_{ijk}}$, where $i = 1 \div 30$ indicates the year, $j = 1 \div 12$ the month, and $k = 1 \div 25$ the station, following the order provided in Table 3.2. Based on temperature data, we estimate $T_{m_{ijk}} = 0.5(T_{max_{ijk}} + T_{min_{ijk}})$ and $\Delta T_{ijk} = T_{max_{ijk}} - T_{min_{ijk}}$.

Potential evapotranspiration PET_{ijk} is then computed following Hargreaves:

$$PET_{ijk} = 0.0135 R_{s_{ijk}} (T_{m_{ijk}} + 17.8), \tag{2.14}$$

where the solar radiation is estimate according to Hargreaves and

Table 2.3: Characteristics of the selected stations.

k	Name	Altitude (m slm)	Latitude (°)
1	Villanova sull'Arda	40	45.03
2	Sarsina	247	43.89
3	Modena urbana	73	44.66
4	Bologna urbana	78	44.50
5	Ostellato	0	44.71
6	Parma urbana	79	44.80
7	Rimini urbana	16	44.06
8	Forli urbana	51	44.22
9	Loiano	741	44.26
10	Porretta terme	352	44.15
11	Idrovora di Guagnino	1	44.69
12	Classe	2	44.37
13	Finale Emilia	16	44.82
14	Castellana Groppo	434	44.81
15	Boschi d'Aveto diga	616	44.59
16	Bobbio	270	44.76
17	Bosco centrale	902	44.44
18	Ligonchio centrale	900	44.32
19	Pavullo	678	44.32
20	Codigoro	2	44.84
21	Malalbergo	12	44.72
22	Imola	42	44.35
23	San Cassiano	230	44.15
24	Campigna	1068	43.87
25	Cesenatico	2	44.21
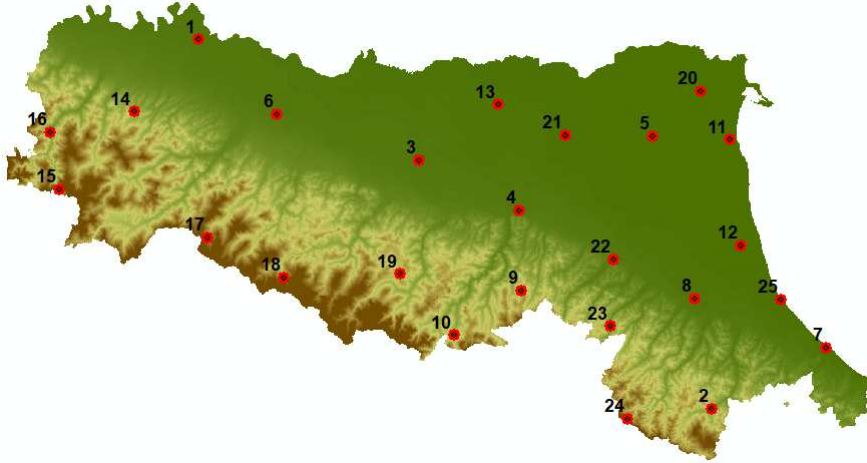
Figure 2.2: Spatial distribution of the stations within the Emilia-Romagna Region.

Samani (Hargreaves and Samani, 1982) as:

$$R_{s_{ijk}} = R_{a_{ijk}} K_T \left(\Delta T_{ijk} \right)^{0.5} . \tag{2.15}$$

In (2.15), R_a is the extraterrestrial radiation (Allen et al., 1998), and K_T is an empirical coefficient whose value typically varies within 0.16 (interior regions) and 0.19 (coastal regions).

Figure 2.3 reports RDI_{30}^i for each station and year within the reference period. It is observed that a negative trend is shown at almost all of the stations. Considering that this index is correlated to the natural recharge of subsurface water bodies, it is relevant to analyze the impact of variability of climate quantities on it across the Region.

As a first step, we consider P_j, T_{m_j}, and ΔT_j as lognormal random variables for each station k. In order to reduce the random dimension
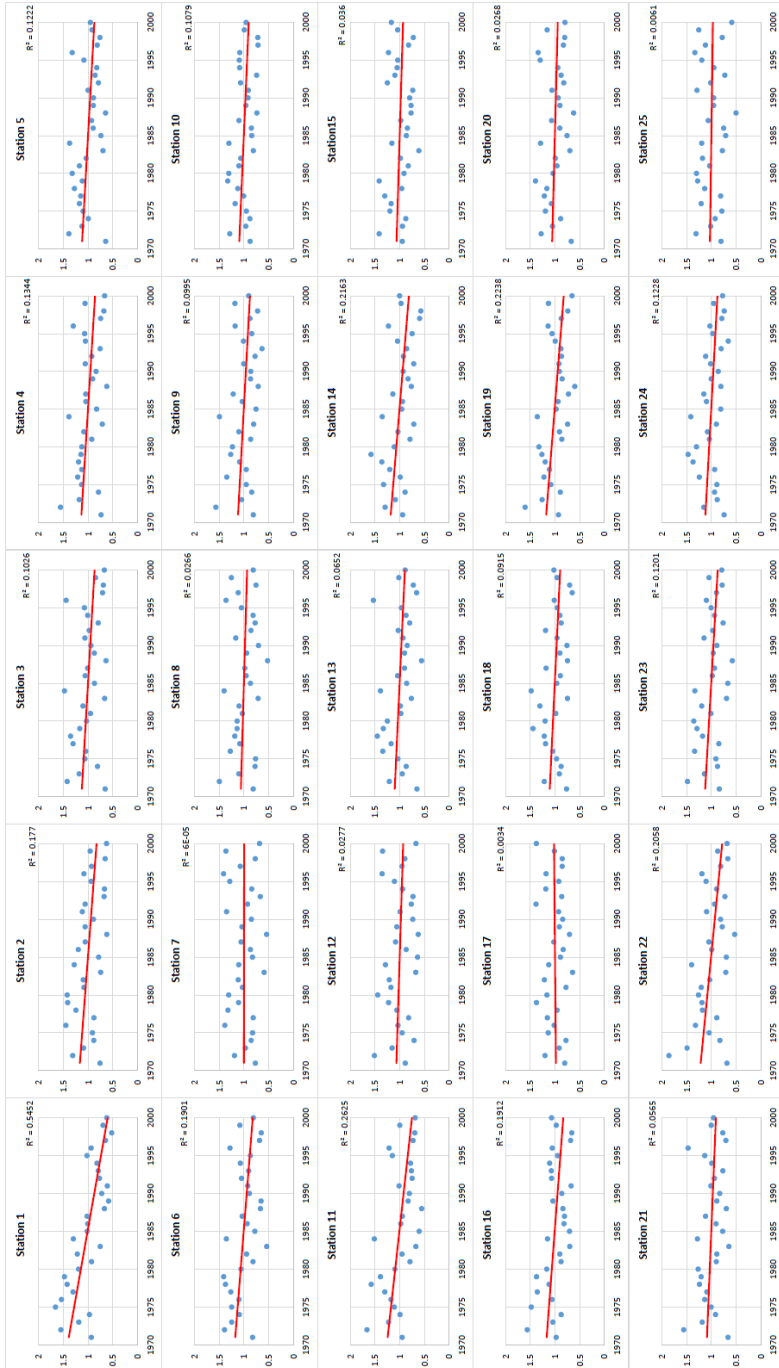
Figure 2.3: Trend of RDI_{30}^i values at each station in the reference period 1971-2000.

of the problem, we apply Monte Carlo simulations (MCs) to propagate uncertainty towards 6 new random variables. In particular, for each station, we derive cumulative precipitations in winter, $P_w = P_{12} + P_1 + P_2$, spring, $P_{sp} = P_3 + P_4 + P_5$, summer, $P_s = P_6 + P_7 + P_8$, and autumn, $P_a = P_9 + P_{10} + P_{11}$, and cumulative evapotranspiration in spring-summer, $PET_{sp,s}$, and autumn-winter, $PET_{a,w}$. As revealed by MCs, these variables are lognormally distributed too, and their moments are collected in Table 2.4.

Table 2.4: Moments of the selected lognormal random variables, estimated at each station for the period $1971 - 2000$.

| k	$\overline{P}_w$	σP_w	$\overline{P}_{sp}$	σP_{sp}	$\overline{P}_s$	σP_s	$\overline{P}_a$	σP_a	$\overline{PET}_{sp,s}$	$\sigma PET_{sp,s}$	$\overline{PET}_{a,w}$	$\sigma PET_{a,w}$
1	5.80	2.71	6.13	2.28	6.16	2.68	8.79	3.51	22.75	1.49	7.04	0.66
2	7.81	2.79	8.35	2.76	6.67	2.53	10.87	4.08	20.68	0.86	7.45	0.41
3	4.37	1.95	5.48	1.71	4.76	1.93	6.29	2.53	22.00	0.63	6.85	0.35
4	5.00	2.15	6.19	1.85	5.07	2.20	7.69	3.14	24.32	0.64	7.82	0.35
5	3.66	1.65	4.98	1.77	5.41	2.05	6.32	2.61	23.03	0.62	7.68	0.33
6	5.43	2.39	6.60	2.25	5.84	2.71	8.75	3.27	24.29	0.64	7.41	0.33
7	4.87	1.95	5.40	2.03	5.25	2.56	7.73	3.00	20.99	0.62	7.16	0.32
8	5.02	2.05	5.69	1.99	5.82	2.40	8.23	3.36	22.38	0.61	7.34	0.31
9	7.02	2.54	8.07	2.24	6.51	2.82	10.59	3.91	19.77	0.77	6.59	0.33
10	12.51	4.52	11.31	3.40	7.55	2.45	15.90	6.20	20.89	0.63	7.26	0.34
11	4.33	1.83	4.70	1.62	5.20	2.38	6.59	3.02	21.64	0.84	7.51	0.39
12	4.42	1.87	5.07	1.87	5.02	2.21	7.30	3.40	23.06	0.70	7.74	0.35
13	4.19	1.79	5.28	1.83	5.25	2.00	6.24	2.48	23.71	0.61	7.41	0.36
14	6.33	2.91	8.24	3.06	6.76	3.00	10.55	4.21	20.71	0.78	6.68	0.36
15	10.88	4.31	11.72	3.97	8.96	3.19	17.88	7.50	16.60	0.54	5.74	0.28
16	6.55	2.76	7.34	2.58	6.20	2.30	10.34	4.29	21.77	0.60	7.18	0.35
17	15.41	5.97	14.13	4.45	9.12	3.14	21.10	9.39	18.18	0.59	5.98	0.32
18	15.63	5.93	14.41	4.70	8.82	3.32	19.43	7.73	16.05	0.60	5.62	0.31
19	5.69	2.07	7.75	2.49	6.99	2.86	9.11	3.46	21.02	0.81	7.47	0.41
20	4.02	1.76	4.77	1.67	5.49	2.52	6.22	2.53	22.81	0.60	7.57	0.33
21	4.16	1.81	5.22	1.61	4.93	1.76	6.34	2.55	24.97	0.70	7.97	0.39
22	5.25	2.15	6.33	2.12	5.60	2.38	8.63	3.77	23.70	0.61	7.78	0.33
23	7.02	2.62	7.84	2.49	5.73	2.29	10.16	3.69	21.79	0.60	7.49	0.32
24	15.34	5.11	14.14	4.20	8.52	2.78	17.63	6.20	13.99	0.56	5.01	0.29
25	4.91	1.98	5.09	1.92	5.53	2.34	8.22	3.51	22.67	0.64	7.91	0.32
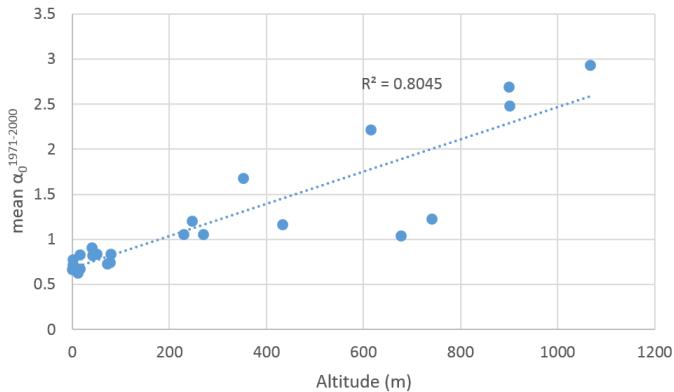
Figure 2.4: Values of $\overline{\alpha}_0^{1971-2000}$ against altitude of each station.

We then consider

$$\alpha_0^{1971-2000} = \frac{P_w + P_{sp} + P_s + P_a}{PET_{sp,s} + PET_{a,w}}, \qquad (2.16)$$

where P_w, P_{sp}, P_s, P_a, $PET_{sp,s}$ and $PET_{a,w}$ are the random variables determined above. We apply PCE to approximate (2.16) in the random parameter space and we compute the distribution-based metric proposed by Borgonovo (Borgonovo, 2007) following the approach presented in Section 2.5.2.

Table 2.5 collects mean and standard deviation associated with (2.16) and the δ index for each uncertain parameter at each station.

We first observe a positive correlation between the altitude of the stations and $\overline{\alpha}_0^{1971-2000}$ as depicted in Figure 2.4.

Figure 2.5 shows $\overline{\alpha}_0^{1971-2000}$ against the Borgonovo δ index associated with the selected uncertain parameters. It is possible to observe that it is detected a positive correlation between $\overline{\alpha}_0^{1971-2000}$ and both

Table 2.5: Mean and standard deviation associated with $\alpha_0^{1971-2000}$ and δ index for each uncertain parameter.

k	$\overline{\alpha}_0^{1971-2000}$	$\sigma_{\alpha_0^{1971-2000}}$	δ_{P_w}	$\delta_{P_{sp}}$	δ_{P_s}	δ_{P_a}	$\delta_{PET_{sp,s}}$	$\delta_{PET_{a,w}}$
1	0.905	0.195	0.144	0.120	0.142	0.208	0.065	0.033
2	1.199	0.223	0.140	0.138	0.121	0.232	0.047	0.026
3	0.725	0.143	0.150	0.135	0.151	0.216	0.032	0.021
4	0.746	0.149	0.140	0.120	0.143	0.236	0.031	0.022
5	0.664	0.134	0.120	0.134	0.160	0.223	0.031	0.022
6	0.840	0.169	0.136	0.129	0.157	0.213	0.031	0.022
7	0.826	0.172	0.122	0.129	0.166	0.218	0.032	0.023
8	0.834	0.169	0.124	0.121	0.150	0.242	0.031	0.022
9	1.222	0.226	0.133	0.116	0.146	0.237	0.045	0.025
10	1.680	0.312	0.171	0.120	0.081	0.266	0.035	0.024
11	0.715	0.157	0.122	0.108	0.167	0.235	0.038	0.021
12	0.709	0.157	0.119	0.120	0.146	0.256	0.034	0.023
13	0.674	0.132	0.134	0.140	0.155	0.208	0.031	0.024
14	1.165	0.245	0.131	0.144	0.136	0.220	0.039	0.024
15	2.215	0.451	0.135	0.124	0.094	0.290	0.036	0.022
16	1.052	0.213	0.141	0.131	0.115	0.255	0.034	0.024
17	2.475	0.514	0.160	0.112	0.075	0.297	0.034	0.022
18	2.692	0.527	0.171	0.131	0.086	0.247	0.041	0.026
19	1.038	0.196	0.116	0.143	0.166	0.220	0.043	0.026
20	0.675	0.142	0.126	0.121	0.197	0.202	0.029	0.020
21	0.627	0.120	0.143	0.126	0.140	0.227	0.033	0.020
22	0.820	0.171	0.125	0.125	0.140	0.260	0.028	0.019
23	1.051	0.194	0.146	0.139	0.122	0.233	0.032	0.022
24	2.931	0.507	0.177	0.139	0.086	0.233	0.048	0.027
25	0.777	0.165	0.123	0.117	0.147	0.258	0.030	0.021

δ_{P_w} and δ_{P_a}, while a negative correlation is shown with δ_{P_s}. A weak correlation is detected with the δ index of the other three parameters.

In general, P_a is the most influence parameter, while $PET_{sp,s}$ and $PET_{a,w}$ have a negligible impact on the pdf of $\alpha_0^{1971-2000}$.

Finally, Figure 2.6 shows a comparison between the Sobol index and the δ index for each selected parameter. A very high correlation is shown, as expected, due to the simplicity of the model used for this example which reduces to 2.16. This further confirms that a distribution-based approach for GSA is more general and provides information tending to that provided by a variance-based approach, depending on the complexity of the relationship between inputs and output.
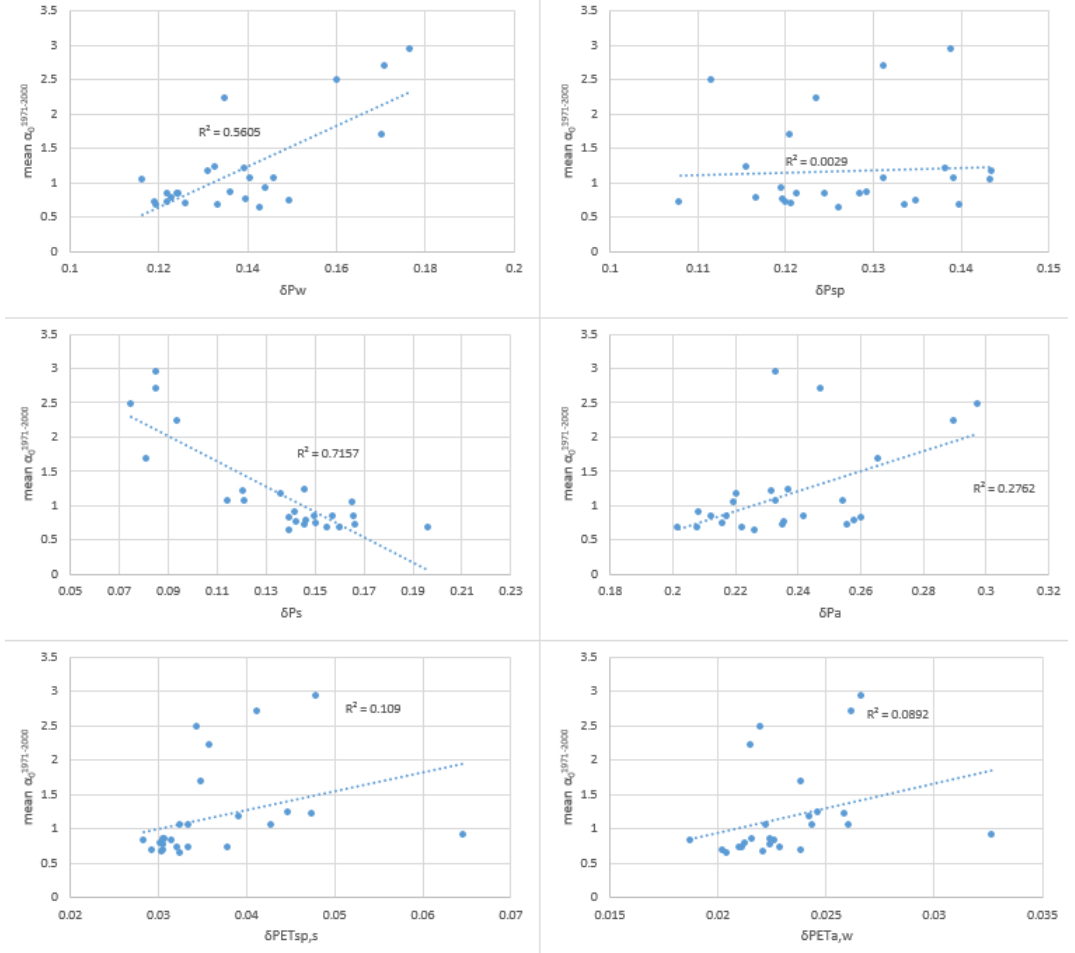
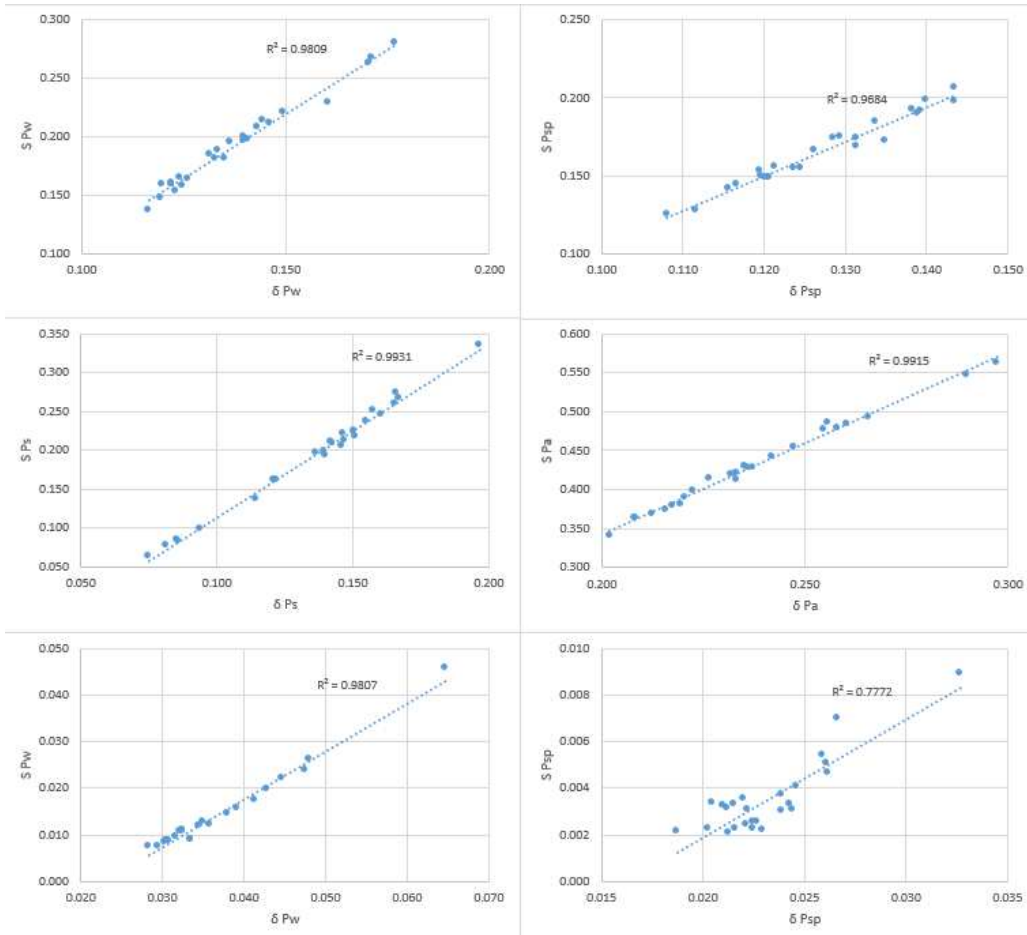Figure 2.5: Values of $\overline{\alpha}_0^{1971-2000}$ against δ indices.

Figure 2.6: Values of Sobol indices against δ indices.

2.6   Research outline

Based on the concepts presented in this Chapter, an integrated framework for PRA applied to the assessment of groundwater vulnerability can be build as described above. In order to explore some of the main factors (or events) that may determine the "failure" (as for an FTA scheme (Figure2.7)) of a given groundwater system (e.g. the predicted groundwater status is not good at the end of a specific time horizon), the following applications are presented in the next chapters:

  i Chapter 3 includes the analysis of local-scale processes dealing with accidental groundwater contamination under hydrological uncertainty.

  ii Chapter 4 is devoted to a river-basin scale analysis of groundwater status and employs these concepts to build a set of climate change scenarios selected on the basis of PCE theory in order to capture the probabilistic region associated with the highest probability of occurance in the random parameter space.

As such, Chapters 3-4 can be seen as a part of a more complex picture to assess the risk associated with the status of a given groundwater body (i.e. possible events within on FTA scheme).
Chapter 5 employs variance-based GSA with the different purpose of exploring an innovative technique for soil moisture measure, while reducing predictive uncertainty.
In the end, Chapter 6 presents a suite of analytical models aimed at describing gravity currents in porous media.
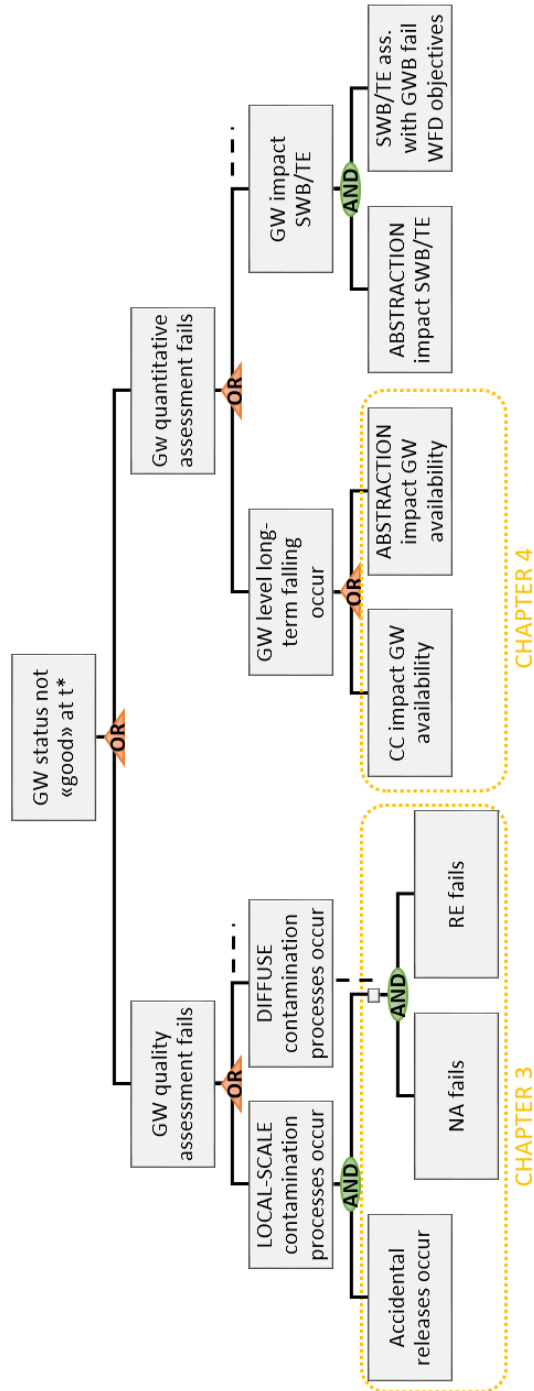
Figure 2.7: Fault Tree Analysis scheme.

Chapter 3

Estimation of environment risk posed by local scale LNAPL contamination processes

Sommario

In questo capitolo si vuole esaminare il caso di un processo di contaminazione locale del sottosuolo, a seguito di un rilascio accidentale di una sostanza chimica. In particolare, si analizzano i processi imputabili a oil spill da condotte onshore. Sebbene le basse frequenze incidentali confermino che il trasporto in condotta rappresenta la modalità di movimentazione via terra più sicura per fluidi chimici, bisogna tuttavia tener presente che i quantitativi di sostanze che possono essere rilasciati da questi impianti sono ingenti, e che il rischio ambientale che ne consegue è potenzialmente elevato.

Lo studio presentato in questo capitolo ha prodotto la pubblicazio-
ne: **"Impact of Hydrogeological Uncertainty on Estimation of
Environmental Risks Posed by Hydrocarbon Transportation
Networks", Water Resources Research, 53(11): 8686-8697
(V. Ciriello, I. Lauriola, S. Bonvicini, V. Cozzani, V. Di Fe-
derico, e Daniel M. Tartakovsky, 2017)**. Tale studio fornisce
una metodologia completa per la valutazione del rischio ambientale a
scala locale, tenendo conto dell'incertezza dei parametri idrogeologici
che regolano la migrazione dei liquidi di fase non acquosi (NAPL) nel
sottosuolo. Nello specifico, si è scelto di adottare un approccio sto-
castico per il campionamento dello spazio parametrico, e di tecniche
quali (i) l'analisi di Sensitività Globale (GSA) e (ii) la metamodella-
zione in Espansione in Chaos Polinomiale (PCE) (v. Capitolo 2). La
prima tecnica è servita per l'identificazione dei parametri più rilevanti
e la riduzione dello spazio parametrico; la seconda ha consentito di
diminuire il costo computazionale della stima dell'estensione spazio-
temporale della contaminazione nel sottosuolo. Fine ultimo dell'analisi
è stato fornire descrittori sintetici per la valutazione del rischio am-
bientale in termini di volumi probabilistici di suolo e acque sotterranee
coinvolti nella contaminazione. L'approccio proposto è generalizzabi-
le e, opportunamente integrato, può essere inserito all'interno di una
PRA (e.g. FTA) a scala di bacino, per valutare l'incidenza di con-
taminazioni accidentali sul rischio associato allo stato qualitativo del
corpo idrico sotterraneo, entro un orizzonte temporale di interesse.

3.1 Introduction

Accidental releases of non-aqueous-phase liquids (NAPLs) into the environment pose significant risks of subsurface contamination, affecting human health, ecosystems and water quality. Onshore pipelines provide the safest way to transport hydrocarbons and other NAPLs over long distances. Yet, even though accidental spills from such pipelines are relatively rare (e.g., OECD, 1997), they might have severe environmental consequences due to large quantities of NAPL released. While risk of human exposure to such contamination is routinely assessed in the context of quantitative risk analysis (QRA) (e.g., CCPS, 1995; TNO, 1999), identification and computation of proper metrics or indices for environmental risk proved to be more elusive. For example, the environmental damage index (Bonvicini et al., 2015) is formulated in terms of the expected overall cost of remediation, $\mathcal{C}_{\text{rem}}$, as

$$\mathcal{C}_{\text{rem}} \equiv \mathcal{C}_{\text{dis}} + \mathcal{C}_{\text{cle}} + \mathcal{C}_{\text{gwt}} = V_{\text{dis}}\hat{\mathcal{C}}_{\text{dis}} + V_{\text{cle}}\hat{\mathcal{C}}_{\text{cle}} + V_{\text{gwt}}\hat{\mathcal{C}}_{\text{gwt}}, \qquad (3.1)$$

where $\mathcal{C}_{\text{dis}}$, $\mathcal{C}_{\text{cle}}$ and $\mathcal{C}_{\text{gwt}}$ are the costs associated with soil disposal, soil clean-up and groundwater treatment, respectively. Each of these costs is computed as the product of an average contaminated volume, V_i, and the unitary cost of the corresponding remediation action, $\hat{\mathcal{C}}_i$, where $i =$ dis, cle and gwt. The volumes V_i are averaged over a number of spill events, differentiated with respect to a cause of the release and the safety barriers present on site. Hence, for a given segment of a pipeline and N spills, the affected volume is estimated by

$$V_i = \sum_{k=1}^{N} p_k \hat{V}_{i,k}, \qquad i = \text{dis, cle and gwt}, \qquad (3.2)$$

where p_k is the probability of occurrence of the kth spill event and $V_{i,k}$ is the unsaturated/saturated volume of soil affected by that contamination event.

Estimation of the contaminated volumes $\hat{V}_{i,k}$ requires computationally intensive numerical solutions of multiphase flow equations, which are parameterized with soil hydraulic and transport parameters. Since the latter are always uncertain, the resulting estimates of $\hat{V}_{i,k}$ are uncertain as well. This uncertainty might significantly, and often unexpectedly, affect estimates of the remediation cost in (3.1), yet its impact remains largely unexplored in risk assessment analyses (Tartakovsky, 2007; Tartakovsky, 2013).

3.2 Mathematical Models of Subsurface Contamination

3.2.1 General Formulation

NAPL Migration in the Vadose Zone. Three distinct phases, water, air and NAPL, are present in the vadose zone; their respective saturations at any "point" (a representative elementary volume) $\mathbf{x}$ and time t are denoted by $S_w(\mathbf{x}, t)$, $S_a(\mathbf{x}, t)$ and $S_N(\mathbf{x}, t)$ such that $S_w + S_a + S_N = 1$. At the continuum scale, $\mathbf{q}_i(\mathbf{x}, t)$, flow velocity of the ith phase ($i = $ a, w, N), is related to $\psi_i(\mathbf{x}, t)$, pressure head in the ith phase, by the generalized Darcy law,

$$\mathbf{q}_i = -K_{s,i} K_{r,i}(S_i) \nabla(\psi_i + x_3), \quad i = \text{a, w, N,} \tag{3.3}$$

where $K_{s,i}(\mathbf{x})$ and $K_{r,i}(\mathbf{x}, S_i)$ are the saturated and relative hydraulic conductivity respectively, with the explicit dependence on $\mathbf{x} = (x_1, x_2, x_3)^\top$ accounting for soil heterogeneity (spatial variability); and x_3 is the vertical coordinate positive upward. Multiphase flow equations are derived by combining these relations with mass conservation,

$$\phi \frac{\partial \rho_i S_i}{\partial t} = -\nabla \cdot (\rho_i \mathbf{q}_i) + f_i, \quad i = \text{a, w, N}, \tag{3.4}$$

where $\phi(\mathbf{x})$ is the soil porosity, ρ_i is the density of the ith phase, and f_i is a generic source term (mass per unit volume). The multiphase flow equations are closed by specifying constitutive laws $\psi_i = \psi_i(S_i)$ and $K_{r,i} = K_{r,i}(S_i)$. The van Genuchten's model provides one example of such laws,

$$\Theta_w = \left[1 + (\alpha \psi_w)^{1/(1-m)}\right]^{-m}, \quad \Theta_w \equiv \frac{S_w - S_{w,\text{ res}}}{S_{w,\text{ sat}} - S_{w,\text{ res}}}, \tag{3.5a}$$

$$K_{r,w} = \sqrt{\Theta_w} \left[1 - (1 - \Theta_w^{1/m})^m\right]^2, \tag{3.5b}$$

where the soil parameter α, the exponents m and the saturated ($S_{w,\text{ sat}}$) and residual ($S_{w,\text{ res}}$) water saturations are fitting parameters. Similar constitutive laws are used for the NAPL phase.

Once (3.3)–(3.5) are solved subject to appropriate initial and boundary conditions, the volume of the soil contaminated with NAPL is computed as $V_N(t) = \{\mathbf{x} : S_N(\mathbf{x}, t) \geq S_N^\star\}$ where $S_N^\star$ is the maximum allowable NAPL saturation.

Solute Migration below Water Table Dissolved component migrates in groundwater following an advection-dispersion-reaction equa-

tion,

$$\frac{\partial c}{\partial t} = \nabla \cdot (\mathbf{D}\nabla c) - \nabla \cdot (\mathbf{v}c) + R(c), \tag{3.6}$$

where $c(\mathbf{x}, t)$ is the solute concentration, $\mathbf{v}(\mathbf{x}, t)$ is the macroscopic flow velocity of groundwater flow, $\mathbf{D}(\mathbf{x}, |\mathbf{v}|)$ is the dispersion coefficient tensor, and $R(c; \kappa)$ is the reaction term parametrized with a reaction rate constant $\kappa(\mathbf{x})$. The longitudinal, D_l, and transverse, D_t, components of the dispersion coefficient $\mathbf{D}$ characterize the spread of the contaminant plume in the directions collinear and perpendicular to the velocity vector $\mathbf{v}$, respectively. For example, if the groundwater flow direction is aligned with the x_1 coordinate, then it is common to define these components as $D_l \equiv D_{11} = D_m + \lambda_l |\mathbf{v}|$ and $D_t \equiv D_{22} = D_{33} = D_m + \lambda_t |\mathbf{v}|$, where D_m is the coefficient of molecular diffusion of the solute in the soil, and $\alpha_l(\mathbf{x})$ and $\alpha_t(\mathbf{x})$ are the longitudinal and transverse dispersivities (typically, these fitting parameters satisfy the condition $\alpha_t \ll \alpha_l$). Once (3.6) is solved subject to appropriate initial and boundary conditions, the volume of the aquifer contaminated with the dissolved contaminant is computed as $V_{gw}(t) = \{\mathbf{x} : c(\mathbf{x}, t) \geq c_N^\star\}$ where $c_N^\star$ is the maximum allowable contaminant concentration. In the deterministic setting, i.e., when all the relevant soil properties and forcings are assumed to be known with certainty, (3.3)–(3.6) are often used to predict subsurface fate and transport of NAPLs e.g., McLaren et al., 2012, and the references therein.

3.2.2 Physics-Based Model

The Hydrocarbon Soil Screening Model (HSSM) (Weaver et al., 1994; Charbeneau, Weaver, and Lien, 1995) is used as physics-based reduced-complexity model of LNAPL migration in the subsurface. Developed by the US EPA, this code is widely used to model LNAPL contamination of soils and groundwater (e.g., Charbeneau and Weaver, 1992; Yoon et al., 2009). The code comprises three modules working in series: (i) one-dimensional vertical multiphase transport in the vadose zone (from the near surface to the capillary fringe); (ii) one-dimensional radial horizontal spreading of the contaminant lens through the capillary fringe; and (iii) two-dimensional, vertically averaged, transport of the dissolved component in the aquifer. Basic assumptions of the code consist in considering the liquid phases to be incompressible and the porous medium as homogeneous and non-deformable. Jang et al., 2013, among others, provide a detailed comparison of the predictions obtained with HSSM and the full model (3.3)–(3.6).

The first module (named KOPT for Kinematic Oil Pollutant Transport) simulates the flow of the LNAPL and the transport of its key chemical constituent through the vadose zone. Soil is characterized by a uniform water content since water saturation is computed from the average annual recharge rate. This assumption allows neglecting the continuity equation for water. The generalized method of characteristics is applied to solve a set of approximated hyperbolic governing equations obtained by neglecting the capillary pressure gradient. As a consequence, gravity acts as the only driving force and the leading edge of the LNAPL is represented as a sharp front. Lateral spreading

due to capillary forces is not addressed.

The second module (named OILENS) simulates a radial spreading of the hydrocarbon on the water table. The unsteady motion is represented as a sequence of steady states based on the assumptions of incompressible flow and vertical equilibrium for the fluids at any location. A simplified description of the LNAPL lens (e.g., a semi-analytical solution of Sudicky et al., 2013) is then provided, together with the mass flux towards the aquifer against time. This is used as a boundary condition for the third module (named TGSPLUM) representing the migration of the dissolved component in the aquifer based on a Gaussian-source plume model. Advection-dispersion processes are assumed to govern transport in two dimensions. Effect of dilution produced by natural recharge is modeled as a decay term. Furthermore, steady state is considered and velocity is assumed to be uniform in the flow direction.

These approximations simplify the computation of the contaminated volumes $V_N(t)$ and $V_{gw}(t)$. The assumption of one-dimensional (vertical) flow in the vadose zone implies that, for a given (and possibly uncertain) surface spill of area A_{spill}, the former is given by $V_N(t) = A_{spill} z_N(t)$, where $z_N(t)$ is the depth of soil within which the NAPL saturation is $S \geq S_N^\star$. The assumption of two-dimensional (horizontal) transport below the water table leads to $V_{gw}(t) \approx \Delta_z A_{gw}(t)$, where Δz is the unit thickness used in the TGSPLUM module and $A_{gw}(t)$ is the aquifer's area within which the concentration $c(\mathbf{x}, t) \geq c_N^\star$.

Selection of an "optimal" model depends on the complex interplay between quantities of interest and availability of (never sufficient) site-specific data and computational resources; a complex model with a

large number of uncertain parameters might yield less accurate predictions than its reduced-complexity counterpart that allows for exhaustive exploration of the parameter space (Sinsbeck and Tartakovsky, 2015). The latter study demonstrates that the HSSM model, which can be sampled extensively due to low computational cost of individual deterministic solves, is likely to outperform the full model (3.3)–(3.6), whose high computational cost typically makes it possible to compute no more than 10s realizations (Maji and Sudicky, 2008; McLaren et al., 2012), when it comes to computing cumulative distribution functions of the quantities of interest.

3.2.3 Model Parametrization

Virtually every parameter in (3.3)–(3.6) and, hence, in our physics-based model (HSSM) is space- and scale-dependent, reflecting the multiscale heterogeneity of subsurface environments. While some of these parameters, e.g., the fitting parameters in the constitutive relations (3.5), are often determined at the laboratory scale from a few soil samples, others, e.g., the dispersivities in (3.6), are inferred at the field scale by calibrating the model's predictions to an observed spatial extent of the plume. Given this disparity of scales and the ubiquitous scarcity of data, the standard practice is to assign a statistical model (a probability density function or PDF) to such parameters and to compute its statistical parameters (e.g., mean and variance) from measurements.

Statistical properties the key parameters affecting contaminant transports in the vadose and saturated zones are presented in Table 3.1. Rather than treating these parameters as random fields, a

Table 3.1: Statistical distributions (PDFs) and properties (mean, $\langle \cdot \rangle$, and standard deviation, σ) of the uncertain model parameters in Eqs. (3.3)–(3.6). All but the last two parameters depend on soil texture and are separated into three classes representing distinct soil types: sand, sandy loam, and loam. The data are from Carsel and Parrish, 1988.

Parameter	PDF	Sand	Sandy loam	Loam
α (1/m)	Lognormal	$\langle \alpha \rangle = 14.5$	$\langle \alpha \rangle = 7.5$	$\langle \alpha \rangle = 3.6$
		$\sigma_\alpha = 2.9$	$\sigma_\alpha = 3.7$	$\sigma_\alpha = 2.1$
$n = (1-m)^{-1}$	Lognormal	$\langle n \rangle = 2.68$	$\langle n \rangle = 1.89$	$\langle n \rangle = 1.56$
		$\sigma_n = 0.29$	$\sigma_n = 0.17$	$\sigma_n = 0.11$
K_s (m/d)	Lognormal	$\langle K_s \rangle = 7.1$	$\langle K_s \rangle = 1.1$	$\langle K_s \rangle = 0.25$
		$\sigma_{K_s} = 3.7$	$\sigma_{K_s} = 1.4$	$\sigma_{K_s} = 0.44$
ϕ	Normal	$\langle \phi \rangle = 0.43$	$\langle \phi \rangle = 0.41$	$\langle \phi \rangle = 0.43$
		$\sigma_\phi = 0.06$	$\sigma_\phi = 0.09$	$\sigma_\phi = 0.10$
J	Normal	$\langle J \rangle = 0.001,$	$\sigma_J = 0.0003$	
α_1 (m)	Lognormal	$\langle \alpha_1 \rangle = 10.0,$	$\sigma_{\alpha_1} = 3.0$	

zonation approach is adopted which uses soil types to subdivide a subsurface environment into regions whose properties are modeled as random variables. Such a conceptualization is often used in practice, where one has to contend with data scarcity or, in the absence of data, rely on regional soil maps. To be specific, in the simulations reported below it is assumed that the soil consists of a single uniform stratum of either sand or sandy-loam or loam, and assign to each the means and standard deviations identified by Carsel and Parrish, 1988. (A layered soil structure can be readily accommodated as well by adopting the random domain decomposition (Winter and Tartakovsky, 2000; Lin, Tartakovsky, and Tartakovsky, 2010).) The regional groundwater head gradient J is assigned a normal distribution with a range of variation consistent with typical values in the application area. Finally,

the longitudinal dispersivity α_l is assumed to follow a lognormal distribution with a mean and standard deviation selected on the basis of an estimation of the characteristic domain length; the transverse dispersivity is set to $\alpha_t = 0.1\alpha_l$.

There is an ongoing debate about whether the soil properties reported in Table 3.1 are mutually correlated (see Tartakovsky, Neuman, and Lu, 1999; Tartakovsky, Guadagnini, and Riva, 2003; Carsel and Parrish, 1988, and the references therein). An often used argument for their independence is that the saturated hydraulic conductivity K_s is controlled by macro-voids, while the reciprocal of the capillary length α depends on the entire continuum of pore size (see Tartakovsky, Neuman, and Lu, 1999, and the references therein). Adopting these hypotheses, and given the weak correlation exhibited by the parameters (and their logarithms) in the most of the tests analyzed, all the uncertain parameters in Table 3.1 are assumed to be mutually independent.

Since the focus is on the effects of uncertain hydrogeological parameters on risk-based assessment of subsurface contamination, the hydrocarbon properties are assumed to be known with certainty, i.e., are treated as deterministic quantities. However, the probabilistic framework introduced in Section 3.3 can also account for uncertainty in the latter parameters, as well as for the probability of pipeline rupture.

3.3   Probabilistic Framework

3.3.1   Random Parameter Space

Table 3.1 shows the six-dimensional parameter space in terms of $M = 6$ *standard Gaussian* variables, $\mathbf{P} = \{P_1, \ldots, P_6\}$, such that

$$P_1 = \frac{\ln \alpha - \langle \ln \alpha \rangle}{\sigma_{\ln \alpha}}, \quad P_2 = \frac{\ln n - \langle \ln n \rangle}{\sigma_{\ln n}}, \quad P_3 = \frac{\ln K_{\mathrm{s}} - \langle \ln K_{\mathrm{s}} \rangle}{\sigma_{\ln K_{\mathrm{s}}}},$$

$$\text{(3.7a)}$$

$$P_4 = \frac{\phi - \langle \phi \rangle}{\sigma_\phi}, \quad P_5 = \frac{J - \langle J \rangle}{\sigma_J}, \quad P_6 = \frac{\ln \alpha_{\mathrm{l}} - \langle \ln \alpha_{\mathrm{l}} \rangle}{\sigma_{\ln \alpha_{\mathrm{l}}}}. \quad \text{(3.7b)}$$

The statistics of $\ln \alpha$ (or other logarithms) are related to that of α (or other log-normally distributed variables in Table 3.1) by $\ln \langle \alpha \rangle = \langle \ln \alpha \rangle + \sigma_{\ln \alpha}/2$ and $\sigma_\alpha^2/\langle \alpha \rangle^2 = \exp(\sigma_{\ln \alpha}^2) - 1$.

Solving for any quantity of interest (QoI) Q is equivalent to identifying the functional relation $Q(\mathbf{x}, t; \mathbf{P})$. A truncated polynomial chaos expansions (PCE) (Wiener, 1938) approximates the QoI $Q(\mathbf{x}, t; \mathbf{P})$ as shown in Section 2.4.1, where $\Psi_j(\mathbf{P})$ denotes, in this case, multivariate Hermite polynomials. The SC method (Webster, Tatang, and McRae, 1996) is used to compute the deterministic expansion coefficients (e.g., Ciriello et al., 2013c).

While the SC might underperform Monte Carlo when the hydraulic properties are spatially varying random functions with relatively short correlation lengths and/or relatively high variances (Barajas-Solano and Tartakovsky, 2016), it is well suited for the low dimensional probability spaces, such as $M = 6$ considered in the present study (e.g., (Ciriello et al., 2013b), (Ciriello et al., 2015), and references therein).

Two quantities of interest (QoIs) are dealt with, $V_{\mathrm{vz}}^{\star} = V_{\mathrm{vz}}(t^{\star})$ and $V_{\mathrm{gw}}^{\star} = V_{\mathrm{gw}}(t^{\star})$, where $V_{\mathrm{vz}}^{\star}$ and $V_{\mathrm{gw}}^{\star}$ are the subsurface volumes defined in Section 3.2.1, and $t^{\star}$ is the number of days from the contaminant release required to detect the occurrence of contamination. Second-degree polynomial representations of these QoIs, with $p = 2$, have the form

$$V_{\mathrm{vz}}^{\star} = \sum_{i=1}^{M-2} a_i P_i + \sum_{i=1}^{M-2} a_{ii}(P_i^2 - 1) + \sum_{i=1}^{M-2}\sum_{k>i}^{M-2} a_{ik}P_i P_k, \qquad (3.8)$$

and

$$V_{\mathrm{gw}}^{\star} = \sum_{i=1}^{M} b_i P_i + \sum_{i=1}^{M} b_{ii}(P_i^2 - 1) + \sum_{i=1}^{M}\sum_{k>i}^{M} b_{ik}P_i P_k. \qquad (3.9)$$

The coefficients in these polynomials are obtained with the SC. The so-called "surrogate models" (3.8) and (3.9) serve as low-fidelity probabilistic predictors of our QoIs $V_{\mathrm{vz}}^{\star}$ and $V_{\mathrm{gw}}^{\star}$, respectively. If necessary, one can improve the accuracy of these surrogate models by increasing the polynomial order.

3.4   Case Study

Following Bonvicini et al., 2015, a benzene spill from a pipeline, of length 16 km and diameter 6 in and equipped with automatic shut-down valves is considered. A volume of $V_{\mathrm{spill}} = 291.7$ m^3 of benzene is released, forming a circular pool of radius $R_{\mathrm{spill}} = 17.6$ m and height $h_{\mathrm{spill}} = 0.3$ m; the height of the pool is kept constant for one minute and then gradually decreases to zero as the substance infiltrates into

the soil. Benzene is classified as a carcinogenic and mutagenic substance, whose maximum allowable concentration in groundwater is set, e.g., in Italy, to $c_N^\star = 1.0 \ \mu g/l$ (Legislative Directive, 2010).

Two contamination scenarios are analyzed. The first (Section 3.4.1) deals with an aquifer that is sufficiently deep for the benzene plume to remain in the vadose zone during a given timeframe (in the simulations reported below $t^\star = 180$ days is set). The second (Section 3.4.2) represents a shallow aquifer, whose water table is located 5.0 m below the ground surface. In both cases, the aim is to relate, probabilistically, the spatial extent of subsurface contamination to soil types and other parameters whose statistical properties are reported in Table 3.1.

3.4.1   Scenario 1: Deep Water Table

For a given area of surface spill A_{spill}, the physics-based model of Section 3.2.2 determines the volume of contaminated soil after $t^\star = 180$ days in terms of $z_N^\star = z_N(t^\star)$. The latter is described probabilistically in terms of its cumulative distribution function (CDF), $F_{z_N^\star}(\zeta) \equiv \mathbb{P}(z_N^\star \leq \zeta)$, which is constructed with a kernel density estimator (KDE) from the N_{SC} solutions (collocation points), $z_{N,i}^\star$ for $i = 1, \ldots, N_{\mathrm{SC}}$, of the surrogate model (3.8). Specifically, a Gaussian kernel is used with a filter size $h = 0.0255$, so that a KDE of $F_{z_N^\star}(\zeta)$ is given by

$$F_{z_N^\star}(\zeta) \approx \frac{1}{N_{\mathrm{NC}}\sqrt{2\pi h^2}} \sum_{i=1}^{N_{\mathrm{SC}}} \exp\left[-\frac{(\zeta - z_{N,i}^\star)^2}{2h^2} \right]. \qquad (3.10)$$

Figure 3.1 exhibits the resulting CDFs, alongside the corresponding Gaussian CDFs, for the three soil types whose statistical properties are
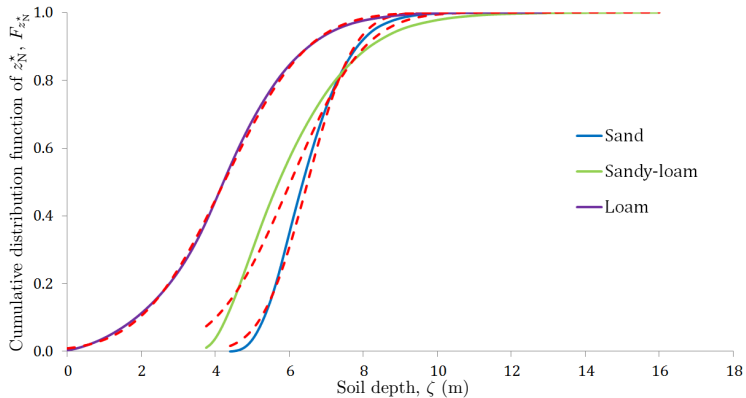
Figure 3.1: Cumulative distribution function, $F_{z_N^\star}(\zeta)$, of the depth of soil contamination after $t^\star = 180$ days from the spill, $z_N^\star$, computed with the surrogate model (3.8) for three soil-texture types. The adjacent dashed lines depict the corresponding Gaussian distribution.

given in Table 3.1. As expected, the average (ensemble mean) depth of contamination increases with the grain size since they correspond to higher values of hydraulic conductivity and, hence, higher rates of NAPL migration. Perhaps less expected, is the concomitant decrease in predictive uncertainty, which is quantified by the standard deviation of $z_N^\star$ (the CDF width). This reflects higher variability of the hydrogeological properties of finer-grained soils (Table 3.1).

Figure 3.1 also reveals that, depending on soil type and composition, the CDF of $z_N^\star$ can significantly deviate from the Gaussian distribution. Consequently, the mean ($\mu_{z_N^\star}$) and standard deviation ($\sigma_{z_N^\star}$) of $z_N^\star$ are insufficient for probabilistic assessment of soil contamination. The latter calls for knowledge of the full CDF or such statistics as the median contamination depth (the depth that occurs with probability

$\mathbb{P} = 0.5$) and the depth predicted with a given degree of certainty (e.g., probability $\mathbb{P} = 0.99$). Such statistics are obtained by inverting the CDFs in Figure 3.1; a few examples are presented in Table 3.2. Conservative estimates ($\mathbb{P} = 0.99$) of soil contamination can be up to an order of magnitude smaller than their average counterparts.

Table 3.2: Statistics of the depth of NAPL contamination, $z_N^\star$, for three soil types: mean $\mu_{z_N^\star}$, median $m_{z_N^\star}$, standard deviation $\sigma_{z_N^\star}$, contamination depth $z_{99\%}^\star$ occurring with $\mathbb{P} = 0.99$, and the probability $\mathbb{P}$ that contamination depth does not exceed 5 m.

Soil type	$\mu_{z_N^\star}$ (m)	$m_{z_N^\star}$ (m)	$\sigma_{z_N^\star}$ (m)	$z_{99\%}^\star$ (m)	$\mathbb{P}(z_N^\star \leq 5 \text{ m})$
sand	6.48	6.33	0.98	4.76	0.04
sandy-loam	6.00	5.68	1.57	3.81	0.30
loam	4.03	4.24	2.10	0.30	0.68

Since predictive uncertainty and, ultimately, quantification of the risk posed by a surface NAPL spill stem from uncertainty in multiple soil properties, the relative impact of these uncertain parameters is important to understand and mitigate by a targeted data collection. Table 3.3 demonstrates the contribution of each uncertain hydraulic parameter, as described by their Sobol' indices, to the overall uncertainty in predictions of the contamination depth $z_N^\star$. The impact of uncertainty in the values of porosity ϕ and saturated hydraulic conductivity K_s is orders of magnitude higher than that of parameters α and n in the van Genuchten constitutive laws (3.5). That is reassuring, since both ϕ and K_s are significantly easier to measure than α and n and consequently their data are more widely available and correlated with soil types. This finding also suggests the possibility

of replacing the uncertain (random) parameters α and n (and, for coarse soils, K_s) with their average values, thus appreciably reducing the random dimension of the problem and, hence, the computational cost. (It is worthwhile emphasizing that the observed relative impact of uncertainty in the various soil properties on the predictive uncertainty is predicated on model selection; replacing the HSSM with the full model (3.3)–(3.6) might lead to different conclusions.)

Table 3.3: Sobol' sensitivity indices $\mathcal{S}_i$ for porosity ($i = \phi$), saturated hydraulic conductivity ($i = K_s$), and parameters α and $n = 1/(1-m)$ in the van Genuchten constitutive laws (3.5). The indices are defined with respect to predictions of the soil contamination depth $z_N^\star$, for three soil types.

Soil type	$\mathcal{S}_\phi$	$\mathcal{S}_{K_s}$	$\mathcal{S}_\alpha$	$\mathcal{S}_n$
Sand	9.67×10^{-1}	2.92×10^{-2}	3.44×10^{-7}	3.63×10^{-3}
Sandy-loam	9.70×10^{-1}	3.14×10^{-2}	1.17×10^{-4}	7.07×10^{-4}
Loam	3.29×10^{-1}	6.64×10^{-1}	1.66×10^{-4}	9.59×10^{-3}

3.4.2 Scenario 2: Shallow Water Table

The case of a shallow phreatic aquifer whose water table is located 5 m below the earth surface is considered. The focus is on subsurface environments composed of either sand or sandy-loam, in which the probability of NAPL reaching the water table is high: $\mathbb{P} \approx 0.96$ or 0.70, respectively (Table 3.2). Figure 3.2 shows CDF of the groundwater area $A_{gw}^\star$, within which the concentration $c(\mathbf{x}, t^\star)$ exceeds $c_N^\star = 1.0\,\mu g/l$ after $t^\star = 180$ days from the spill occurrence. The CDF is constructed

with the KDE analogous to (3.10) from the N_{SC} solutions (collocation points), $A^\star_{gw,i}$ for $i = 1, \ldots, N_{SC}$, of the surrogate model (3.9). As expected, at any probability level, the contaminated area of the sandy aquifer is significantly larger than that of its counterpart comprised of sandy loam (the CDF for the former is to the right of the latter). Uncertainty in predictions of the plume size is appreciably higher in sandy-loam than in sand; this is evidenced by the widths of their corresponding CDFs and their standard deviations ($\sigma_{A^\star_{gw}}$) reported in Table 3.4.
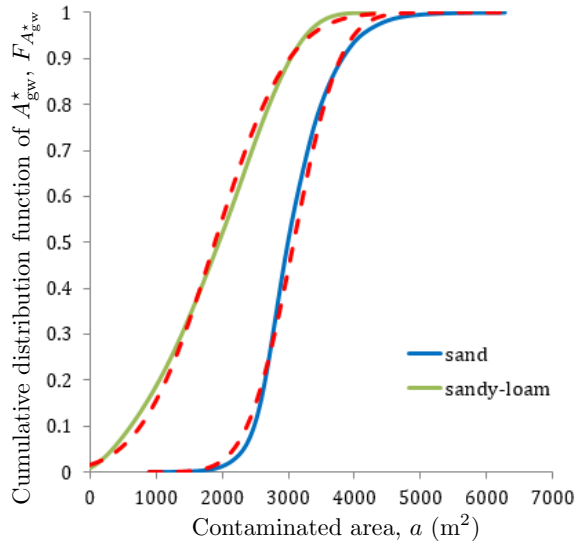

Figure 3.2: Cumulative distribution function, $F_{A^\star_{gw}}(a)$, of the plume size after $t^\star = 180$ days from the spill, $A^\star_{gw}$, computed with the surrogate model (3.9) for two soil-texture types. The adjacent dashed lines depict the corresponding Gaussian distribution.

Figure 3.2 reveals that the CDFs of the plume size are reasonably close to Gaussian CDFs for both sand and sandy-loam. Discrepancy between the computed CDFs and its Gaussian counterparts is illustrated by the difference between the mean ($\mu_{A_{\mathrm{gw}}^\star}$) and median ($m_{A_{\mathrm{gw}}^\star}$) of the plume size (Table 3.4). The two statistics are identical for Gaussian distributions, but differ by 2% and 18% for sand and sandy-loam, respectively.

Table 3.4: Statistics of the plume size in groundwater, $A_{\mathrm{gw}}^\star$, for two soil types: mean $\mu_{A_{\mathrm{gw}}^\star}$, median $m_{A_{\mathrm{gw}}^\star}$, standard deviation $\sigma_{A_{\mathrm{gw}}^\star}$, and plume size $A_{99\%}^\star$ occurring with $\mathbb{P} = 0.99$.

Soil type	$\mu_{A_{\mathrm{gw}}^\star}$ (m^2)	$m_{A_{\mathrm{gw}}^\star}$ (m^2)	$\sigma_{A_{\mathrm{gw}}^\star}$ (m^2)	$A_{99\%}^\star$
sand	3.08×10^3	3.01×10^3	5.47×10^2	1.95×10^3
sandy-loam	1.59×10^3	1.95×10^3	1.24×10^3	1.30×10^1

Similar to the deep water-table case, the Sobol' indices indicate that uncertainty in the values of porosity ϕ and saturated hydraulic conductivity K_{s} dominates the overall predictive uncertainty, with uncertainty in the direction of hydraulic gradient playing an important role in the sandy aquifer (Table 3.5). The latter would play a larger role in the aquifer consisting of sandy-loam if the simulation horizon $t^\star$ were longer because both the NAPL in the vadose zone and its dissolved phase in the aquifer migrate slower in sandy-loam. Second-order effects are detected in case of a sandy soil as follows: $\mathcal{S}_{K_{\mathrm{s}},\alpha_1} = 2.74 \times 10^{-2}$, and $\mathcal{S}_{K_{\mathrm{s}},J} = 4.02 \times 10^{-2}$. Once again, uncertainty in hard-to-measure parameters, such as the parameters in the van Genuchten constitutive laws (α and n), is relatively unimportant, because their Sobol' indices are orders of magnitude smaller than those

of ϕ and K_{s}.

Table 3.5: Sobol' sensitivity indices $\mathcal{S}_i$ for the six uncertain parameters whose statistics are collated in Table 3.1. The indices are defined with respect to predictions of the aquifer contamination area $A_{\mathrm{gw}}^{\star}$, for two soil types.

Soil type	$\mathcal{S}_\phi$	$\mathcal{S}_{K_{\mathrm{s}}}$	$\mathcal{S}_\alpha$	$\mathcal{S}_n$	$\mathcal{S}_{\alpha_1}$	$\mathcal{S}_J$
sand	0.16	0.54	4.58×10^{-4}	8.58×10^{-5}	8.42×10^{-2}	0.12
sandy-loam	0.45	0.52	7.76×10^{-6}	3.05×10^{-5}	1.52×10^{-3}	1.26×10^{-3}

3.4.3   Model verification

The preceding probabilistic analysis of the depth of contaminated soil, $z_{\mathrm{N}}^{\star}$, and area of contaminated aquifer, $A_{\mathrm{gw}}^{\star}$, relies on the surrogate models (3.8) and (3.9), respectively. To ascertain the predictive accuracy of these polynomial representations, 40 realizations of the QoIs are generated ($z_{\mathrm{N},k}^{\star}$ and $A_{\mathrm{gw},k}^{\star}$ with $k = 1, \ldots, 40$ per soil type) by randomly selecting 40 realizations of the parameters in (3.8) and (3.9), $\mathbf{P}_k$ with $k = 1, \ldots, 40$. Each of these parameter sets is then used to compute a solution of the physics-based model (Section 3.2.2) and post-process the results to construct high-fidelity estimates of $z_{\mathrm{N},k}^{\star}$ and $A_{\mathrm{gw},k}^{\star}$. Figure 3.3 provides a comparison of the 40 estimates obtained with these two alternative models for several soil types. A perfect agreement between the two models corresponds to points (realizations) that fall on the 45° (dashed) line; the (solid) regression lines are close to the 45° lines, with the coefficient of determination $R^2 = 0.976$ and 0.980 for the predictions of $z_{\mathrm{N}}^{\star}$ (left) and $A_{\mathrm{gw}}^{\star}$, respectively. This demonstrates the accuracy of the surrogate models for both QoIs.

The accuracy improves as the soil becomes coarser, yielding a virtually perfect agreement with the physics-based models for sand. This is because the variances of the input parameters increase as the grain size decreases (Table 3.1), affecting the accuracy of the PCEs (3.8) and (3.9). The latter can be improved by increasing the polynomial order and, hence, the computational cost of SC. For the purposes of screening analysis and risk assessment, the agreement shown in Figure 3.3 is deemed to be sufficient.

3.4.4 Probabilistic Environmental Risk Indices

The results presented in Sections 3.4.1 and 3.4.2 demonstrate how uncertainty in the soil hydraulic properties propagates through the modeling process, giving rise to uncertainty in predictions of volumes of the contaminated soils and aquifers. Hence, computation of the environmental risk indices (Bonvicini et al., 2015) must account for uncertainty in estimation of the subsurface volumes $V_{i,k}$ in (3.2). For a single surface spill ($k = 1$) with area $A_{\text{spill}} = \pi 17.6^2$ m^2 in scenario 1 (Section 3.4.1), the deep aquifer is unaffected by contamination after $t^\star = 180$ days, and estimates of the volumes of contaminated soil in the vadose zone, $V_{\text{vz}}^\star = A_{\text{spill}} z_{\text{N}}^\star$, are reported in Table 3.6 for probability levels $\mathbb{P} = 0.5$ (a median estimate, $m_{V_{\text{vz}}^\star} \equiv V_{\text{vz},50\%}^\star$) and $\mathbb{P} = 0.99$ (an estimate $V_{\text{vz},99\%}^\star$). Since this scenario deals with a deep aquifer, no contamination of groundwater takes place.

The same NAPL spill in scenario 2 (Section 3.4.2) can contaminate both the vadose zone and shallow aquifer. The probability of occurrence of these two events, $V_{\text{vz}}^\star$ and $V_{\text{gw}}^\star$, is characterized by their joint CFD $F_{V_{\text{vz}}^\star V_{\text{gw}}^\star}(v_1, v_2) \equiv \mathbb{P}(V_{\text{vz}}^\star \leq v_1, V_{\text{gw}}^\star \leq v_2) = 1 - \mathbb{P}(V_{\text{vz}}^\star >$
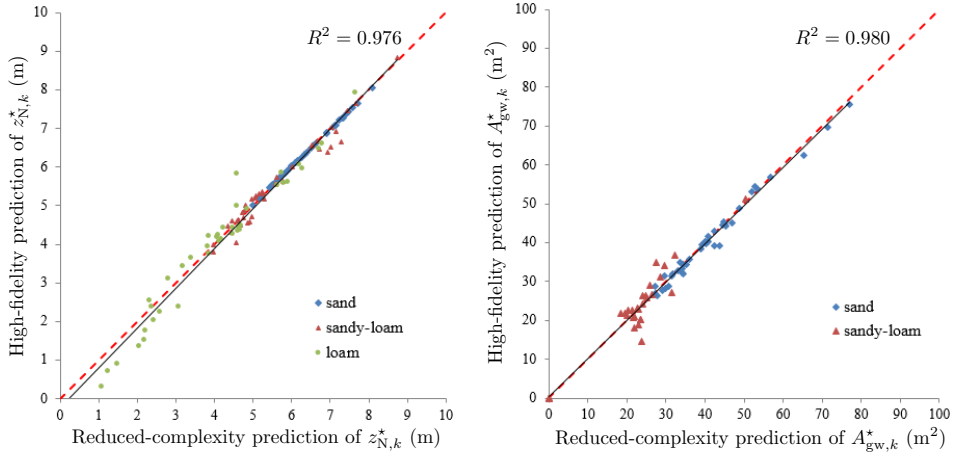
Figure 3.3: Realizations ($k = 1, \ldots, 40$) of the quantities of interest $z^{\star}_{N,k}$ (left) and $A^{\star}_{gw,k}$ (right) computed with the reduced-complexity surrogate model (the horizontal axis) and the physics-based model (the vertical axis), for several soil types. Data falling on the $45°$ (dashed) lines indicate the perfect agreement between the two models. The closeness of these lines to the regression (solid) lines indicates a close agreement between the models, with the coefficient of determination $R^2 = 0.976$ and 0.980 for the predictions of $z^{\star}_N$ (left) and $A^{\star}_{gw}$, respectively.

Table 3.6: Probabilistic estimates, at $\mathbb{P} = 0.5$ and 0.99 probability levels, of the volumes of the vadose zone ($V_{\mathrm{vz}}^{\star}$) and groundwater ($V_{\mathrm{gw}}^{\star}$) contaminated by a surface spill of NAPL after $t^{\star} = 180$ days.

Contaminated volume (m^3)	sand	sandy-loam	loam
Scenario 1: $V_{\mathrm{vz},50\%}^{\star}$	6.16×10^3	5.53×10^3	4.13×10^3
$V_{\mathrm{vz},99\%}^{\star}$	4.63×10^3	3.71×10^3	2.92×10^2
$V_{\mathrm{gw},50\%}^{\star}$	0	0	0
$V_{\mathrm{gw},99\%}^{\star}$	0	0	0
Scenario 2: $V_{\mathrm{vz},50\%}^{\star}$	6.16×10^3	5.53×10^3	4.13×10^3
$V_{\mathrm{vz},99\%}^{\star}$	4.63×10^3	3.71×10^3	2.92×10^2
$V_{\mathrm{gw},50\%}^{\star}$	3.03×10^3	2.50×10^3	$-$
$V_{\mathrm{gw},99\%}^{\star}$	1.94×10^3	1.17×10^2	$-$

$v_1, V_{\mathrm{gw}}^{\star} \leq v_2$). The latter is expressed in terms of conditional probability $\mathbb{P}(V_{\mathrm{vz}}^{\star} > v_1, V_{\mathrm{gw}}^{\star} \leq v_2) = \mathbb{P}(V_{\mathrm{gw}}^{\star} \leq v_2 | V_{\mathrm{vz}}^{\star} > v_1)\mathbb{P}(V_{\mathrm{vz}}^{\star} > v_1)$. Since $V_{\mathrm{vz}}^{\star} = A_{\mathrm{spill}} z_{\mathrm{N}}^{\star}$ and A_{spill} is deterministic, $\mathbb{P}(V_{\mathrm{vz}}^{\star} > v_1) = \mathbb{P}(z_{\mathrm{N}}^{\star} > z)$. For the vadose zone of thickness $z = 5$ m and composed of sand or sandy-loam, $\mathbb{P}(z_{\mathrm{N}}^{\star} > 5 \text{ m}) = 0.96$ or 0.70, respectively (see Table 3.2). Once the NAPL reached the water table, the probability of the groundwater plume having the size smaller than v_1 is given by $\mathbb{P}(V_{\mathrm{gw}}^{\star} \leq v_2 | V_{\mathrm{vz}}^{\star} > v_1)$. Given the modeling assumptions, $\mathbb{P}(V_{\mathrm{gw}}^{\star} \leq v_2 | V_{\mathrm{vz}}^{\star} > v_1) = \mathbb{P}(A_{\mathrm{gw}}^{\star} \leq a | z_{\mathrm{N}}^{\star} > 5 \text{ m})$. The latter is the CDF plotted in Fig. 3.2 and has the statistics presented in Table 3.4. With these preliminaries, $V_{\mathrm{vz},r\%}^{\star} = A_{\mathrm{spill}} z_{\mathrm{N},r\%}^{\star}$ is presented in Table 3.6 for $r = 50$ and 99; and the corresponding values of $V_{\mathrm{gw},r\%}^{\star} = b A_{\mathrm{gw},r\%}^{\star}$ are obtained (for the aquifer of unit thickness, $b = 1.0$ m) by solving for a the equation $\mathbb{P}(A_{\mathrm{gw}}^{\star} \leq a | z_{\mathrm{N}}^{\star} > 5 \text{ m})\mathbb{P}(z_{\mathrm{N}}^{\star} > 5 \text{ m}) = (1 - r)/100$. This is done

numerically by defining $A^\star_{\mathrm{gw},r\%}$ as the abscissa of the graph in Fig. 3.2 at which $F_{A^\star_{\mathrm{gw}}} = (1-r)/[100\mathbb{P}(z^\star_N > 5 \text{ m})]$. The results are presented in Table 3.6.

Finally, three remediation techniques are considered—excavation of the top 1.2 m of soil accompanied by subsequent landfill disposal, soil clean-up by means of vapor extraction, and groundwater clean-up with air sparging—whose unitary costs are $\hat{\mathcal{C}}_{\mathrm{dis}} = 150$ euro/m^3, $\hat{\mathcal{C}}_{\mathrm{cle}} = 100$ euro/m^3 and $\hat{\mathcal{C}}_{\mathrm{gwt}} = 65$ euro/m^3, respectively (Bonvicini et al., 2015). Figure 3.4 depict 50% and 99% probability estimates of the overall costs of subsurface remediation, computed with (3.1) and (3.2). Uncertainty in the hydrogeological parameters strongly affects predictions of the remediation costs even within a single texture class and especially for fine-grained soils.

Figure 3.4: The 50% and 99% probability estimates of the overall costs of subsurface remediation in Scenarios 1 (top) and 2 (bottom).

3.5 Final remarks

The uncertainty affecting predictions of environmental impact due to an accidental oil-spill from an onshore pipeline was quantified in case of three different texture classes: sand, sandy-loam and loam. The environmental impact is defined through the computation of volumes of unsaturated and saturated soil affected by the contamination within a given timeframe. Volumes are computed by means of PCE-based metamodels defined over a selected full model solving multiphase flow problems. It was found that uncertainty in model predictions increases when grain-size decreases. This is mainly due to the variability of key hydrogeological parameters that increases in case of fine-grained soils. By developing a GSA, the influence of parameter variability on model predictions was quantified. This analysis revealed the main role played by the porosity and saturated hydraulic conductivity when multiphase flow affects the unsaturated zone. In particular, variability in the porosity explains almost completely the uncertainty associated with the contaminated unsaturated volume in case of sand and sandy loam, while the saturated hydraulic conductivity becomes more relevant when a loamy soil is considered. If the contamination reaches the saturated zone, volumes of groundwater affected by the plume are mainly influenced by the hydraulic conductivity, especially in case of sand; the porosity, hydraulic gradient and dispersivity also play a significant role with similar magnitude. On the contrary, when sandy-loam is considered as texture class, the influence of the hydraulic gradient and dispersivity decreases by about two orders of magnitude, while porosity assumes a role comparable with that of the hydraulic conductivity. In case of loamy soils, the probability of groundwater

to be affected by the contamination is significant only if the water table depth is very high. In general, the impact of the uncertainty in the unsaturated soil parameters is almost negligible in each considered scenario. It is possible to note that these results depend on the interpretation provided by the selected full model of the physical and chemical processes occurring in the subsurface domain. Uncertainty related to contaminated volumes significantly affect prediction of remediation costs. This is relevant when computing environmental risk indices of Bonvicini et al., 2015. The results indicate that reducing uncertainty in the parameters toward which model responses are most sensitive increases the accuracy of predictions and facilitates design of appropriate remediation actions.

Chapter 4

Probabilistic construction of climate scenarios for the quantitative assessment of groundwater at river-basin scale

Sommario

In questo capitolo si presenta uno studio a scala di bacino che mira ad indagare l'impatto dei cambiamenti climatici sulla disponibilità di risorsa idrica sotterranea entro un orizzonte temporale di riferimento. A tal scopo, si considera, quale caso studio, la conoide del fiume Trebbia, corpo idrico sotterraneo di grande rilevanza in Regione

Emilia-Romagna. Se la valutazione sullo stato quantitativo del corpo idrico al 2015 era risultata buona, la previsione condotta da Arpae E-R (ER, 2015a) al 2021 evidenzia possibili criticità in particolare per il comparto freatico.

In questo capitolo, lo studio condotto mira a definire una metodologia generalizzabile per la valutazione del rischio quantitativo associato ad un dato corpo idrico sotterraneo. Nello specifico si è preso come orizzonte temporale di interesse il 2050 e si sono considerate le corrispondenti previsioni fornite dall'IPCC (IPCC, 2015).

E' stato contemporaneamente calibrato un modello numerico in MODFLOW, rappresentativo della conoide, sfruttando dati disponibili nel decennio 2002-2011.

Per valutare l'impatto dei cambiamenti climatici al 2050, si sono costruiti degli scenari di ricarica, conseguenti alle variazioni previste di pioggia e temperatura.

Partendo dalle previsioni medie dell'IPCC per il trentennio 2021-2050, basato sullo scenario emissivo RCP 4.5, opportunamente regionalizzato, si è utilizzato lo Stochastic Collocation Method (v. Section 2.4.2) per la definizione degli scenari climatici. Ciò costituisce un approccio innovativo utile a superare i limiti associati a (i) l'analisi del solo scenario di previsione medio, (ii) l'analisi di molteplici scenari costruiti combinando gli estremi di variazione di pioggia e temperatura, incapaci di cogliere eventuali punti stazionari sulla superficie di risposta associata alla variabile di interesse, (iii) l'analisi di un numero molto elevato di scenari basato su simulazioni di tipo Monte Carlo.

Lo SCM consente di investigare la regione associata alla massima probabilità di accadimento nello spazio dei parametri incerti. Come già

evidenziato, lo SCM è stato generalmente impiegato in letteratura per trattare l'incertezza associata ai parametri (idraulici, idrogeologici, chimici, ecc.) caratteristici del dominio e dei fluidi/sostanze che vi si muovono all'interno.

In questo capitolo si mostra come l'applicazione dello SCM può essere estesa all'individuazione di un set ottimale di scenari, capaci di catturare la variabilità della forzante climatica.

Tali scenari possono essere applicati al modello numerico e, con l'ausilio della PCE (Section 2.4.1), possono condurre alla stima dell'impatto complessivo su una o più variabili di stato di interesse.

In ultimo, ciò rappresenta la base ideale per l'analisi di rischio quantitativo associata al corpo idrico e la definizione di opportuni indicatori di sintesi.

4.1 Case study

4.1.1 Trebbia alluvial fan

The Trebbia alluvial fan is characterized, on a regional scale, by greater extension of the unconfined compartment; this conoid is also the largest, in terms of size, among those located in the Province of Piacenza (Figure 4.1). The main inhabited centers insisting on the groundwater body are Podenzano and Piacenza cities, where the major water withdrawals are concentrated. Analyzing the land use map (version 2008 ed. 2011) produced by the Emilia-Romagna Region (for more details, see geoportale.regione.emilia-romagna.it), it emerges that the predominant land use over the basin is agricultural, followed

by natural and urbanized area.

The conoid of the Trebbia River falls within the category of the major Apennine alluvial fans of the Emilia-Romagna Region. Following the scheme of aquifers of the Emilia-Romagna Region (ER, 2015b) shown in Figure 4.2, the Trebbia fan consists of several alternations of coarse and fine deposits of variable thickness with a well-recognized stratification. Close to the Apennine margin (southern zone), highly permeable deposits that extend up to a few hundred meters in the subsoil are identified. In this area, a phreatic (monolayer) aquifer is recharged directly from rain and river supplies. In the northern zone, instead, an unconfined aquifer and a lower confined (multilayer) aquifer, progressively compartmentalized, not directly connected to the surface, coexist. In this case, the recharge is indirect, generally deriving from the unconfined aquifer (Lauriola, Ciriello, and Marcaccio, 2015; Ferri and Marcaccio, 2015).

4.1.2   Status and risk assessment of the fan

As regards to the quantitative status of Trebbia alluvial fan, the assessment made by Arpae Emilia-Romagna, using classification test shown in Sections 1.1.1 and 1.1.2, at the end of last River Basin Management Plan (RBMP) (2015) reveals that both the unconfined and lower confined aquifers are in "good status". On contrary, risk assessment at the end of the current RBMP (2021) delineates possible criticalities for the unconfined compartment (ER, 2015a). In order to assess groundwater quantitative status risk, Guidance Document n.18 (EC, 2009) provides a specific test on water balance (Figure 4.1.2). Specifically, it suggests verifying the status of good on the basis of dif-
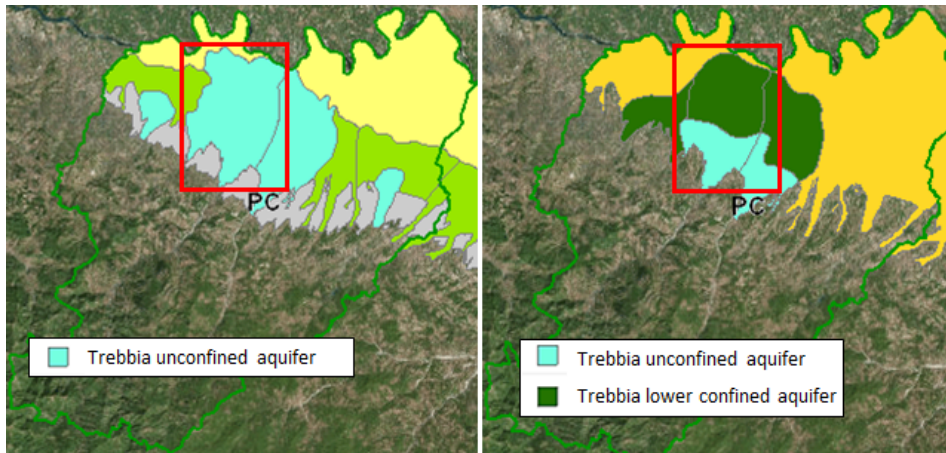
Figure 4.1: Trebbia alluvial fan, Province of Piacenza (cartografia ambientale, Arpae Emilia-Romagna).
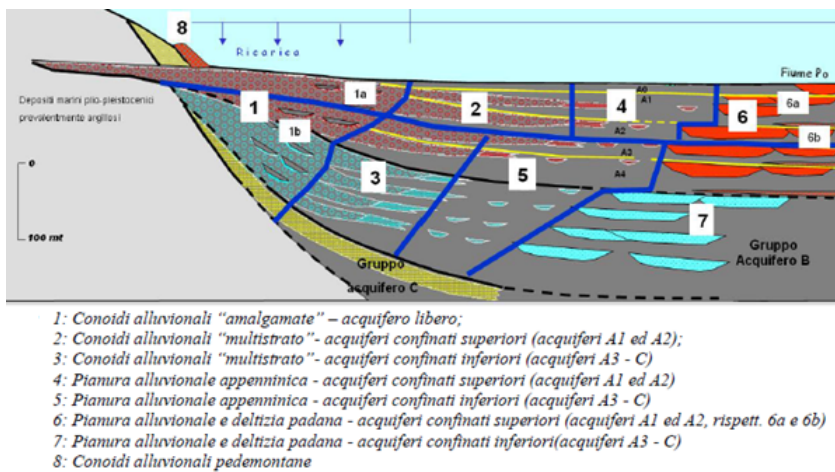

Figure 4.2: Geological scheme of the Emilia-Romagna aquifers identified in accordance with the WFD (ER, 2015b).

ference between the Long-Term Annual Average abstraction (LTAAQ)
and the Available Groundwater Resources (AGR). The AGR corre-
sponds to the Long-Term Annual Average Recharge (LTAAR), net of
the long-term Ecological Flow Needs (EFN), necessary for the good
status of the terrestrial ecosystems and of the surface water bodies
connected with groundwater body. The quantitative status is good
if the natural resources available minus the water volumes necessary
for the good chemical, quantitative and ecological status of superficial
ecosystems are higher than withdrawals. This balance represents a
long-term analysis in which the water volumes considered are aver-
aged annual values relating to a representative hydrological period, in
any case not less than at least one basin management cycle (6 years)
(EC, 2009; ISPRA, 2016).

As stressed into the European guideline (EC, 2009) the basis for the
application of water balance test is the construction of a conceptual
model. To this end, in collaboration with Arpae E-R, a numerical
model in MODFLOW is built to mimic the behavior of the flow into
the aquifers.

Collection of climate and pumping data is performed to provide bound-
ary conditions to the model. The model is calibrated against data in
2002-2011.

Sections below provide details on data collection and the numerical
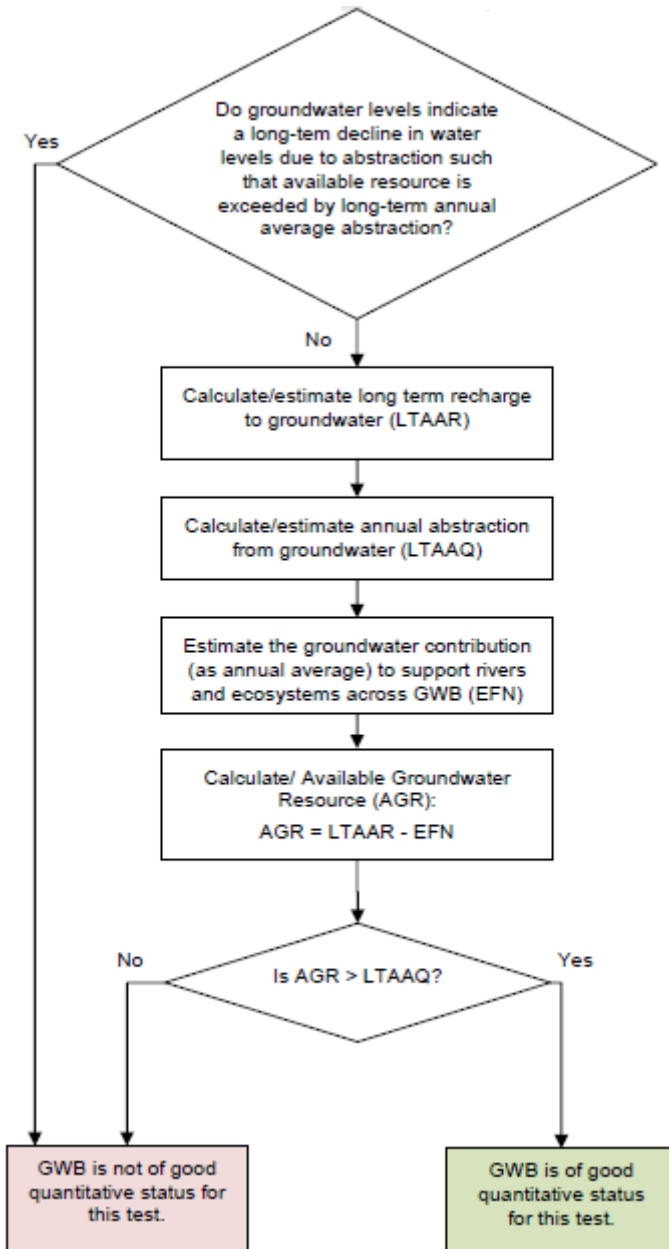model.

Figure 4.3: Procedure for water balance test (EC, 2009).

4.2 Data collection and processing

4.2.1 Data model in GIS

In order to build a preliminary conceptualization of the study area, a 3D model has been built in the GIS environment (Figure 4.4); the following data have been collected in the GIS model:

- Digital model elevation for the identification of basin's boundaries and drainage pathways;

- Land use at different years (1976; 1994; 2003; 2008) to capture the variations and to identify the main recharge areas associated with agricultural and natural land use;

- Climate data (precipitation, temperature) useful to estimate the natural recharge (time series: 2002-2011);

- Groundwater data such as aquifer bodies planimetric collocation, piezometric levels (time series: 2002-2011) and withdrawals (time series: 2002-2011).

Figure 4.5 shows some informative layers constituting the GIS model.

4.2.2 Climate data processing

By observing the geological structure of the fan, it is possible to note that the confined aquifer is only indirectly recharged by the phreatic compartment. As such, natural recharge is here computed
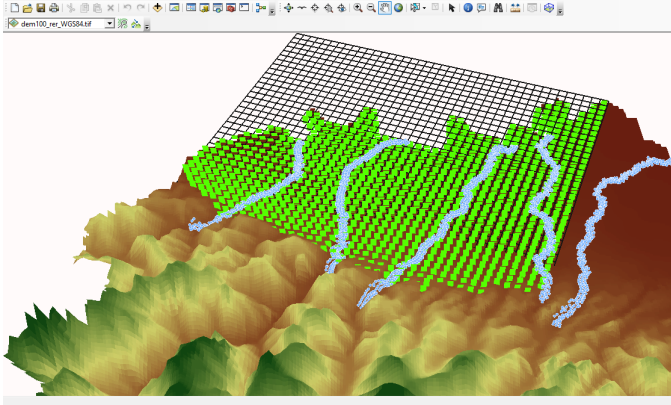
Figure 4.4: 3D model of study area in GIS environment.

with respect to the phreatic aquifer.

Estimation of natural recharge N is given by

$$N = R - ET_c - Q \qquad (4.1)$$

where R, ET_c, Q represent rainfall, potential evapotranspiration and runoff. All these terms are affected by climate change.

In order to compute ET_c it is first estimated the reference evapotranspiration, ET_0 following Hargreaves by means of a two parameters model:

$$ET_0 = \sum_{i=1}^{365} 0.0135 R_s \left(T_m + 17.8\right), \qquad (4.2)$$

where R_s is the incident solar radiation $(MJ/m^2/d^{-1})$, and T_m is the mean daily air temperature $(°C)$. This approach has been recognized by the FAO as an appropriate simplified alternative to the Penman–Monteith equation (Allen et al., 1998). In case solar radiation data
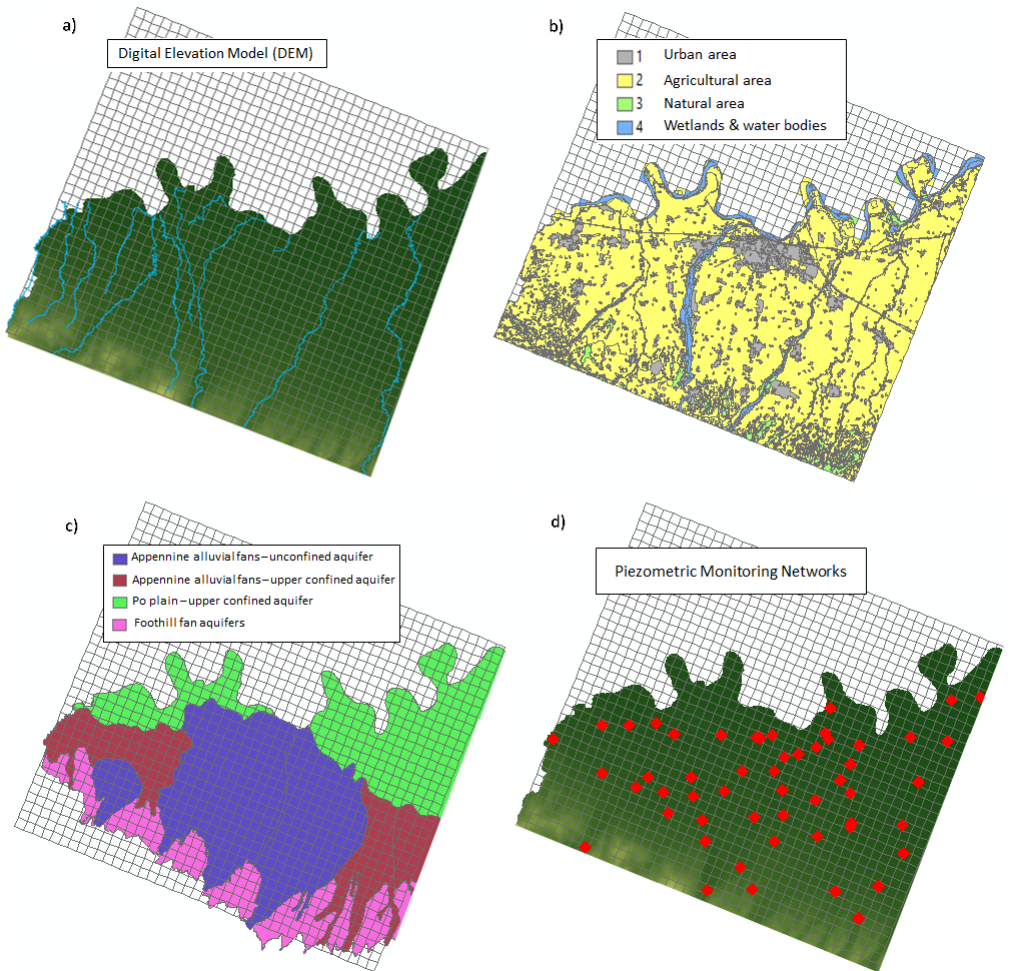
Figure 4.5: Information layers collected in GIS model: a)digital elevation model; b) land use layer; c)groundwater bodies layer; d) monitoring network stations.

are not available, the temperature-based approach suggested by Hargreaves and Samani (Hargreaves and Samani, 1982) can be employed to compute R_s as follows

$$R_s = R_a K_T \left(T_{max} - T_{min}\right)^{0.5},\tag{4.3}$$

where R_a is the extraterrestrial radiation ($MJ/m^2/d^{-1}$) which can be obtained for each day of the year and latitude. T_{max} and T_{min} are the maximum and minimum air temperature ($°C$), respectively; K_T is an empirical coefficient whose value typically varies within 0.16 (interior regions) and 0.19 (coastal regions). Combining (4.2)-(4.3) allows estimating ET_0 relying only on air temperature data.

Potential evapotranspiration ET_c, for agriculture and natural land uses, is obtained relying on the FAO approach as follows

$$ET_c = K_c ET_0,\tag{4.4}$$

where K_c is the crop coefficient.

Through the semi-empirical relationship hypothesized by Calera et al. (Calera et al., 2005) it is possible to correlate the Normalized Difference Vegetation Index (NDVI) obtained from satellite data to the crop coefficient Kc as follows

$$K_c = 1.25 NDVI + 0.2,\tag{4.5}$$

For K_c estimation, data of the MODIS satellite are used, aggregated on a monthly basis (product MOD13A3 V006), which allows monitoring the vegetation growth in the study area. K_c maps are then multiplied by monthly averaged maps of ET_0, obtained from the Arpae ERG-5 database (Emilia-Romagna Grid 5 km). Specifically, the latter is a

database implemented in Emilia-Romagna that provides weather daily data on a grid of 5 km side, interpolating measured data from regional meteorological stations. ERG-5 database has also been used to derive monthly averaged maps of precipitation.

Regarding to the runoff, it is estimated as a percentage of the precipitation which does not infiltrate in the vadose zone. Considering that the recharge area is devoted to agriculture, a runoff coefficient of 0.4 is considered.

FIGURE 4.6 shows variation of computed natural recharge in the period 2002-2011, for the purpose of model calibration. Each year is divided into quarters (named stress periods SP).
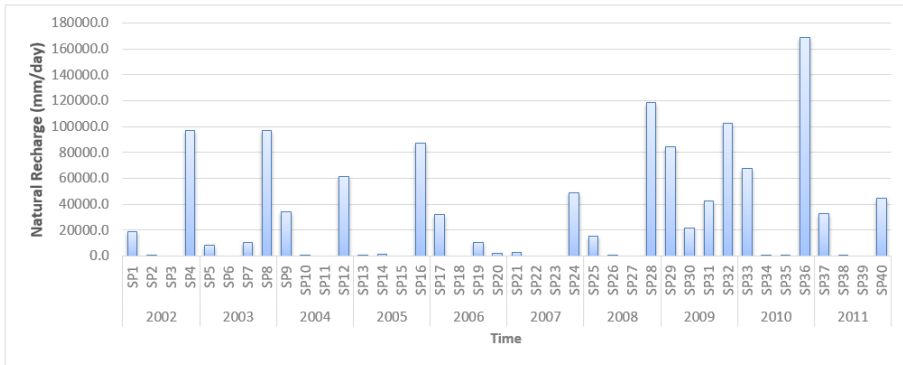

Figure 4.6: Total natural recharge (mm/day) for each stress period (SP) over the study area.

4.2.3 Pumping data processing

Pumping fluxes insisting on the phreatic (P_1) and confined (P_2) aquifers are estimated based on time series of water withdrawals for the period 2002-2011 (the same of climate data). The reference database consists of withdrawals related to the different uses (civil, industrial, irrigation and zootechnical); for each well, it is also available information on spatial location and filter depth (see Arpa, 2007, Arpa, 2009, ER, 2015a, for more details). Figure 4.7 shows the distribution of wells in the study area, while Figure 4.8 refers total pumping (m^3/day) insisting on the phreatic (P_1) and confined (P_2) aquifer for different uses in each stress period (SP).
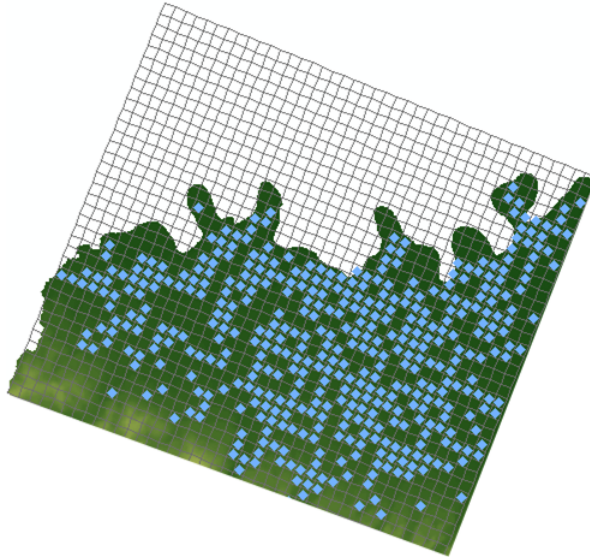

Figure 4.7: Spatial distribution of pumping insisting on Trebbia fan.

Figure 4.8: Total pumping (m^3/day) insisting on the phreatic (P_1) and confined (P_2) aquifer for different uses for each stress period (SP).

4.3 Numerical model

A conceptual model is built in MODFLOW (Harbaugh, 2005) and calibrated against available data in the period 2002-2011. In order to obtain a robust numerical model of the case study, we used a local clipping of the complete model of groundwater flow in the Emilia-Romagna Region is used(Emiro 3D) (Arpa, 2007). Therefore, of the entire regional aquifer, with an extension of about 12,000 km^2, only the area covered by the Conoid of the Trebbia River is considered (Figure 4.9). It has an extension of about 1516 km^2, developing planimetrically on 1516 cells of a length of 1 km and vertically on 35 layers characterized by cells with variable thickness. For each cell, it is also assigned a specific lithological class with hydrogeological parameters appropriately calibrated during the initial calibration phase of the numerical model (Arpa, 2007). With regards to the initial conditions, the following choices are made. An initial condition is imposed on the hydraulic head (Figure 4.10), obtained by kriging of piezometric data collected by Arpae E-R during groundwater monitoring campaigns (Arpa, 2008). In the superficial layers, in the northern area, the hydrometric level of the Po River is imposed as head condition, while in the southern area, corresponding to the Apennine margin, no flow condition is imposed. As for the boundary conditions, it was decided to simulate the effect of natural recharge and pumping as external forcing agents insisting on the system. The time step of the whole analysis is on quarterly basis, for a total of 40 stress periods.
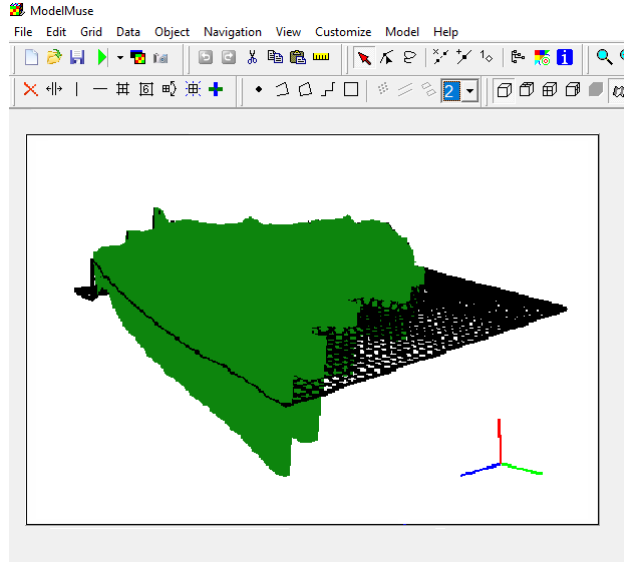
Figure 4.9: 3D numerical model of conoid Trebbia River in MOD-FLOW.

4.3.1   Numerical model output

The local numerical model, describing groundwater flow in the Trebbia fan, is compared in terms of head to the full regional scale model in the period 2002-2011. In addition, the Zonebudget is used to check if the water balance equation and the terms that compose each of the stress period are respected (Harbaugh, 1990). Terms of incoming and outgoing balance are calculated in terms of averaged flow rates for the single simulation period (m^3/s). In detail, the inputs correspond to the natural recharge and possible positive changes in the storage term. The outputs correspond to withdrawals and negative changes
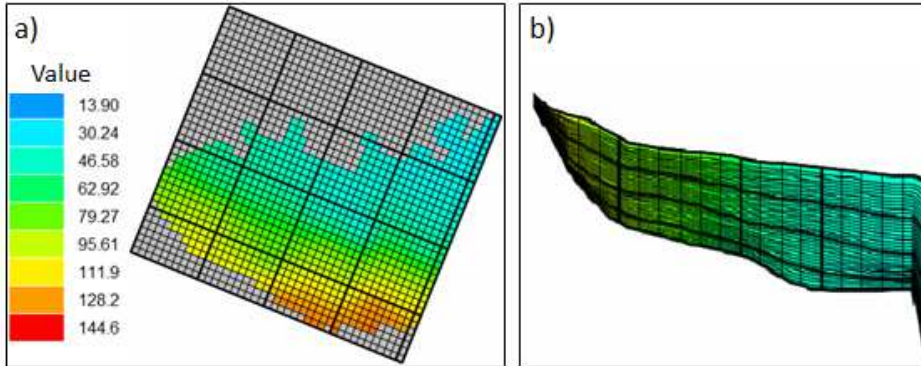
Figure 4.10: Model front view (a) and side view (b) of the initial head condition (m a.s.l.).

in storage. It follows that a positive change in the storage corresponds to a volume of water that is subtracted from the groundwater body, while a negative change to an accumulation of water resource. Figure 4.11 shows the trends of the water balance terms during the 40 simulation stress periods. From the analysis of the overall balance of the fan it is highlighted that the storage of water inside the system undergoes the dynamic withdrawals/recharge, reflecting the seasonal variation. In particular, in correspondence with the summer period, characterized by greater withdrawals, there is a reduction in the stored water resource, vice versa in periods of greater precipitation, there is an accumulation of water within the system.
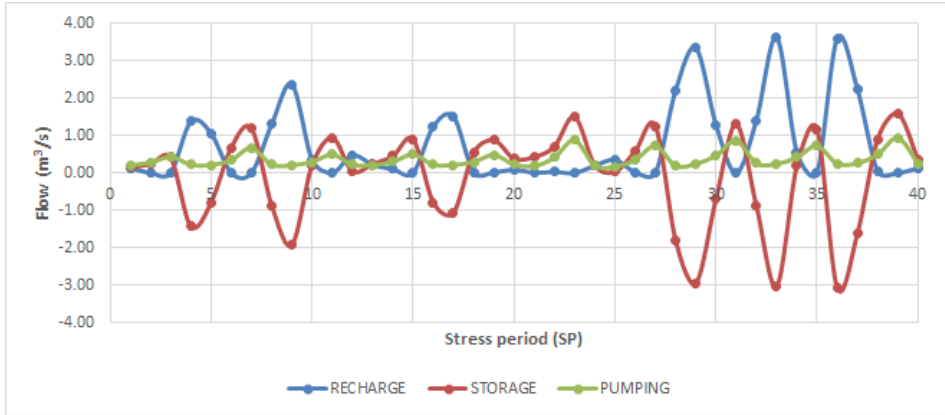
Figure 4.11: Zonebudget output: averaged flow rates of natural recharge, storage and wells (m^3/s) for Trebbia unconfined aquifer during 40 stress periods.

4.4   Climate change impacts on recharge

For the construction of recharge scenarios, climate variation on precipitation and temperature is considered. To this end, monthly averaged data of daily precipitation and mean temperature for the 30-years reference period 1971-2000 are collected; the stations are the same of those adopted for climate data collection in the period 2002-2011.

Employing the IPCC RCP 4.5 scenario and based on statistical regionalization techniques applied to a global climate model (CMCC-CM) (Antolini et al., 2017; IPCC, 2015), it is possible to evaluate future variations of temperature and precipitation for the period 2021-2050

respect to the reference period. Regional climate projections are collected in Table 4.1 and allow projecting forward precipitation and temperature for the years 2021-2050.

Table 4.1: Climate change projections for the Emilia-Romagna Region defined as expected variations of precipitation and temperature in 2021-2050 respect to 1971-2000.

Season	$\Delta T_{min}(°C)$	$\Delta T_{max}(°C)$	$\Delta P(\%)$
Winter	+1.7	+1.4	-2
Spring	+1.3	+2.1	-11
Summer	+1.8	+2.5	-7
Autumn	+1.7	+1.8	+19

4.4.1 Identification of random parameters

In order to identify multiple climate scenarios, built upon optimum combinations of precipitations and temperatures, a set of random variables are chosen; they consist of averaged data of daily precipitation associated with the four stress periods (P_{sp1}, P_{sp2}, P_{sp3}, P_{sp4}) and, similarly, averaged data of daily mean temperature (T_{sp1} T_{sp2} T_{sp3} T_{sp4}). Table 4.2 shows statistical distribution (pdfs), means (μ), and standard deviations (σ) of random parameters. These data correspond to the spatial average over the basin.

In order to build PCE surrogate models, following Section 2.4.1, the degree for the the expansion is set to $p=2$ (if necessary for accuracy reasons, it can be increased); consequently, with $M=8$ random parameters, the associated PCE is then composed by $P=45$ terms. The

Table 4.2: Statistical distribution and properties of the selected random parameters.

Parameter	μ	σ	PDF
P_{sp1}	1.85	0.96	logn
P_{sp2}	2.15	0.92	logn
P_{sp3}	2.30	1.29	logn
P_{sp4}	3.21	1.02	logn
T_{sp1}	5.95	1.10	logn
T_{sp2}	18.07	0.88	logn
T_{sp3}	23.77	0.85	logn
T_{sp4}	9.03	0.70	logn

adopted distributions for the parameters suggest to resort to Hermite multivariate polynomial basis. Therefore, PCE is expressed in terms of eight random variables, ξ_i (i=1,...8) representing standardized gaussian parameters which are related to (P_{sp1}, P_{sp2}, P_{sp3}, P_{sp4}, T_{sp1} T_{sp2} T_{sp3} T_{sp4}) through isoprobabilistic transformations. Combination of regression points (ξ_1, ..., ξ_8) are obtained by applying the stochastic collocation method (SCM), explained in Section 2.4.2, using a number of regression points N=P=45. These combinations are shown in Table 4.3.

Resulting recharge scenarios for the 45 combinations of precipitations and temperatures are shown in Figure 4.12. Finally, in Figure 4.13 is shown the average recharge scenario referring to the period 1971-2000, while Figure 4.14 the average recharge scenario for the period 2021-2050.
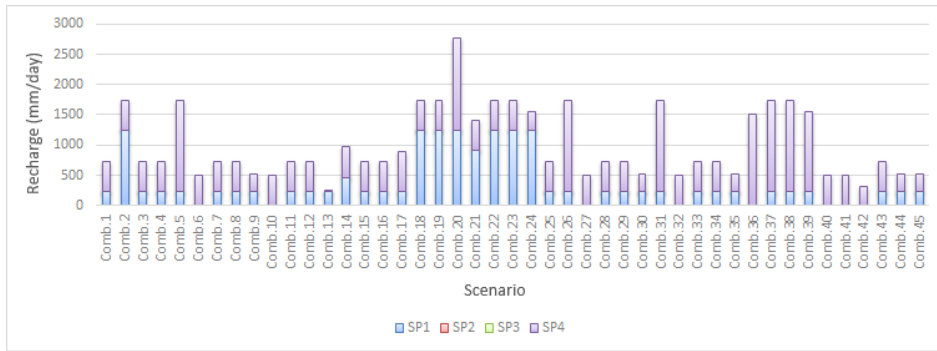

Figure 4.12: Scenarios of average natural recharge (mm/day) for each stress period (SP) over the study area.

4.4.2 Definition of the PCE

The expansion coefficients of PCE, i.e. a_i (i=1,...8), can be computed according to the regression-based approach discussed in Section 2.4.2. In this way is possible to obtain the second order PCE metamodel for any quantity of interest (QoI) as follows:

$$QoI = \sum_{i=1}^{P} a_i \Psi_i \left(\xi_1, ..., \xi_8 \right) \tag{4.6}$$

Table 4.3: Regression points for the selected polynomial function.

| Combination	ξ_1	ξ_2	ξ_3	ξ_4	ξ_5	ξ_6	ξ_7	ξ_8
Comb. 1	0	0	0	0	0	0	0	0
Comb. 2	1.73	0	0	0	0	0	0	0
Comb. 3	0	1.73	0	0	0	0	0	0
Comb. 4	0	0	1.73	0	0	0	0	0
Comb. 5	0	0	0	1.73	0	0	0	0
Comb. 6	0	0	0	0	1.73	0	0	0
Comb. 7	0	0	0	0	0	1.73	0	0
Comb. 8	0	0	0	0	0	0	1.73	0
Comb. 9	0	0	0	0	0	0	0	1.73
Comb. 11	-1.73	0	0	0	0	0	0	0
Comb. 12	0	-1.73	0	0	0	0	0	0
Comb. 13	0	0	-1.73	0	0	0	0	0
Comb. 14	0	0	0	-1.73	0	0	0	0
Comb. 15	0	0	0	0	-1.73	0	0	0
Comb. 16	0	0	0	0	0	-1.73	0	0
Comb. 17	0	0	0	0	0	0	-1.73	0
Comb. 18	1.73	1.73	0	0	0	0	0	0
Comb. 19	1.73	0	1.73	0	0	0	0	0
Comb. 20	1.73	0	0	1.73	0	0	0	0
Comb. 21	1.73	0	0	0	1.73	0	0	0
Comb. 22	1.73	0	0	0	0	1.73	0	0
Comb. 23	1.73	0	0	0	0	0	1.73	0
Comb. 24	1.73	0	0	0	0	0	0	1.73
Comb. 25	0	1.73	1.73	0	0	0	0	0
Comb. 26	0	1.73	0	1.73	0	0	0	0
Comb. 27	0	1.73	0	0	1.73	0	0	0
Comb. 28	0	1.73	0	0	0	1.73	0	0
Comb. 29	0	1.73	0	0	0	0	1.73	0
Comb. 30	0	1.73	0	0	0	0	0	1.73
Comb. 31	0	0	1.73	1.73	0	0	0	0
Comb. 32	0	0	1.73	0	1.73	0	0	0
Comb. 33	0	0	1.73	0	0	1.73	0	0
Comb. 34	0	0	1.73	0	0	0	1.73	0
Comb. 35	0	0	1.73	0	0	0	0	1.73
Comb. 36	0	0	0	1.73	1.73	0	0	0
Comb. 37	0	0	0	1.73	0	1.73	0	0
Comb. 38	0	0	0	1.73	0	0	1.73	0
Comb. 39	0	0	0	1.73	0	0	0	1.73
Comb. 40	0	0	0	0	1.73	1.73	0	0
Comb. 41	0	0	0	0	1.73	0	1.73	0
Comb. 42	0	0	0	0	1.73	0	0	1.73
Comb. 43	0	0	0	0	0	1.73	1.73	0
Comb. 44	0	0	0	0	0	1.73	0	1.73
Comb. 45	0	0	0	0	0	0	1.73	1.73
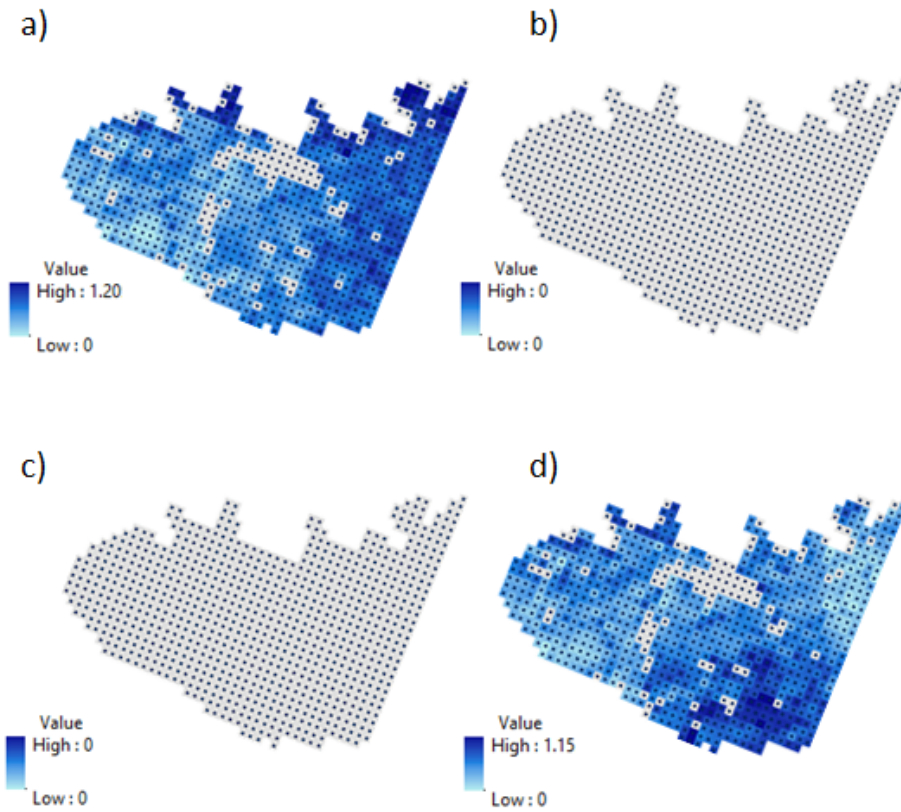
Figure 4.13: Average recharge scenario (mm/day) referring to the period 1971-2000. a) Stress period SP_1, b) Stress period SP_2, c) Stress period SP_3, d) Stress period SP_4.
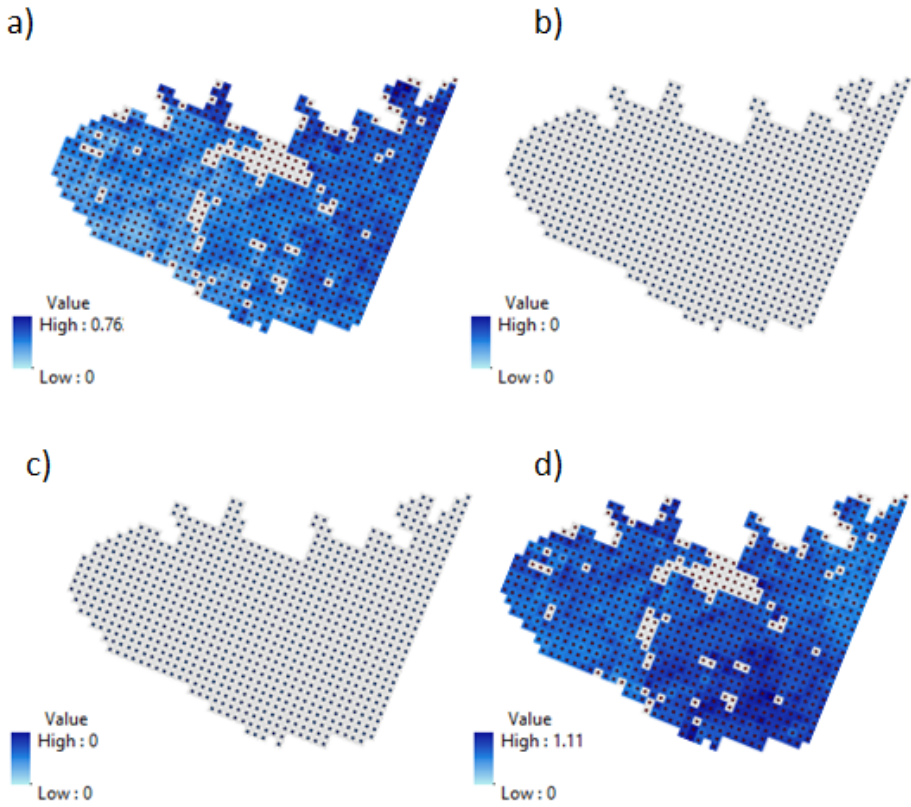
Figure 4.14: Average recharge scenario (mm/day) referring to the period 2021-2050. a) Stress period SP_1, b) Stress period SP_2, c) Stress period SP_3, d) Stress period SP_4.

The potentiality of the approach lies in the possibility of deriving a surrogate model of any quantity of interest that is only a function of the considered random parameters. For the selected case study, possible quantities of interest can be identified e.g.in the average piezometric level variation in a given region of the aquifer, or in the water volumes stored in the groundwater bodies or in the input terms of the above-mentioned water balance test.

This method is completely innovative as it can define quantities of interest through a stochastic approach and can be used for the formulation of new risk assessment indices linked to the quantitative status of groundwater bodies, as required by the European Directives.

4.5 Final remarks

In this chapter, the study led to the definition of a new methodology for the quantitative risk assessment associated with groundwater bodies. For the definition of the environmental status, the current legislation requires an integrated analysis at the river basin scale and the definition of a conceptual model for the selected groundwater body. For this purpose, a numerical model of the conoid of the Trebbia River was realized and it was appropriately calibrated using data of the decade 2002-2011.

In order to assess the effects that climate change may have on the quantitative status of the selected water body, multiple recharge scenarios were constructed, combining the expected precipitation and temperature variations based of RCP 4.5 emission scenario provided by the IPCC. The innovative application of the SCM in this field allowed

to define an optimal set of scenarios, capable of capturing the variability of precipitations and temperatures due to the climate change. These scenarios can be applied to the numerical model and by means of PCE can lead to the estimate of the overall impact on one or more state variables of interest. Results obtained from this approach can be useful to define appropriate quantitative risk assessment indicators associated with the groundwater body. The methodology can be also applied to assess the impacts of anthropic pressures (which may vary as well) at the same time.

Chapter 5

Estimation of soil moisture trough radio waves transmission: a Global Sensitivity Analysis study

Sommario

L'umidità del suolo è un parametro chiave che regola l'equilibrio idrico del suolo e influenza i processi idrologici come l'infiltrazione dell'acqua e l'evapotraspirazione, componenti fondamentali per la stima degli apporti di ricarica nelle falde acquifere. La comprensione di tali processi ha importanti ricadute in diversi campi di applicazione relativi alle risorse idriche, tra cui l'agricoltura di precisione e la gestione della siccità.

Per la stima sul campo dell'umidità del suolo, i metodi indiretti sono
generalmente preferiti in quanto non sono invasivi e le misure posso-
no essere rilevate in continuo nel tempo. Tra i metodi indiretti, si
analizzano, in particolare, le Wireless Underground Communication
Networks (WUCNs), tecnica promettente basata sulla trasmissione di
onde radio a uno o più sensori posizionati nel sottosuolo a specifiche
profondità. Dalle misurazioni della perdita del segnale elettromagneti-
co e in base ai modelli di propagazione delle onde a percorso singolo o
a due percorsi, è possibile ricavare informazioni sull'umidità del suolo.
Lo studio presentato in questo capitolo ha prodotto la pubblicazione
**"Impacts of uncertainty in soil texture parameters on esti-
mation of soil moisture through radio waves transmission",
Advances in Water Resources, Vol. 122 pp 131-138, (E. Di
Fusco, I. Lauriola, R. Verdone, V. Di Federico, V. Ciriel-
lo, 2018)**. In questo lavoro, l'analisi di Sensitività Globale (GSA)
basata sulla varianza (v. Capitolo 2) viene applicata per studiare
la propagazione dell'incertezza associata ai parametri tessiturali del
suolo nelle stime del contenuto d'acqua. Questo è fondamentale per
identificare quali grandezze parametriche richiedono misurazioni più
accurate e per guidare la progettazione di campagne di ispezione sul
campo. Nello specifico, la GSA è stata eseguita su un modello ricavato
dalle equazioni delle onde elettromagnetiche e coadiuvato da relazio-
ni semiempiriche che definiscono le proprietà dielettriche del suolo in
funzione della porosità del suolo e delle percentuali di contenuto di
argilla e sabbia, nell'intervallo di frequenza di trasmissione $0.3 \div 1.3$
GHz. Il modello matematico risultante è stato successivamente ridot-
to mediante la tecnica della Espansione in Chaos Polinomiale (PCE).

Ricorrendo alla metamodellazione, è stato possibile approssimare la superficie di risposta della quantità di interesse, nel caso specifico la perdita di potenza del segnale, per diversi valori di umidità del suolo e di frequenza operativa, nello spazio parametrico dato dalla pdf congiunta dei parametri tessiturali considerati incerti.

5.1 Introduction

5.1.1 Wireless underground communication networks

Soil moisture is a key quantity in the field of drought management and to close the soil water balance in hydrologic modeling. It also plays a critical role in precision agriculture for enabling flexible and smart irrigation strategies (e.g. Narasimhan and Srinivasan, 2005; Sheffield and Wood, 2008; Martínez-Fernández et al., 2015; Huang et al., 2017; Moghadas, Jadoon, and McCabe, 2017; Ahmad et al., 2018). Soil moisture can be measured directly through the gravimetric method, which is however a destructive time-consuming approach, difficult to use in practical applications. Due to these limitations, several indirect methods have been developed to provide a measure of another quantity that can be related to soil moisture through physically based and empirical equations. A widely used technology, focused on dielectric measurements, is time domain reflectometry (TDR), which has shown to be more accurate and economical if compared to frequency domain reflectometry (FDR). However, both these technologies provide local scale (single point) measures. In order to move towards field

scale measures one may resort to geophysical methods such as ground penetrating radar (GPR), that is however an expensive technology, or electrical resistivity measurements, with the disadvantage that data acquisition is periodic or requires regular field surveys (for more details on indirect methods see e.g. Bittelli, 2011; Dobriyal et al., 2012, and references therein).

In this context, a recent and promising monitoring technique consists (in the basic configuration) of two radio transceivers (hereinafter denoted as devices), buried underground, that can exchange signals and make possible to provide indirect estimates of soil moisture without the need for an ad hoc device, based on the idea that radio waves propagate through the soil with a loss rate which depends on the volumetric water content (e.g., Akyildiz and Stuntebeck, 2006; Akyildiz, Sun, and Vuran, 2009; Vuran and Silva, 2009; Dong, Vuran, and Irmak, 2013, and references therein). In addition, this approach provides an average estimate over the transmission volume instead of a single point measure. Soil moisture is measured locally and then transmitted by the receiving node to a surface gateway. The latter will forward data to the Internet through, e.g., a UAV repeater flying above the area. Measuring soil moisture at 30-100 cm depth through devices connected to the Internet may provide critical real time information for several applications.

LoRa is a novel wireless technology for the IoT (Internet of Things) even much more robust to power losses than its predecessors. LoRa operates on ISM bands that are available in the world on a Region and Country-level basis. In ITU Region 1, including Europe, the 863 MHz - 870 MHz frequency range can be used by LoRa devices. However,

in Countries like Italy, the availability of the band is limited to the range 868-870 MHz. In Region 2 (Americas), the available frequency range is 902 MHz - 928 MHz. From the viewpoint of the underground propagation channel, it is expected that no major differences are found between these options. The LoRa technology can provide successful detection of data pockets suffering a power loss of up to 151 dB, when very low data rates are needed. Theoretically, such margin to loss enables to link zones of up to 10 m underground, depending on soil texture and moisture, and the antenna type.
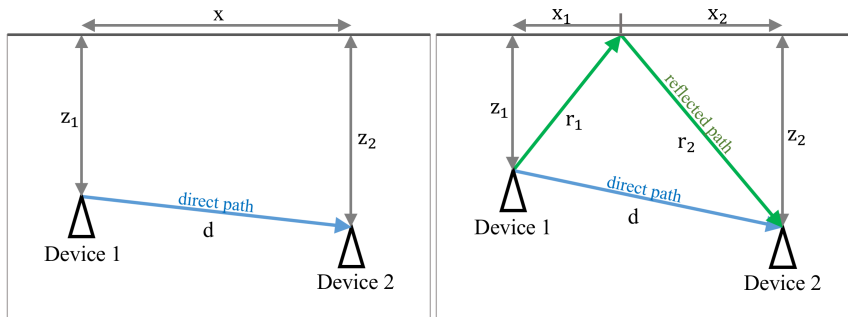

Figure 5.1: Possible configurations of WUCNs. In the left panel a single path transmission is depicted, while in the right panel a two-path transmission mechanism is shown due to the reflection produced by the ground surface.

5.1.2 Mathematical foundation

EM wave propagation in soil can be described with a link budget based on the Friis equation with an additional term accounting for the

attenuation induced by the soil with respect to free space propagation
(e.g. Li, Vuran, and Akyildiz, 2007, and references therein). The power
of the received signal, P_r $[dB]$, is computed as follows:

$$P_r = P_t + G_r + G_t - L_0 - L_s \qquad (5.1)$$

where P_t $[dB]$ is the transmitted power, G_r $[dB]$ and G_t $[dB]$ are the
gains of the receiver and transmitter antennae respectively, L_0 $[dB]$ is
the path loss in free space and L_s $[dB]$ the additional path loss due to
the soil. These losses are given by:

$$L_0 = 20log\left(4\pi d/\lambda\right), \qquad (5.2)$$

$$L_s = L_\beta + L_\alpha = 20log\left(\lambda_0/\lambda\right) + e^{2\alpha d}, \qquad (5.3)$$

where d $[m]$ is the distance between devices, L_β $[dB]$ is due to the
difference of signal wavelength in soil, $\lambda = 2\pi/\beta$, with respect to the
same in free space, $\lambda_0 = c/f$, with β $[rad/m]$ the phase shifting con-
stant and f $[Hz]$ the operating frequency; L_α $[dB]$ is the transmission
loss caused by attenuation with attenuation constant α $[1/m]$.

Both α and β depend on the dielectric properties of soil: the per-
meability, μ $[H/m]$, the conductivity, σ $[S/m]$, and the permittivity,
ε $[F/m]$. Let's consider the Helmholtz equations (written in terms of
phasor vector equations):

$$\nabla^2 E_s - \gamma^2 E_s = 0 \quad \nabla^2 H_s - \gamma^2 H_s = 0, \qquad (5.4)$$

where E_s is the phasor vector associated with the electric field E $[V/m]$
through the relationship $\partial E/\partial t = i\omega E_s$; the same holds for H_s which is
the phasor vector associated with the magnetic field H $[A/m]$ (Balanis,
2012).

In (5.4), γ is the propagation constant, which is defined as follows

$$\gamma = \sqrt{i\omega\mu(\sigma + i\omega\varepsilon)}, \tag{5.5}$$

where ω $[rad/s]$ is the angular frequency ($\omega = 2\pi f$). By imposing $\gamma = \alpha + i\beta$, from (5.5), it is possible to derive the following expressions for α and β as functions of the dielectric soil properties:

$$\alpha, \beta = \omega\sqrt{\frac{\mu\varepsilon}{2}\left[\sqrt{1 + \left(\frac{\sigma}{\omega\varepsilon}\right)^2} \mp 1\right]}. \tag{5.6}$$

5.1.3 Impact of soil texture on measurements

Given that the soil consists in a multiphase medium of air, water (both bound and free) and bulk soil, EM wave propagation is generally facilitated in case of low soil density and high porosity combined with low water contents, as the rate of air presence is larger under these conditions. The volumetric moisture content provides a critical contribution to the EM wave attenuation. It includes information about the presence of bound and free water at a time; soil texture analysis, and specifically the quantity of clay in the soil, allows one to distinguish among these two contributions.

Frequency also affects the dielectric constants. The range of frequencies used in practical applications is $0.3 \div 1$ GHz, which is associated with reasonable dielectric constants for wireless communication and feasible sizes of the antenna.

From a geometrical point of view, the distance between devices also plays a role as well as the burial depth; in case of low depths underground (generally $< 0.3 \div 0.5$ m) the ground surface produces a

reflection/refraction effect which has to be considered. In this case, the received signal consists of two components: a direct path from the transmitter to the receiver and a reflecting path due to the ground surface; a two-path model has to be preferred in this case with respect to the single path conceptualization (see Figure 5.1).

The path loss increases with frequency and distance between devices, and is affected by soil moisture and texture in turn. If one uses WUCNs to estimate soil moisture, it is critical to perform preliminary analysis to properly design measurement campaigns under specific field conditions. In particular, it is relevant to identify the influence of soil texture parameters on path loss values, given the uncertainty which typically characterizes the subsurface environment and specifically the vadose zone (e.g., Tartakovsky, 2013; Assouline, Ciriello, and Tartakovsky, 2017; Brandhorst, Erdal, and Neuweiler, 2017).

5.2 Methodology

5.2.1 Equations

A single path model to study EM wave propagation through the soil at high burial depths (typically > 0.5m) is considered. In this case, from (5.2)-(5.3), it is possible to represent the overall path loss, L_p, in dB as follows (Vuran and Silva, 2009):

$$L_p = L_0 + L_s = 6.4 + 20\mathrm{log}d + 20\mathrm{log}\beta + 8.69\alpha d. \qquad (5.7)$$

Based on (5.5) and introducing the complex permittivity of the medium $\varepsilon_c = \varepsilon \left[1 - i\left(\frac{\sigma}{\omega\varepsilon}\right)\right] = \varepsilon' - i\varepsilon''$ (both ε' and ε'' are in F/m), constants

α and β can be rewritten as

$$\alpha, \beta = \omega \sqrt{\frac{\mu \varepsilon'}{2} \left[\sqrt{1 + \left(\frac{\varepsilon''}{\varepsilon'}\right)^2} \mp 1 \right]}. \tag{5.8}$$

The semi-empirical model proposed by Peplinsky et al. (Peplinski, Ulaby, and Dobson, 1995) provides expressions for ε' and ε'' as

$$\varepsilon' = 1.15 \left[1 + \frac{\rho_b}{\rho_s} \left(\varepsilon_s^{\alpha'} - 1 \right) + m_v^{\beta'} \left(\varepsilon'_{fw} \right)^{\alpha'} - m_v \right]^{\frac{1}{\alpha'}} - 0.68, \tag{5.9}$$

$$\varepsilon'' = \left[m_v^{\beta''} \left(\varepsilon''_{fw} \right)^{\alpha'} \right]^{\frac{1}{\alpha'}}, \tag{5.10}$$

where m_v [$-$] is the volumetric moisture content, $\rho_s = 2.66\text{g/cm}^3$ is the specific density of solid soil particles, and $\rho_b = \rho_s \left(1 - n \right)$ is the bulk density, with n [$-$] the soil porosity; $\alpha' = 0.65$ and $\varepsilon_s = 4.7$ F/m , which is the soil solid permittivity, are empirically determined constants (Dobson et al., 1985), while β' and β'' are empirically determined as functions of soil texture based on mass fractions of sand (S = sand mass / total dry mass) and clay (C = clay mass / total dry mass): $\beta' = 1.2748 - 0.519S - 0.152C$, $\beta'' = 1.33797 - 0.603S - 0.166C$. The quantities ε'_{fw} [F/m] and ε''_{fw} [F/m] are the real and imaginary parts of the relative dielectric constant of free water given by

$$\varepsilon'_{fw} = \varepsilon_{w\infty} + \frac{\varepsilon_{w0} - \varepsilon_{w\infty}}{1 + \left(2\pi f \tau_w \right)^2}, \tag{5.11}$$

$$\varepsilon''_{fw} = \frac{2\pi f \tau_w \left(\varepsilon_{w0} - \varepsilon_{w\infty} \right)}{1 + \left(2\pi f \tau_w \right)^2} + \frac{\sigma_{eff} \left(\rho_s - \rho_b \right)}{2\pi f \varepsilon_0 \rho_s m_v}, \tag{5.12}$$

where f $[Hz]$ is the frequency, τ_w $[s]$ is the relaxation time for water, $\varepsilon_{w0} = 80.1$ F/m (at20°C) is the static dielectric constant for water, $\varepsilon_{w\infty} = 4.9$ F/m is the high-frequency limit of ε'_{fw}, and ε_0 $[F/m]$ is the permittivity of free space. Peplinsky et al. (Peplinski, Ulaby, and Dobson, 1995) provide a value of 0.58×10^{-10}s for the product $2\pi\tau_w$ and define, for a range of low frequencies $[0.3 \div 1\text{GHz}]$, an empirical equation to estimate the effective conductivity $[S/m]$: $\sigma_{eff} = 0.0467 + 0.2204\rho_b - 0.4111S + 0.6614$.

In case of devices buried in proximity of the ground surface, it is necessary to consider a two-path model to account for the reflection effect on the underground signal propagation (Li, Vuran, and Akyildiz, 2007). In this case, the total path loss is defined in dB as

$$L_f = L_p - V_{dB}, \tag{5.13}$$

where $V_{dB} = 10logV^2$ $[dB]$ is the attenuation factor due to the second path, and $V^2 = 1 + \left(\Gamma e^{-\alpha\Delta r}\right)^2 - 2\Gamma e^{-\alpha\Delta r}cos\left(\pi - \phi + 2\pi/\lambda\Delta r\right)$; $\Delta r = r - d$ $[m]$ is the difference between the two paths, Γ and ϕ the amplitude and phase angle of the reflection coefficients at the reflection point (Vuran and Silva, 2009).

5.2.2   Global sensitivity analysis application

Variabilies of porosity (n), and sand and clay contents (S, C) reflect the uncertainty in soil texture. For the sake of simplicity and consistency with the model presented in section 5.2.1, a zonation approach is adopted (Ciriello et al., 2017) and it is assumed that the soil consists of a single uniform stratum of either clay-loam (CL), loam (L) or sandy-loam (SL). To each type of soil the mean and standard

deviation identified by Carsel and Parrish (Carsel and Parrish, 1988) is assigned, as presented in Table 5.1. GSA (see Section 2.3) is applied to identify, for each soil, the regions of influence of soil texture parameters in the (m_v, f, d) space. To do this, a truncated polynomial chaos expansions (PCE) Wiener, 1938 (see Section 2.5) is derived which approximates L_p as

$$L_p(m_v, f, d; \mathbf{P}) \approx \sum_{j=0}^{P-1} a_j(m_v, f, d) \Psi_j(\mathbf{P}), \quad P = \frac{(M+p)!}{M!p!}, \quad (5.14)$$

where $\mathbf{P} = \{n, S, C\}$ is the vector of uncertain texture parameters, and $\Psi_j(\mathbf{P})$ denotes multivariate Hermite polynomials. The Stochastic Collocation (SC) method (Webster, Tatang, and McRae, 1996) (see Section 2.4.2) is used to compute the deterministic expansion coefficients a_j. The zero-order coefficient, $a_0(m_v, f, d)$, corresponds to the mean of L_p, i.e., $\langle L_p(m_v, f, d) \rangle = a_0(m_v, f, d)$. The variance of L_p is computed as

$$\sigma_{L_p}^2(m_v, f, d) = \sum_{j=1}^{P} a_j^2(m_v, f, d) \langle \Psi_j^2(\mathbf{P}) \rangle, \quad (5.15)$$

which is derived from (5.14) by accounting for the orthogonality of the Hermite polynomials, $\langle \Psi_i \Psi_k \rangle = 0$ for all $i \neq k$. The SC is well suited for the low-dimensional probability spaces, such as $M = 3$ considered in the present study (e.g., Ciriello et al., 2013c; Ciriello et al., 2013a; Ciriello et al., 2015, and the references therein).

The Sobol' indices (Sobol', 1993) provide a metric of the relative impact of each parameter affected by uncertainty (see Table 5.1) on the overall predictive uncertainty, as quantified by (5.15). The contribution of the ith parameter, P_i to the response variance is quantified

by a "principle sensitivity index" $\mathcal{S}_i$, which is defined, based on the PCE approximation, by Sudret, 2008

$$\mathcal{S}_i(m_v, f, d) = \frac{\sigma^2_{L_p,i}}{\sigma^2_{L_p}}, \qquad \sigma^2_{L_p,i}(m_v, f, d) = \sum_{\gamma \in \Gamma_i} a^2_\gamma(m_v, f, d)\langle \Psi^2_\gamma(P_i)\rangle,$$

(5.16)

where $\Gamma_i = \{\gamma \in (1, \ldots, N_Q - 1) : \Psi_\gamma(P_i)\}$. This definition can be easily extended to evaluate the joined influence of a subset of model parameters, in case that principle sensitivity indices do not provide a full description of the response variance. The Sobol indices computed for all the possible subsets of parameters sum up to unity (Sobol', 1993).

Global sensitivity metrics, including the Sobol' indices, are generally computed by means of Monte Carlo simulations (Sobol', 2001). However, depending on the complexity of model equations and the number of uncertain parameters, the deriving computational cost may discourage the use of global approaches for sensitivity analysis. In these cases, metamodeling techniques (among which PCE is one option) represent powerful tools to accelerate the computational cost associated with GSA and other onerous stochastic analyses. For the purposes of this study, the approximation of the response surface with PCE is build upon soil texture uncertainty, while leaving information on the variability of operating conditions (d and f) within the deterministic coefficients a_j. This is done to distinguish among epistemic uncertainty and response variability due to the design/operating parameters.

Table 5.1: Statistical distributions (PDFs) and properties (mean, $\langle \cdot \rangle$, and standard deviation, σ) of the uncertain model parameters.

Parameter	PDF	clay-loam	loam	sandy-loam
n	Normal	$\langle n \rangle = 0.41$	$\langle n \rangle = 0.43$	$\langle n \rangle = 0.41$
		$\sigma_n = 0.09$	$\sigma_n = 0.10$	$\sigma_n = 0.09$
S	Lognormal	$\langle S \rangle = 29.8$	$\langle S \rangle = 40$	$\langle S \rangle = 63.4$
		$\sigma_S = 5.9$	$\sigma_S = 6.5$	$\sigma_S = 7.9$
C	Lognormal	$\langle C \rangle = 32.6$	$\langle C \rangle = 19.7$	$\langle C \rangle = 11.1$
		$\sigma_C = 3.7$	$\sigma_C = 5.2$	$\sigma_C = 4.8$

5.3 Results and discussion

Here, results of GSA for the single path transmission mechanism based on a second-order PCE are shown, which provides an accurate approximation of the model response surface (not shown) and requires only 10 full model runs to be calibrated.

GSA results are presented in Figures 5.2 - 5.4 for clay-loam, loam and sandy-loam, respectively. These Figures depict $\langle L_p \rangle$ vs f, in the range $0.3 - 1$ GHz, for constant values of m_v between 0.05 and 0.5. Within the area delimited by the curves correspondent to $m_v = 0.05$ and $m_v = 0.5$, variation of sensitivity indices is explored. For the sake of brevity, for each selected soil type, the case of two devices at a distance $d = 3$ m is presented. This is a reasonable configuration for practical applications. Nevertheless, GSA in case of $d = 1 \div 6$ m is also performed (not shown) and it is possible to observe that the Sobol indices are not significantly affected by this parameter.

In case of clay-loam, the principal sensitivity indices associated with

n, S and C are depicted in Figure 5.2. It is shown that, generally, the indices exhibit a negligible variation with f, while it is relevant to analyze their behavior with respect to m_v. Influence of n, as denoted by S_n values, is always above 0.6 and increases with m_v till about 0.85 when the water content tends to 0.5. Regarding to at the principal sensitivity index associated with S, an opposite behavior, respect to m_v variations, is detected. Specifically, the sand content is relevant ($S_S > 0.1$) in case of low values of m_v, (< 0.15), with a maximum of about 0.25 for $m_v = 0.05$. The principal sensitivity index of C exhibits a very low variation with m_v within the range $0.14 - 0.17$. Maximum values for S_C are reached in a middle range of water content values between $0.1 - 0.3$.

In case of loam, the principal sensitivity indices associated with n, S and C are depicted in Figure 5.3. Also in this case the indices exhibit a low variation with f. Regarding to S_n, it varies within the range $0.3 - 0.4$, and is maximum for high values of both m_v and f. When looking at S_S, it is possible to observe that the sand content is relevant ($S_S > 0.1$) in case of low values of m_v, (< 0.1), with a maximum of about 0.2 for $m_v = 0.05$. The principal sensitivity index of C exhibits a low variation with m_v within the range $0.44 - 0.53$. Maximum values for S_C are reached in a middle range of water content values between $0.1 - 0.3$.

In case of sandy-loam, the principal sensitivity indices associated with n, S and C are depicted in Figure 5.4. Regarding to S_n, its value is almost constant with respect to f and increases weakly with m_v within the range $0.1 - 0.15$. When looking at S_S, it is possible to observe a moderate decrease when f increases and that the sand content

is relevant ($S_S > 0.1$) in case of high values of m_v, (> 0.25), with a maximum of about 0.3 when m_v tends to 0.5. The principal sensitivity index of C increases with f and exhibits a moderate variation with m_v within the range $0.5 - 0.68$. Maximum values for S_C are reached in the range of water content values $0.1 - 0.3$. Table 5.2 focuses on GSA results for two experimental settings in which the two devices, at a distance $d = 3$ m, work with an operating frequency of either $f = 0.868$ GHz (LoRa) or $f = 0.433$ GHz (ISM band), and are able to detect path losses $L_p \leq 151$ dB. Under these conditions, the range of measurable path loss increases with the grain size of the soil, as already shown in Figures 5.2-5.4. As a consequence, for $f = 0.868$ GHz, in case of clay-loam it is possible to have only an estimate of m_v if ≤ 0.19; while for loam and sandy-loam, it is possible to estimate m_v if ≤ 0.30 and ≤ 0.50, respectively. For the selected frequency and within the detectable range of L_p values, we observe that for the clay-loam the variability of n is responsible for the $58 - 79\%$ of the uncertainty related to the estimate; hence, this parameter has to be estimated with high accuracy in order to reduce the predictive uncertainty. While influence of C is almost constant and responsible in average for only the 15% of the predictive uncertainty, influence of S varies significantly and only for the minimum detectable values of L_p it is quite significant contributing for a maximum of 26% to the predictive uncertainty. For a loamy soil, n and C are both important with an average contribution of about 35% and 49%, respectively. Again, the influence of S is associated with the highest variability with a maximum contribution of 18% for the minimum detectable L_p. Finally, in case of sandy-loam, the most important parameter is C which is responsible
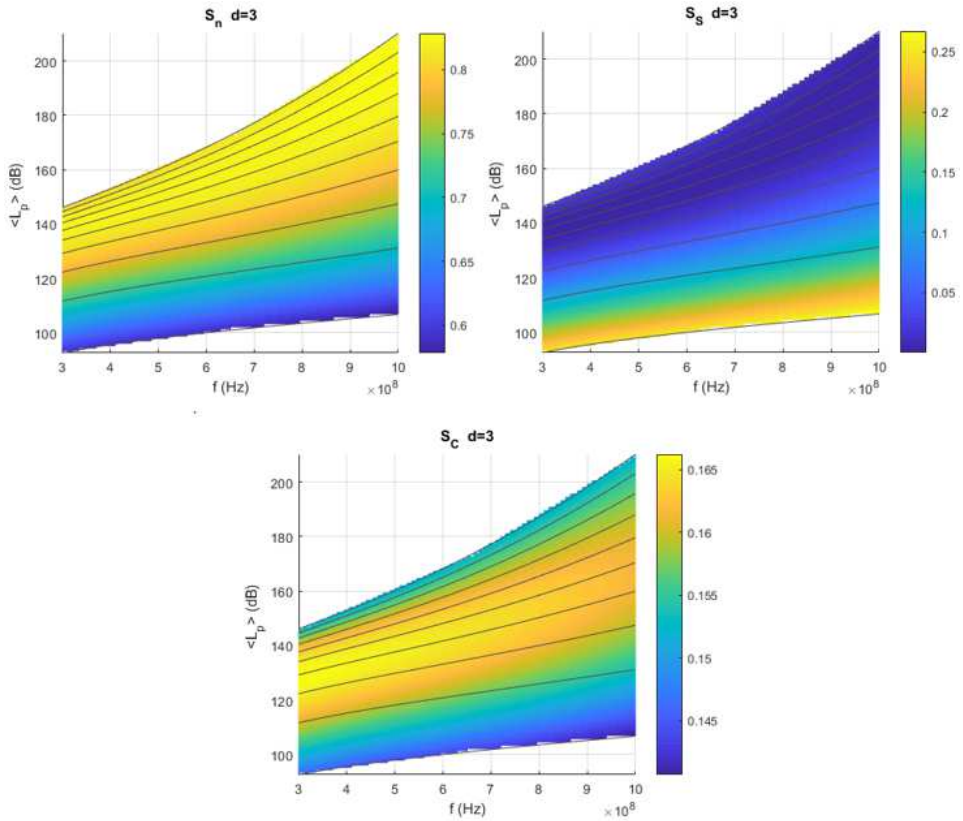
Figure 5.2: Single path model: variations of S_n, S_S, S_C in case of clay-loam in the $(\langle L_p \rangle, f)$ plane. Grey lines denote constant values for m_v between 0.05 (the lowest) and 0.5 (the highest), with a constant step of 0.05.
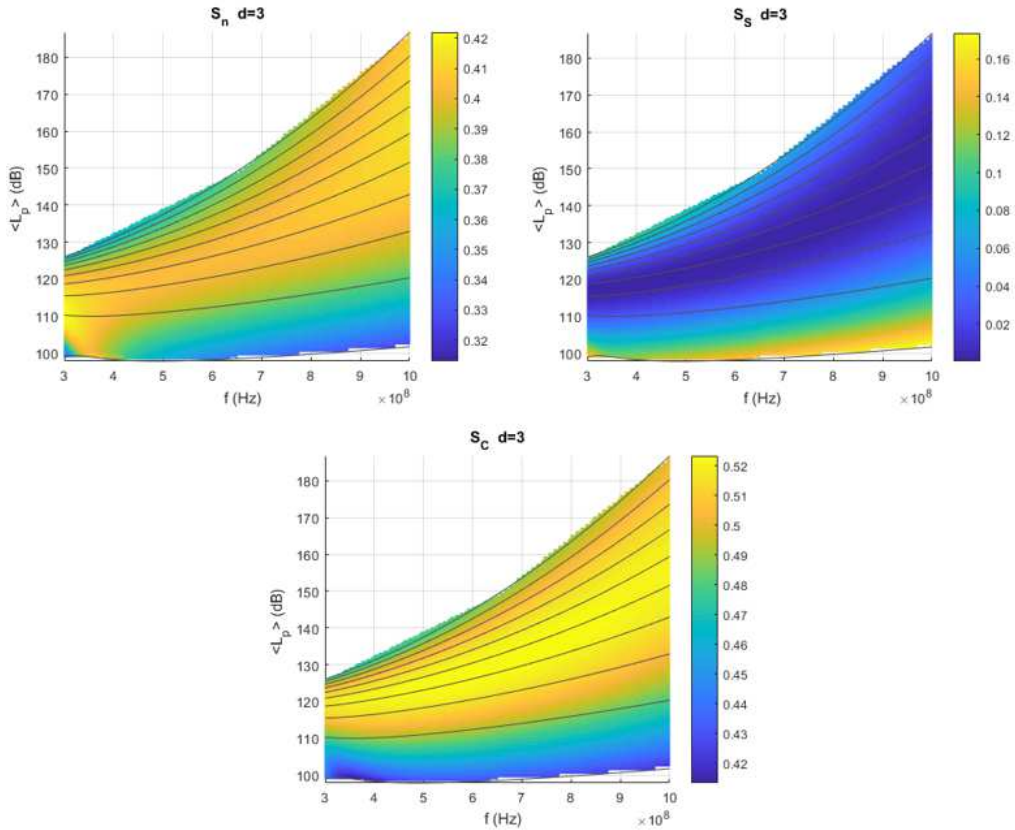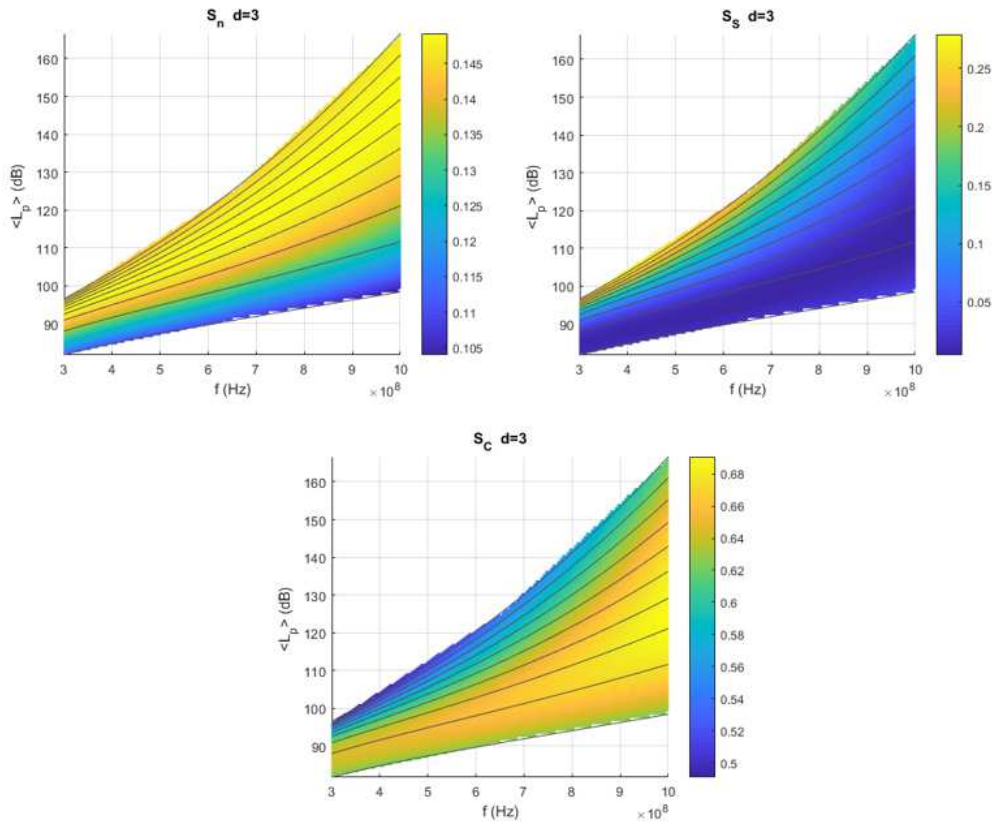
Figure 5.3: Single path model: variations of S_n, S_S, S_C in case of loam in the $(\langle L_p \rangle, f)$ plane. Grey lines denote constant values for m_v between 0.05 (the lowest) and 0.5 (the highest), with a constant step of 0.05.

Figure 5.4: Single path model: variations of S_n, S_S, S_C in case of sandy-loam in the $(\langle L_p \rangle, f)$ plane. Grey lines denote constant values for m_v between 0.05 (the lowest) and 0.5 (the highest), with a constant step of 0.05.

in average for the 60% of the predictive uncertainty; influence of n is low (about 13%) and almost constant, while the contribution of S shows again a variability and in this case it has a maximum of 18% for the maximum measurable value of L_p.

When considering $f = 0.433$ GHz, in case of clay-loam it is possible to have an estimate of m_v if ≤ 0.40; while for loam and sandy-loam, it is possible to estimate m_v if ≤ 0.50. It is shown that the results do not exhibit significant differences with respect to the other operating frequency. This is in line with the general observation that sensitivity indices vary more with m_v than with f. The main difference exists in the range of values of m_v that can be estimated; this range is wider since L_p decreases with f. The sensitivity metrics discussed above, show how the predictive uncertainty can be apportioned to the different sources of uncertainty in the model input. In order to quantify the predictive uncertainty for the three selected soil types, Figure 5.5 represents the map of variance associated with L_p in the selected (m_v, f) domain and for $d = 3$m (it is not shown but the variance always increases with d). As expected, $\sigma^2_{L_p}$ increases with f. In case of clay-loam and loam, $\sigma^2_{L_p}$ also increases with m_v; the opposite is detected for sandy-loam. It is also possible to note that the variance decreases when the grain size increases.

In field scale applications, when L_p is available from device's reading, it is possible to use Figures 5.2 - 5.4 to determine m_v and identify which texture parameters have to be more accurately estimated to reduce the predictive uncertainty. In this sense, results of GSA can be read with respect to soil moisture, given the correspondence between m_v and L_p when texture and operating parameters are fixed. Note

Table 5.2: Single path model: GSA outcomes for two possible experimental settings with $d = 3$m and $f = 0.868$ GHz or $f = 0.433$ GHz.

| f	Soil type	$\langle L_p \rangle$ (dB)	m_v range	influential parameters
0.868 GHz	CL	$105 \div 151$	$0.05 \div 0.19$	$S_n = 0.58 \div 0.79$
				$S_S = 0.26 \div 0.03$
				$S_C = 0.14 \div 0.16$
0.868 GHz	L	$98 \div 151$	$0.05 \div 0.30$	$S_n = 0.30 \div 0.40$
				$S_S = 0.18 \div 0.00$
				$S_C = 0.44 \div 0.53$
0.868 GHz	SL	$96 \div 150$	$0.05 \div 0.50$	$S_n = 0.11 \div 0.15$
				$S_S = 0.03 \div 0.18$
				$S_C = 0.63 \div 0.58$
0.433 GHz	CL	$97 \div 151$	$0.05 \div 0.40$	$S_n = 0.59 \div 0.82$
				$S_S = 0.25 \div 0.01$
				$S_C = 0.15 \div 0.16$
0.433 GHz	L	$90 \div 133$	$0.05 \div 0.50$	$S_n = 0.31 \div 0.36$
				$S_S = 0.16 \div 0.09$
				$S_C = 0.45 \div 0.48$
0.433 GHz	SL	$86 \div 106$	$0.05 \div 0.50$	$S_n = 0.11 \div 0.14$
				$S_S = 0.01 \div 0.27$
				$S_C = 0.62 \div 0.50$
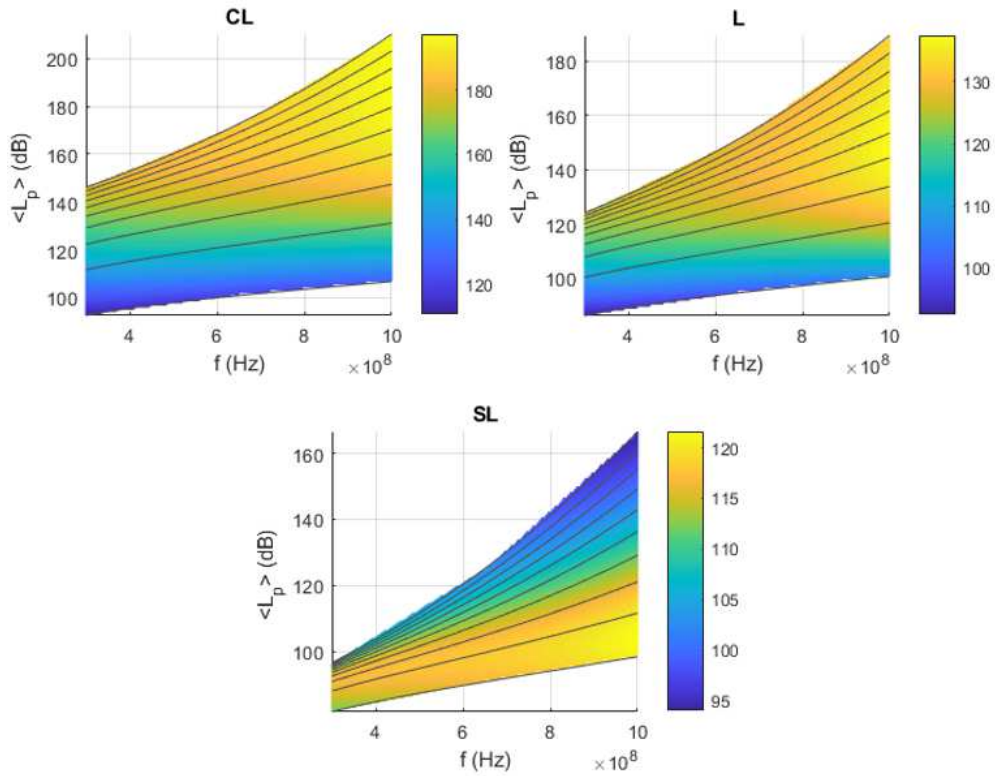
Figure 5.5: Single path model: maps of variance in case of clay-loam (CL), loam (L) and sandy-loam (SL) in the $(\langle L_p \rangle, f)$ plane. Grey lines denote constant values for m_v between 0.05 (the lowest) and 0.5 (the highest), with a constant step of 0.05.

that results of GSA with respect to L_p, i.e. the device's reading, may represent a basis for the application of other techniques, such as data assimilation, sensitivity-based model calibration, or model selection (Ciriello et al., 2013a; Ciriello et al., 2015), in order to reduce the epistemic uncertainty and increase the reliability of m_v estimations at the same time.

In case of a two-path transmission mechanism, results of GSA are very similar as shown in A.

5.4   Final remarks

In this work the predictive uncertainty associated with the path loss when adopting WUCNs to estimate soil moisture is treated. In particular, the focus is on uncertainty deriving from textural parameters which significantly influence the path loss of the signal transmitted to the receiver as expressed in the selected underlying mathematical framework. To this end, GSA is performed and texture uncertainty based on the PCE technique is propagated to reduce the computational cost associated with the analysis. Sensitivity and variance maps are produced in order to fully characterize the predictive uncertainty as a guide for practical applications and selected methods are applied to: (i) different transmission mechanisms (either single path or two-path models), (ii) different device distances ($1 \div 6$m), and (iii) three soil types (clay-loam, loam, and sandy-loam).

The study reveals that $\langle L_p \rangle$ varies significantly with the operating parameters, f and d, for given soil texture and moisture, and the same is true for the predictive uncertainty (i.e. $\sigma^2_{L_p}$). At the same time, the

operating conditions have a negligible impact on the selected sensitivity indices. This means that the most influential texture parameters, which may deserve additional data collection, vary only with soil type and moisture. This is relevant in field scale applications, where d and f are typically controlled by spatial and/or technological constraints. It is also found that the transmission mechanism (see Appendix A) does not impact significantly on GSA results and on the predictive uncertainty.

GSA reveals that if in case of clay-loam, variability on the porosity explains most of the predictive uncertainty, in case of sandy-loam the clay content is the parameter which requires the most accurate estimate. When considering a loamy soil, these two parameters are almost equally important. Influence of sand content is significantly variable for the three soil types: it increases with m_v in case of sandy-loam, while the opposite happens when considering the other two soils. In general, sensitivity indices exhibit significant variations with m_v.

The findings of this analysis can be easily extended to other soil types. At the same time, in a future analysis, it is possible to extend this approach in order to consider alternative models, respect to the one suggested by (Peplinski, Ulaby, and Dobson, 1995), and evaluate their predictive capacity against measurements, following the method suggested in (Ciriello et al., 2013a; Ciriello et al., 2015).

Chapter 6

Development of conceptual models for non-Newtonian porous gravity currents

Sommario

La valutazione dello stato e del rischio associato a un corpo idrico sotterraneo va affrontato, come spiegato precedentemente, scomponendo il problema in eventi base all'interno di un inquadramento metodologico di tipo probabilistico. Il calcolo della probabilità degli eventi base richiede la predisposizione di opportuni modelli concettuali capaci di descrivere i processi chiave legati al flusso ed al trasporto in ambiente sotterraneo.

In questo contesto, il presente Capitolo è dedicato allo sviluppo di formulazioni analitiche utili ad interpretare fenomeni di migrazione

di fluidi non-ewtoniani nel sottosuolo. Generalmente tali fenomeni si possono verificare (i) in applicazioni di ingegneria industriale, durante i processi di stoccaggio di gas dal sottosuolo o nell'intorno di pozzi di perforazione, o (ii) in contesti geologici complessi, ove si individuano fratture nei mezzi porosi naturali. In queste circostanze, la trattazione degli scenari di migrazione non può avvenire attraverso l'impiego delle equazioni di Navier-Stokes, perché la reologia associata ai fluidi è più complessa del modello di viscosità newtoniano.

Nello specifico, il lavoro mostrato nel seguito riguarda lo studio della propagazione delle correnti di gravità nei mezzi porosi ed ha prodotto la seguente pubblicazione: **"Porous gravity currents: axisymmetric propagation in horizontally graded medium and a review of similarity solutions", Advances in Water Resources, Vol. 115 pp 136–150, (Lauriola I., Felisa G., Petrolo D., Di Federico V., Longo S., 2018)**.

In questo studio, sono stati analizzati gli effetti che la reologia del fluido e la variazione di permeabilità possono avere sulla propagazione del fenomeno. Con questo fine sono stati sviluppati modelli semi-analitici che descrivono l'iniezione istantanea o continua di un fluido non-newtoniano all'interno del mezzo poroso; successivamente è stata verificata la validità della modellazione attraverso un set di analisi sperimentali eseguite in laboratorio. I modelli derivati risultano sufficientemente dettagliati al fine di cogliere la peculiarità del processo, ma conservano una forma semplice, avendo una natura semi-analitica. Quest'ultimo aspetto rende la modellazione versatile per ulteriori applicazioni perché consente, in modo sufficientemente agevole, lo sviluppo di analisi stocastiche come l'analisi di sensitività e di rischio,

discusse nei Capitoli precedenti. Questo tipo di analisi, infatti, possono rappresentare un valido supporto per individuare con maggiore dettaglio quelli che sono i fattori chiave che governano questo tipo di processi.

6.1 Introduction

The propagation of gravity-driven flows in porous media is but a chapter of the fascinating 'book' on gravity currents (hereinafter GCs), which has received considerable attention (Ungarish, 2009), with new 'chapters' being continuously added. Yet also porous GCs by themselves, originating from such diverse phenomena (carbon dioxide sequestration, mining engineering, environmental pollution and remediation, seawater intrusion, to name but a few) constitute such a wide topic that a comprehensive summary is arduous. In the authors' view, the recent advancements on gravity-driven porous flow belong to two broad categories.

The first group of contributions has as a common feature the modeling of the spatial variations of properties and/or of boundary conditions in natural (geologic) media, and the description of their topographical features. Examples of such contributions are Huppert, Neufeld, and Strandkvist, 2013, Sahu and Flynn, 2017, and (Ngo, Mouche, and Audigane, 2016), where heterogeneity is modeled via discrete layers or intrusions of finite extent; (Islam et al., 2016), which introduces explicitly small-scale heterogeneity; Yu, Zheng, and Stone, 2017, where simultaneous drainage from a permeable substrate and an edge is accounted for; and (Huber, Stroock, and Koch, 2016), which aims at

reproducing the effect of diverse CO_2 injection strategies.

The second broad group of GC-themed contributions presents an improved description of fundamental mechanisms via a more sophisticated modeling. Some relevant examples are the effects of a change in flux (Ball et al., 2017) or of stratification in an intruding current (Pegler, Huppert, and Neufeld, 2016); the investigation of the CO_2 sequestration mechanisms into deep saline aquifers, involving two-phase flow (Guo et al., 2016) or with possible background hydrological flow (Unwin, Wells, and Woods, 2016); the interactions between gravity currents and convective dissolution (Elenius, Voskov, and Tchelepi, 2015) or geomechanics (Bjornara, Nordbotten, and Park, 2016); the adoption of realistic rheological models in the study of non-Newtonian GCs (Di Federico et al., 2017).

Some recent contributions belong to both categories, and are associated for example with the modeling of CO_2 sequestration (Ngo, Mouche, and Audigane, 2016) or the simultaneous presence of non-Newtonian flow and spatial heterogeneity or specific topographical features. The latter topic has been investigated in depth by our group, considering deterministic heterogeneity and radial Di Federico et al., 2014 or plane geometry Ciriello et al., 2016, and channelized flow Di Federico et al., 2014. The motivation for these studies lies in a multiplicity of applications involving complex fluids flowing in geologic media characterized by spatial heterogeneity at various scales: oil and displacing suspensions in reservoir flow, remediation carriers and liquid contaminants in the subsurface environments, drilling and grouting fluids; earlier references (Di Federico et al., 2014; Ciriello et al., 2016) list specific references to these applications.

Flow of non-Newtonian GCs relies on a body of knowledge accumulated for Newtonian currents: the reference works of Huppert & Woods Huppert and Woods, 1995 for plane geometry and by Lyle *et al.* Lyle et al., 2005 for axisymmetric geometry were extended to power-law fluid flow by Di Federico *et al.* Di Federico, Archetti, and Longo, 2012a; Di Federico, Archetti, and Longo, 2012b, which, in turn, set the stage for the more realistic setups cited earlier. Variations of properties along vertical and horizontal direction were considered in the context of Newtonian GCs by Zheng et al., 2013 and Zheng, Christov, and Stone, 2014, respectively. While vertical variations mimic the effect of stratification, horizontal variations may represent e.g. the effect induced by the drilling of a well, and thus are of interest especially in the context of axisymmetric propagation. A review of existing studies on non-Newtonian porous GCs reveals the lack of a study coupling power-law rheology and permeability gradients along the flow direction in axisymmetric flow. Such a study is presented here considering the usual hypothesis of a GC of time-variable inflow.

6.2 Problem formulation

Consider a non-Newtonian power-law fluid of density ρ, consistency index m, and flow behavior index n, that spreads axisymmetrically over a horizontal bed into a porous medium of height h_0, initially saturated with a lighter fluid of density $\rho - \Delta\rho$ (see Figure 6.1). Under the sharp interface and thin current approximations, and in the absence of capillary effects (see the recent paper by Chiapponi Chiapponi, 2017 for an indication of the fluid retention in a glass beads

porous medium), the pressure within the current is hydrostatic, and given by $p(r, z, t) = p_1 + \Delta\rho\, gh(r, t) - \rho gz$, where r and z represent radial and vertical coordinates, $p_1 = p_0 + (\rho - \Delta\rho)gh_0$ is a constant, p_0 is the constant pressure at $z = h_0$, and g is gravity. Further, the velocity in the ambient fluid and the vertical velocity in the intruding fluid can be neglected, allowing to describe the current behaviour by means of its horizontal velocity $u(r, t)$, thickness $h(r, t)$ and maximum extension $r_N(t)$ for given time t. The expression of the horizontal velocity can be deduced from the following general equation, valid for the motion of a power-law fluid in a porous medium (Cristopher and Middleman, 1965)

$$\nabla p - \rho \boldsymbol{g} = -\frac{\mu_{eff}}{k}|\boldsymbol{u}|^{n-1}\boldsymbol{u}, \qquad (6.1)$$

in which p is the pressure, $\boldsymbol{u}$ is the Darcy velocity field, $\boldsymbol{g}$ is the gravity vector, k the permeability, and μ_{eff} is the effective viscosity (dimensions $[\mathrm{ML}^{-n}\mathrm{T}^{n-2}]$). The mobility $\frac{\mu_{eff}}{k}$ is given by (Di Federico, Archetti, and Longo, 2012b)

$$\frac{k}{\mu_{eff}} = \frac{1}{2C_t}\frac{1}{m}\left(\frac{n\phi}{3n+1}\right)^n\left(\frac{50k}{3\phi}\right)^{(n+1)/2}, \qquad (6.2)$$

where ϕ is the porosity, and $C_t = C_t(n)$ the tortuosity factor, for which different formulations are available (Shenoy, 1995). In the following, Pascal's formulation Pascal, 1983, $C_t = (25/12)^{(n+1)/2}$, is adopted.

Local mass conservation implies that

$$\frac{1}{r}\frac{\partial}{\partial r}(ruh) = -\phi\frac{\partial h}{\partial t}, \qquad (6.3)$$

and, in addition, two boundary conditions are needed to formulate the

problem. The first b.c. is the global mass conservation condition

$$2\pi\phi \int_0^{r_N(t)} rh(r,t)\mathrm{d}r = Qt^\alpha, \tag{6.4}$$

expressing the total volume of the current as a function of time t and parameters Q (dimensions $[\mathrm{L}^3\mathrm{T}^{-\alpha}]$) and α. This formulation includes the instantaneous injection with constant volume ($\alpha = 0$), and the continuous injection with increasing volume ($\alpha > 0$).

The second boundary condition states that the thickness at the current front is null, i.e.

$$h\left(r_N(t), t\right) = 0. \tag{6.5}$$

Further, the horizontal permeability variation needs to be described. The following law of variation is adopted for the medium permeability k (Ciriello, Longo, and Di Federico, 2013; Zheng, Christov, and Stone, 2014)

$$k(z) = k_0 \left(\frac{r}{\sigma r^*}\right)^\beta, \tag{6.6}$$

where k_0 is a characteristic permeability, r^* is a length scale, σ is a coefficient introduced for convenience, and β is a constant. For $\beta \lessgtr 0$, the permeability decreases or increases with the distance from the injection well, respectively; $\beta = 0$ represents a medium with constant permeability k_0, and the simpler model of Di Federico *et al.* (Di Federico, Archetti, and Longo, 2012b) is recovered. We require that $\beta < \beta_0 = 2(n+3)/(n+1)$; the upper limitation to the increase of the permeability with distance from the origin guarantees the validity of our solution. For a Newtonian fluid ($n = 1$), $\beta_0 = 4$ (Ciriello *et al.* Ciriello, Longo, and Di Federico, 2013 found $\beta_0 = 3$ in plane geometry); for the two limit cases $n \ll 1$ and $n \gg 1$ (very shear-thinning

or shear-thickening fluids), $\beta_0 \sim 6$ and $\beta_0 \sim 2$ respectively. Realistic values of exponents in power-law variations of properties (De Marsily, 1980; Jiang, Wang, and Wan, 2010) tend to be much lower than the upper limit value β_0. Note that the case of permeability decreasing with distance from the injection well roughly represents motion within a natural medium, whose permeability was altered nearby the injection well by the drilling process (see, e.g., Slider Slider, 1983) For $\beta < 0$, the behaviour of (6.6) is singular for $r \to 0$, but this does not affect the overall behaviour of the current.

Substituting Eq. (6.6) in the one-dimensional version of Eq. (6.1), and expressing the pressure gradient as a function of the unknown free surface as $\partial p/\partial r = \Delta \rho \, g(\partial h/\partial r)$ yields the following equation of motion

$$u(r,z,t) = -\left(\Lambda \Delta \rho \, g\right)^{1/n} k_0^{(n+1)/(2n)} \left(\frac{r}{\sigma r^*}\right)^{\frac{\beta(n+1)}{2n}} \left|\frac{\partial h}{\partial r}\right|^{1/n-1} \frac{\partial h}{\partial r}, \quad (6.7)$$

where

$$\Lambda = \Lambda(\phi, m, n) = \frac{1}{2C_t} \left(\frac{50}{3}\right)^{(n+1)/2} \left(\frac{n}{3n+1}\right)^n \frac{\phi^{(n-1)/2}}{m}, \quad (6.8)$$

which for a Newtonian fluid ($n = 1$) is the inverse of dynamic viscosity μ . The mathematical problem constituted by Equations (6.7) and (6.3) with boundary conditions (6.4) and (6.5) may be rendered non-dimensional upon defining time, space, and velocity scales as

$$t^* = \left(\frac{Q}{\phi v^{*3}}\right)^{1/(3-\alpha)}, \; r^* = v^* t^*, \; v^* = \frac{\left(\Lambda \Delta \rho \, g\right)^{1/n} k_0^{(1+n)/(2n)}}{\phi \sigma^{\beta(n+1)/(2n)}}. \quad (6.9)$$
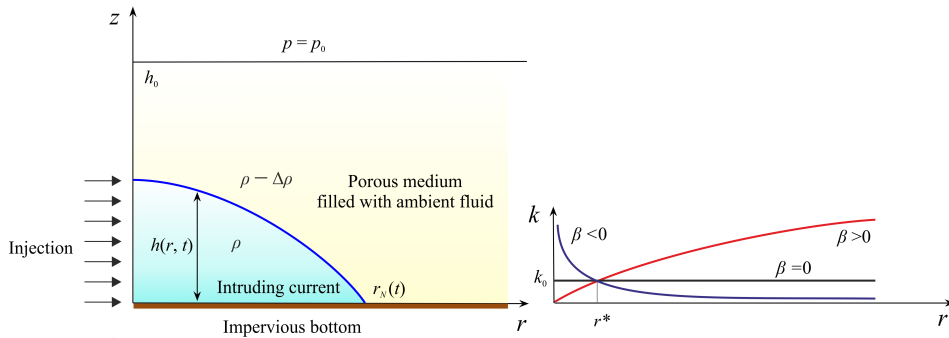
Figure 6.1: Sketch of an axisymmetric gravity current intruding into a saturated porous medium of thickness h_0. The panel on the right illustrates radially increasing ($\beta > 0$), decreasing ($\beta < 0$), and homogeneous ($\beta = 0$) permeabilities.

and dimensionless coordinates as $T = t/t^*$, $R = r/r^*$, $R_N = r_N/r^*$, and $H = h/r^*$.

Note that the time scale t^* is defined for $\alpha \neq 3$. The particular case $\alpha = 3$ requires a partially different non-dimensional formulation, which can be easily derived following e.g. Vella and Huppert, 2006; Di Federico, Archetti, and Longo, 2012a. For all other cases, the dimensionless problem reads

$$\frac{1}{R}\frac{\partial}{\partial R}\left[R^{F_1+1}H\left|\frac{\partial H}{\partial R}\right|^{1/n-1}\frac{\partial H}{\partial R}\right] = \frac{\partial H}{\partial T}, \tag{6.10}$$

obtained by combining the dimensionless versions of (6.7) and (6.3). In Eq. (6.10)

$$F_1 = \frac{\beta(n+1)}{2n} \tag{6.11}$$

is a factor which reduces to zero in the homogeneous case.

The global mass balance (6.4) becomes

$$2\pi \int_0^{R_N} RH\mathrm{d}R = T^\alpha, \qquad (6.12)$$

while the condition at the front (6.5) does not vary in dimensionless form.

6.3 Solution

It is desirable to obtain a self-similar solution to the system formed by Equations (6.10) and (6.12) with (6.5) to capture the long-term evolution of the current once the influence of initial and boundary conditions fades. As illustrated in the Appendix B, a first-kind similarity solution for the extension and thickness of the current is derived in the form $R_N(T) = \eta_N T^{F_2}$ and $H(R,T) = \eta_N^{F_5} T^{F_3} \psi(\zeta)$, where the thickness factor $\psi(\zeta)$ is the solution of the ODE

$$\left(\zeta^{F_1+1} \psi\psi' \, |\psi'|^{1/n-1}\right)' + F_2\zeta^2\psi' - F_3\zeta\psi = 0, \qquad (6.13)$$

in which the prime indicates d /dζ, and subject to the condition

$$\psi(1) = 0, \qquad (6.14)$$

while the similarity variable at the front of the current η_N is given by

$$\eta_N = \left(2\pi \int_0^1 \zeta\psi(\zeta)\mathrm{d}\zeta\right)^{-1/(F_5+2)}, \qquad (6.15)$$

and the factors F_2, F_3 and F_5 are given respectively by (B.2), (B.3), and (B.7). For a homogeneous medium ($\beta = 0$), results reduce to the

simpler case of Di Federico *et al.* (Di Federico, Archetti, and Longo, 2012b), with $F_1 = 0$, $F_2 = (\alpha+n)/(n+3)$, $F_3 = [\alpha(n+1)-2n]/(n+3)$, and $F_5 = n + 1$. For a Newtonian fluid ($n = 1$), one obtains $F_1 = \beta$, $F_2 = (\alpha + 1)/(4 - \beta)$, $F_3 = [\alpha(2 - \beta) - 2]/(4 - \beta)$, and $F_5 = 2 - \beta$. When both simplifications apply, the homogeneous Newtonian case studied by Lyle *et al.* Lyle et al., 2005 is recovered, and $F_1 = 0$, $F_2 = (\alpha + 1)/4$, $F_3 = (\alpha - 1)/2$, and $F_5 = 2$.

For the instantaneous injection case ($\alpha = 0$), Equations (6.13) and (6.15) subject to (6.14) and $\psi'(0) = 0$ (the latter condition derives from a no-flux boundary condition for $r = 0$ valid for constant volume) are amenable to the closed-form solution

$$\psi(\zeta) = \frac{F_{20}^n}{F_5} \left(1 - \zeta^{F_5}\right), \tag{6.16}$$

$$\eta_N = \left(\frac{\pi F_{20}^n}{F_5 + 2}\right)^{-\frac{1}{F_5+2}}, \tag{6.17}$$

where $F_{20} = F_2(\alpha = 0) = 2n/[2(n + 3) - \beta(n + 1)]$. The constraint $F_5 > 0$ (equivalent to $\beta < 2$) applies. When $\beta = 1$, Eq. (17) of Di Federico *et al.* Di Federico, Archetti, and Longo, 2012b is recovered. When $n = 1$, (6.16) and (6.17) transform into

$$\psi(\zeta) = \frac{1}{(4 - \beta)(2 - \beta)} \left(1 - \zeta^{2-\beta}\right), \tag{6.18}$$

$$\eta_N = \left[\frac{(4 - \beta)^2}{\pi}\right]^{1/(4-\beta)}. \tag{6.19}$$

Finally when $n = 1$ and $\beta = 0$, $\psi(\zeta) = (1 - \zeta^2)/8$ and $\eta_N = 2/\pi^{1/4}$ (Pattle, 1959).

For the continuous injection case ($\alpha \neq 0$) equation (6.13) needs to be integrated numerically with (6.14) and a second boundary condition is obtained expanding the solution in power Frobenius series and balancing the lower order terms for $\zeta \to 1$. This yields

$$\psi'|_{\zeta \to 1} = -a_0 b \epsilon^{b-1}, \ a_0 = F_2^n, \ b = 1, \tag{6.20}$$

where $\epsilon = 1 - \zeta$ is a small quantity and F_2 is non-negative if $\beta < 2(n + 3)/(n + 1)$. Integrating (6.13) with (6.14) and (6.20) with a Runge-Kutta scheme yields the thickness profile $\psi(\zeta)$ and the similarity variable η_N. Sample results are shown in Figures 6.2(a)-(f) for $\alpha = 0, 1$, and selected values of n and β. The analytical solution for $\alpha = 0$ and the results obtained by Lyle *et al.* Lyle et al., 2005 for the Newtonian, homogeneous case are well reproduced. The thickness profile $\psi(\zeta)$ increases with the injected volume (α) for given fluid and medium (n and β), is an increasing function of β, and a decreasing function of n for constant volume currents; the dependency on n for constant flux currents is more complex. The prefactor η_N (6.15), whose value influences the current thickness via (B.8), is illustrated in Figure 6.2(g) versus α for different n, β. η_N increases with n and decreases with α and β, while its sensitivity is largest for smaller α and n and larger β. These dependencies are reversed with respect to the thickness profile, so that the dimensionless thickness results from the interplay of ψ and η_N.

Other quantities of interest are the aspect ratio of the current (the ratio between its average thickness $\overline{H}$ and radius R_N) and the average free-surface gradient driving the motion $\left(\overline{\frac{\partial H}{\partial R}}\right)$. These are given
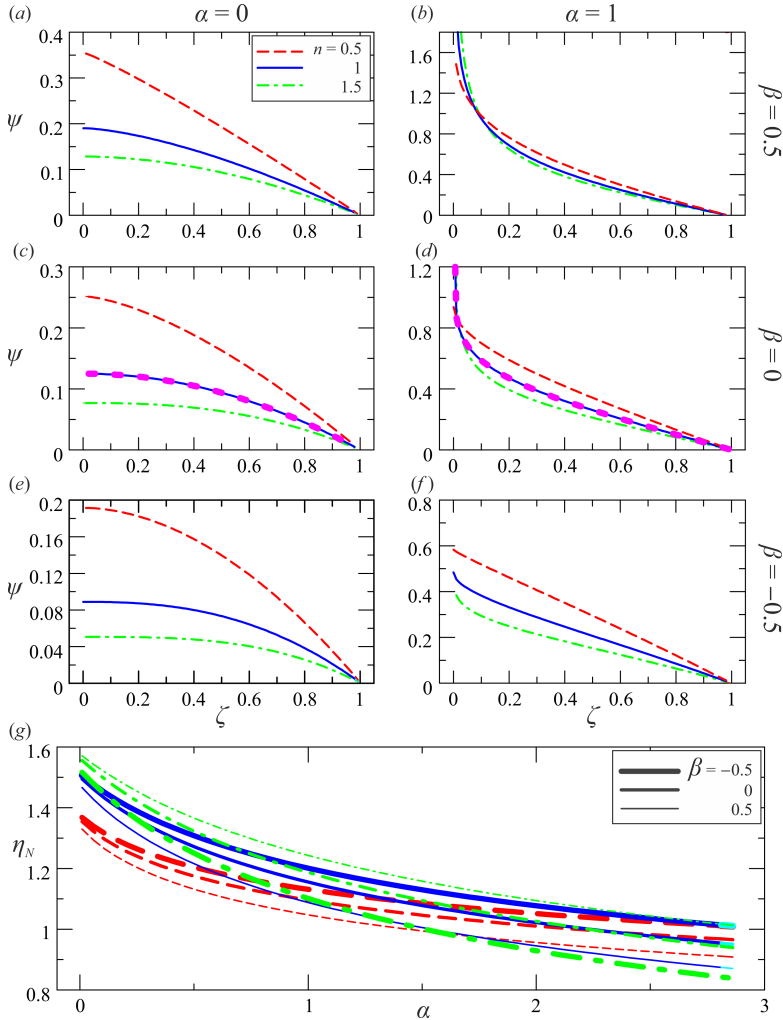
Figure 6.2: (a)-(f) Thickness profile $\psi(\zeta)$. Upper/intermediate/lower rows: radially increasing $(\beta = 0.5)$/uniform $(\beta = 0)$/decreasing $(\beta = -0.5)$ permeability; left/right columns: constant volume $(\alpha = 0)$/constant flux $(\alpha = 1)$; dashed red/solid light blue/dot-dashed green lines: shear-thinning $(n = 0.5)$/Newtonian $(n = 1)$/shear-thickening $(n = 1.5)$ fluids. Pink ovals in panels (c)-(d) are the results by Lyle *et al.* Lyle et al., 2005 for $\beta = 0, n = 1$ and $\alpha = 0, 1$, respectively;(g) prefactor $\eta_N(\alpha)$. Dashed/solid/dash-dotted lines: $n = 0.5/1/1.5$; thick/intermediate/thin lines: $\beta = 0.5/0/0.5$.

respectively by

$$\frac{\overline{H}}{R_N} = \eta_N^{F_5-1}T^{F_3-F_2}\overline{\psi}, \tag{6.21}$$

$$\overline{\left(\frac{\partial H}{\partial R}\right)} = \eta_N^{F_5-1}T^{F_3-F_2}\overline{\left(\frac{d\psi}{d\zeta}\right)}; F_3 - F_2 = \frac{\alpha[2n - \beta(n+1)] - 6n}{2(n+3) - \beta(n+1)}, \tag{6.22}$$

where $\overline{\psi}$ and $\overline{\left(\frac{d\psi}{d\zeta}\right)}$ are respectively the average value of the thickness profile and of its derivative over the interval 0-1.

Furthermore, the velocity field u is given in dimensionless form $U = u/v^*$ by

$$U = -\phi R^{F_1}\eta_N^{\frac{F_5-1}{n}}T^{\frac{F_3-F_2}{n}}\left|\frac{\partial\psi}{\partial\zeta}\right|^{1/n-1}\frac{\partial\psi}{\partial\zeta}, \tag{6.23}$$

while for the velocity of advancement of the current $v = \mathrm{d}\,r_N(t)/\mathrm{d}\,t$, the dimensionless expression $V = v/v^*$ is

$$V = \eta_N F_2 T^{F_2-1}; F_2 - 1 = \frac{2\alpha - [6 - \beta(n+1)]}{(n+1)(2-\beta) + 4}. \tag{6.24}$$

6.4   Discussion of results

6.4.1   Behaviour of key time exponents

The power-law time exponents F_2, F_2-1, F_3 and F_3-F_2 (equations (B.2), (6.24), (B.3), and (6.22)), of the radius, velocity, thickness and aspect ratio of the gravity current are the key factors to understand the evolution of the current over time. In the present section, we explore their dependency on model parameters α (the time rate of change of the fluid volume), n (the flow behaviour index), and β (the

rate of change of the permeability along the direction of propagation) by evaluating their sign and their partial derivatives with respect to model parameters. The results obtained for F_2 (together with $F_2 - 1$), F_3, and $F_3 - F_2$ are listed in Tables 6.1, 6.2, and 6.3, respectively. Various limit values of α, and, in some instances, of other parameters, emerge; each limit value is listed below the respective condition on F_2, F_3, $F_3 - F_2$ or their partial derivative. These threshold values of model parameters discriminate between a positive, null, or negative value of F_2, F_3, $F_3 - F_2$ and of their partial derivative with respect to α, n, and β.

Inspection of Table 6.1 reveals that for a physically meaningful solution, the permeability must decrease over space, or increase not too sharply ($\beta < \beta_e$); for a Newtonian fluid ($n = 1$), $\beta_e = 4$. The current front accelerates ($F_2 - 1 > 0$) for any α under a sharp increase in permeability ($\beta > \beta_a$), or beyond a threshold value α_a of α for permeability decreasing or increasing moderately over space ($\beta < \beta_a$); otherwise, the current is decelerated. For a Newtonian fluid ($n = 1$), the threshold values reduce to $\beta_a = 3$, $\alpha_a = 3 - \beta$; for a homogeneous medium ($\beta = 0$) and any fluid, $\alpha_a = 3$. Moreover, F_2 increases with α for any combination of β, n, as a larger fluid injection rate implies an increase in the current velocity regardless of the permeability variation and fluid nature. Similarly, F_2 increases with β for any combination of α, n, as an increase/less marked decrease of the permeability favours the current advancement. The functional dependency of F_2 on n is more complex, as the velocity of the current increases with n for any α under a sharp increase in permeability ($\beta > \beta_{en}$), or below a threshold value α_{en} of α for permeability decreasing or increasing moderately

Table 6.1: Dependence of the propagation rate F_2 on model parameters for horizontally varying permeability. Row 1: Conditions for $F_2 > 0$. Row 2: conditions for decelerated/constant speed/accelerated currents. Row 3: condition for F_2 increasing with α. Row 4: conditions for F_2 decreasing/constant/increasing with n. Row 5: conditions for F_2 increasing with β.

$$
\begin{cases}
F_2 > 0 & \beta < \beta_e \\[2ex]
\beta_e & \dfrac{n+3}{n+1} \\[2ex]
F_2 - 1 < 0 & \beta < \beta_a \wedge \alpha < \alpha_a \\[1ex]
F_2 - 1 = 0 & \beta < \beta_a \wedge \alpha = \alpha_a \\[1ex]
F_2 - 1 > 0 & (\beta < \beta_a \wedge \alpha > \alpha_a) \vee (\beta = \beta_a \wedge \alpha > 0) \vee \\[1ex]
& (\beta > \beta_a \wedge \forall \alpha) \\[2ex]
\beta_a & \dfrac{6}{n+1} \\[2ex]
\alpha_a(\beta < \beta_a) & \dfrac{6 - \beta(n+1)}{2} \\[2ex]
\dfrac{\partial F_2}{\partial \alpha} > 0 & \forall n, \beta \\[2ex]
\dfrac{\partial F_2}{\partial n} < 0 & \beta < \beta_{en} \wedge \alpha > \alpha_{en} \\[2ex]
\dfrac{\partial F_2}{\partial n} = 0 & \beta < \beta_{en} \wedge \alpha = \alpha_{en} \\[2ex]
\dfrac{\partial F_2}{\partial n} > 0 & (\beta < \beta_{en} \wedge \alpha < \alpha_{en}) \vee (\beta \geq \beta_{en} \wedge \forall \alpha) \\[2ex]
\beta_{en} & 2 \\[2ex]
\alpha_{en}(\beta < \beta_{en}) & \dfrac{6 - \beta}{2 - \beta} \\[2ex]
\dfrac{\partial F_2}{\partial \beta} > 0 & \forall \alpha, n
\end{cases}
$$

Table 6.2: Dependence of the thickness time exponent F_3 on model parameters for horizontally varying permeability. Row 1: conditions for thickness decreasing/constant/increasing with time. Row 2: condition for F_3 decreasing/constant/increasing with α. Row 3: conditions for F_3 decreasing/constant/increasing with n. Row 4: conditions for F_3 decreasing with β.

$$
\begin{cases}
F_3 < 0 & (\beta < \beta_t \wedge \alpha < \alpha_t) \vee (\beta \geq \beta_t \wedge \forall\alpha) \\[1ex]
F_3 = 0 & \beta < \beta_t \wedge \alpha = \alpha_t \\[1ex]
F_3 > 0 & \beta < \beta_t \wedge \alpha > \alpha_t \\[1ex]
\beta_t & 2 \\[1ex]
\alpha_t(\beta < \beta_t) & \dfrac{4n}{(n+1)(2-\beta)} \\[2ex]
\begin{cases} \dfrac{\partial F_3}{\partial \alpha} \lesseqgtr 0 \end{cases} & \beta \gtreqless \beta_t \\[1ex]
\beta_{t\alpha} & 2 \\[1ex]
\dfrac{\partial F_3}{\partial n} < 0 & (\beta < \beta_{tn} \wedge \alpha < \alpha_{tn}) \vee (\beta \geq \beta_{tn} \wedge \forall\alpha) \\[1ex]
\dfrac{\partial F_3}{\partial n} = 0 & \beta < \beta_{tn} \wedge \alpha = \alpha_{tn} \\[1ex]
\dfrac{\partial F_3}{\partial n} > 0 & \beta < \beta_{tn} \wedge \alpha > \alpha_{tn} \\[1ex]
\beta_{tn} & 2 \\[1ex]
\alpha_{tn}(\beta < \beta_{tn}) & \dfrac{6-\beta}{2-\beta} \\[2ex]
\begin{cases} \dfrac{\partial F_3}{\partial \beta} < 0 \end{cases} & \forall\alpha, n
\end{cases}
$$

Table 6.3: Dependence of the aspect ratio time exponent $F_3 - F_2$ on model parameters for horizontally varying permeability. Row 1: conditions for aspect ratio increasing/constant/decreasing with time. Row 2: condition for $F_3 - F_2$ increasing with α. Row 3: conditions for $F_3 - F_2$ decreasing/constant/increasing with n. Row 4: conditions for $F_3 - F_2$ decreasing/constant/increasing with β.

$$
\begin{cases}
F_3 - F_2 < 0 & (\beta < \beta_g \wedge \alpha < \alpha_g) \vee (\beta \geq \beta_g \wedge \forall \alpha) \\[4pt]
F_3 - F_2 = 0 & \beta < \beta_g \wedge \alpha = \alpha_g \\[4pt]
F_3 - F_2 > 0 & \beta < \beta_g \wedge \alpha > \alpha_g \\[4pt]
\beta_g & \dfrac{2n}{n+1} \\[6pt]
\alpha_g(\beta < \beta_g) & \dfrac{6n}{2n - \beta(n+1)}
\end{cases}
$$

$$
\begin{cases}
\dfrac{\partial(F_3 - F_2)}{\partial \alpha} \lesseqqgtr 0 & \beta \gtreqqless \beta_{g\alpha} \\[8pt]
\beta_{g\alpha} & \dfrac{2n}{n+1}
\end{cases}
$$

$$
\begin{cases}
\dfrac{\partial(F_3 - F_2)}{\partial n} < 0 & (\beta < \beta_{gn} \wedge \alpha < \alpha_{gn}) \vee (\beta \geq \beta_{gn} \wedge \forall \alpha) \\[8pt]
\dfrac{\partial(F_3 - F_2)}{\partial n} = 0 & \beta < \beta_{gn} \wedge \alpha = \alpha_{gn} \\[8pt]
\dfrac{\partial(F_3 - F_2)}{\partial n} > 0 & \beta < \beta_{gn} \wedge \alpha > \alpha_{gn} \\[8pt]
\beta_{gn} & 2 \\[4pt]
\alpha_{gn}(\beta < \beta_{gn}) & \dfrac{6 - \beta}{2 - \beta}
\end{cases}
$$

$$
\begin{cases}
\dfrac{\partial(F_3 - F_2)}{\partial \beta} < 0 & \forall \alpha, n
\end{cases}
$$

over space ($\beta < \beta_{en}$). The current velocity decreases with n when combining a large injection rate ($\alpha > \alpha_{en}$) with a permeability decreasing or increasing moderately over space ($\beta < \beta_{en}$). For a Newtonian fluid ($n = 1$), the threshold value of α reduces to $\alpha_{en} = 3$.

Inspection of Table 6.2 shows that the thickness of the current increases with time at a given point ($F_3 > 0$) only when a large injection rate ($\alpha > \alpha_t$) is combined with permeability decreasing or increasing moderately over space ($\beta < \beta_t$); for decreasing permeability, the current encounters more resistance as it advances, while for a moderately increasing permeability, the decrease in medium resistance is more than compensated by the volume increase of the current. In all other cases, the thickness decreases over time, and does so for any α when the permeability increase is marked. For a Newtonian fluid ($n = 1$), the threshold value of α reduces to $\alpha_t = 2/(2 - \beta)$; for a homogeneous medium ($\beta = 0$) and any fluid, $\alpha_t = 2n/(n + 1)$. Furthermore, it is noted that F_3 decreases or increases with α depending whether a threshold value α_t is exceeded or not, or, equivalently, depending whether the increase in the volume of the current prevails over the permeability increase along the flow direction. The functional dependency of F_3 on n is the opposite of F_2 and the same threshold values due to mass balance. Finally, F_3 decreases with β for any combination of α, n, as an increase/less marked decrease of the permeability increases the radius of the current, thus implying a decrease in thickness due to mass balance. For the same reasons, the dependence of F_3 upon n is the opposite of F_2, with the threshold value α_{tn} being equal to α_{en}.

Inspection of Table 6.3 indicates that the aspect ratio/average spa-

tial gradient of the current increases with time $(F_3 - F_2 > 0)$ only when a large injection rate $(\alpha > \alpha_g)$ is combined with permeability decreasing or increasing moderately over space $(\beta < \beta_g)$; this behaviour can be understood noting that the average spatial gradient is proportional to the resistance encountered by the current in its advancement. Otherwise, the aspect ratio decreases with time, and the current grows progressively more elongated. For a Newtonian fluid $(n = 1)$, the threshold values reduce to $\alpha_g = 2/(2 - \beta)$, $\beta_g = 1$; for a homogeneous medium $(\beta = 0)$ and any fluid, $\alpha_g = 3$. The dependence of $F_3 - F_2$ on α is governed by a threshold value $\beta_{g\alpha}$; for $\beta > \beta_{g\alpha}$, $F_3 - F_2$ decreases with increasing α; the reverse is true for $\beta < \beta_{g\alpha}$. This is so because unless the permeability increase is marked, the aspect ratio of the current increases with the injection rate. The threshold is $\beta > \beta_{g\alpha} = 1$ for a Newtonian fluid. The behaviour of $F_3 - F_2$ as a function of n is analogous to F_2, with the same threshold values. Finally, $F_3 - F_2$ decreases with β for any combination of α, n, as a more permeable medium implies less resistance to the flow and a reduced average spatial gradient.

To visually illustrate the behaviour of the key exponent, Figures 6.3(a)-(f) depict how F_2, F_3 and $F_3 - F_2$ depend on β for fixed $n = 0.5$ and on n for fixed $\beta = -0.5$; results for various values of α, including the critical ones, are shown. The two reference values $(n = 0.5$ and $\beta = -0.5)$ are selected for illustrative purposes and represent common cases in natural porous media, i.e. a shear-thinning fluid and a permeability decreasing with distance from the source.

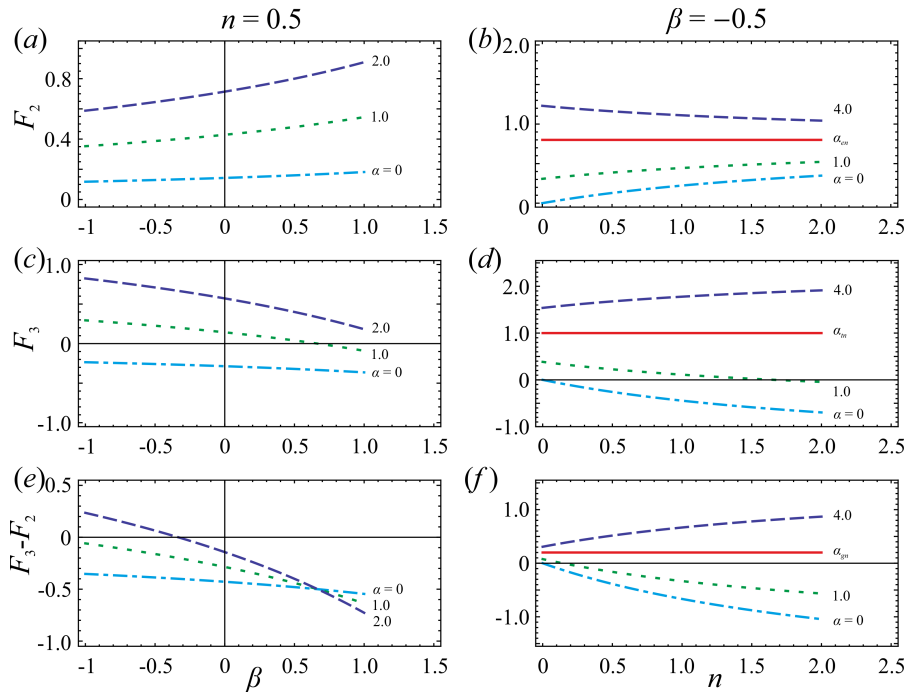A comparison of the threshold values of α and β reveals that: i)

Figure 6.3: (a)-(f) The value of the time exponents F_2, F_3 and $F_3 - F_2$ for a current with length $\propto T^{F_2}$, height $\propto T^{F_3}$, mean free-surface gradient/aspect ratio $\propto T^{F_3 - F_2}$, and volume $\propto T^{\alpha}$ in a porous medium with permeability varying horizontally as r^{β}. Results are shown for F_2, F_3 and $F_3 - F_2$ in the upper, intermediate and lower rows, respectively, as a function of β for $n = 0.5$ and as a function of n for $\beta = -0.5$ (left and right columns, respectively), and for different values of α. $\alpha_{en} = \alpha_{tn} = \alpha_{gn} = (6 - \beta)/(2 - \beta)$.
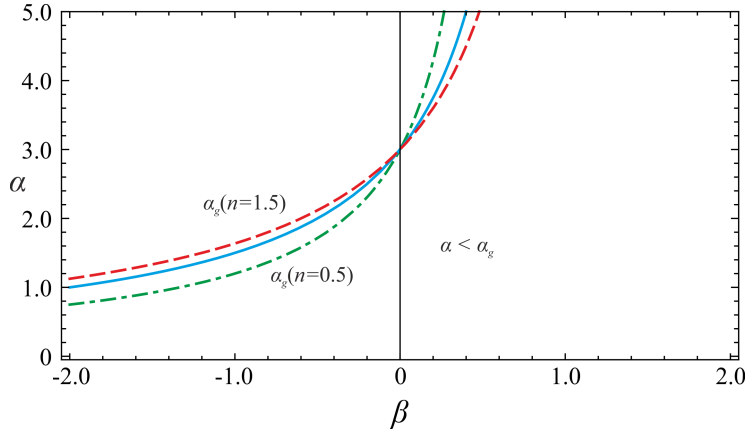
Figure 6.4: Limiting values of α to ensure an asymptotic decrease of the average steepness of the current, $\alpha < \alpha_g$ and $\beta < \beta_g$.

for a homogeneous medium ($\beta = 0$), all threshold values of α coalesce into 3, except for α_t; ii) for a Newtonian fluid ($n = 1$), the threshold values of α are β-dependent; iii) for Newtonian flow in a homogeneous medium, $\alpha_t = 1$. A plot of the limit α_g is shown in Figure 6.4 for $n = 0.5, 1, 1.5$. The limiting value of α increases with β; the increase is more rapid for $\beta > 0$. The influence of n on α_g is mixed, in that this limit value increases with n for $\beta < 0$ and decreases with n for $\beta > 0$. For a homogeneous medium, the limit α_g is independent of the behaviour index n.

6.4.2   Limits of validity

Limitations on the parameters emerge when considering the validity of model assumptions. At any time, conditions for the radius of

the current to increase with time must hold ($F_2 > 0$), as noted in the previous subsection. Furthermore, for $T \gg 1$ the thin current approximation requires the intruding current to be thin compared to both the characteristic height h_0 of the porous medium ($F_3 < 0$) and its height ($F_3 - F_2 < 0$). Otherwise, at large times i) the current thickness would exceed a reasonable portion of the porous domain total height, rendering invalid the assumption of immobile ambient fluid; ii) the aspect ratio of the current would increase without bounds, contrary to the assumption of negligible vertical velocities. Combining these limitations, the parameters domain satisfying all model assumptions asymptotically (the most restrictive condition) is obtained. An example is illustrated in Figure 6.5, where the two limits β_e and β_g are depicted, the first to ensure $F_2 > 0$, the second to ensure $F_3 - F_2 < 0$. It is seen that a too sharp increase in the permeability along the flow direction renders the current steeper with time; the limit β value is 0.67 for $n = 0.5$ and 1 for $n = 1$.

6.5 Laboratory experiments

6.5.1 Experimental setup

A series of experiments were conducted at the Hydraulic Laboratory of the University of Parma, to test the validity of the theoretical solution.

A 90° sector glass tank 25 cm × 25 cm × 25 cm in size was filled with transparent glass ballotini with nominal diameters of $d = 1.0, 2.0, 3.0, 4.0$ and 5.0 mm to reproduce a porous media whose per-
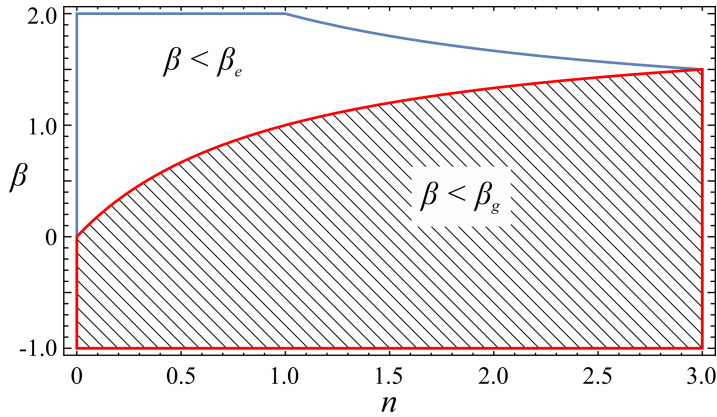
Figure 6.5: Limiting values of β to ensure a positive time advancing of the front of the current, $\beta < \beta_e \equiv (n+3)/(n+1)$, and an asymptotic decreasing average steepness of the current, $\beta < \beta_g \equiv 2n/(n+1)$.

meability varied along the horizontal direction. The continuous horizontal gradient of the permeability was obtained by using a plastic framework that allowed to create separate neighboring sectors, each of uniform permeability, reproducing a horizontal permeability variation. Five such vertical sectors were created, and each of them was gently filled with beads of uniform diameter. Figure 6.6 shows the radial distribution of the diameters and the permeability for $\beta = 1.65$. The horizontality of the bottom of the tank was checked by an electronic level. The intruding current was a shear-thinning fluid, made of softened water, glycerin and Xanthan Gum, mixed in two different proportions: (i) 40% (vol) of water, 60% (vol) of glycerin and 0.10% (weight) of Xanthan Gum, (ii) 95% (vol) of water, 5% (vol) of glyricerin and 0.15% (weight) of Xanthan Gum. Ink was added to the
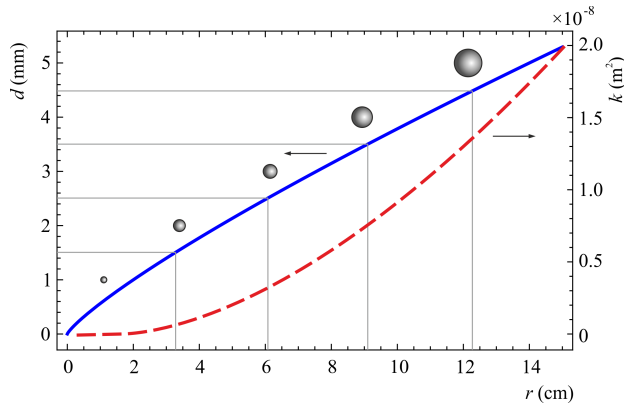
Figure 6.6: Radial distribution of the diameter of the ballotini (continuous curve) and of the permeability (dashed curve) for $\beta = 1.65$ and $k_0 = 1.986 \times 10^{-8}\,\mathrm{m}^2$.

final mixture for an easy visualization and detection of the interface. The rheological parameters (flow behaviour index n and consistency index m) were measured by a strain-controlled rheometer (Dynamic Shear Rheometer, Anton Paar Physica MCR 101), with parallel plates roughened by sandpaper P-60 glued onto both smooth surfaces. The distance between the plates was 1 mm and the testing temperature of the rheometer was $T = 25°\mathrm{C}$, approximately equal to the one measured in the laboratory during the experiments. The range of shear rate during measurements was chosen in order to overlap the range of shear rate expected during flow in the porous medium, following the criterion reported in Longo et al., 2013b. Figure 6.7 shows a sequence of measurements of the same fluid and the fitting power–law function.

The intruding fluid was injected with a syringe pump into the tank through a quarter-cylinder volume similar to a well, obtained with a
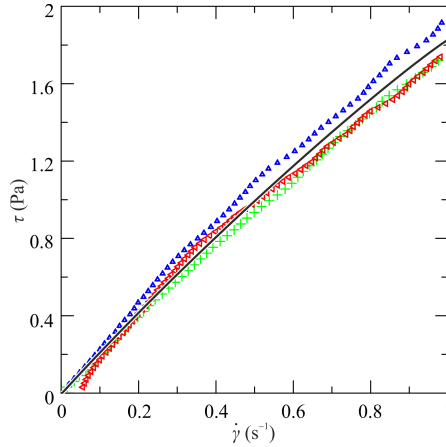
Figure 6.7: Stress-strain measurements. Three sequences of measurements were performed (symbols), and a power-law function was fitted to the experimental data (solid line).

brass net, which was located in one corner of the tank. This configuration reproduces an axisymmetric spreading due to the symmetry along the the vertical axis and with negligible influence of the wall boundary layers. The syringe pump was controlled by an analog electric signal to generate a constant ($\alpha = 1$) or waxing ($\alpha = 1.5, 2.0$) influx rate. During the injection, the lateral current profile was recorded by a high-resolution video-camera (Canon Legria HF 20, 1920×1080 pixels) working at 25 frames per second, while the bottom view was reflected by a mirror and captured by a photo-camera shooting every 2 seconds. The videos and images were post-processed using a software to transform the pixel positions into metric coordinates.

Figure 6.8 shows two typical images of the side- and bottom-view during one of the experiments.
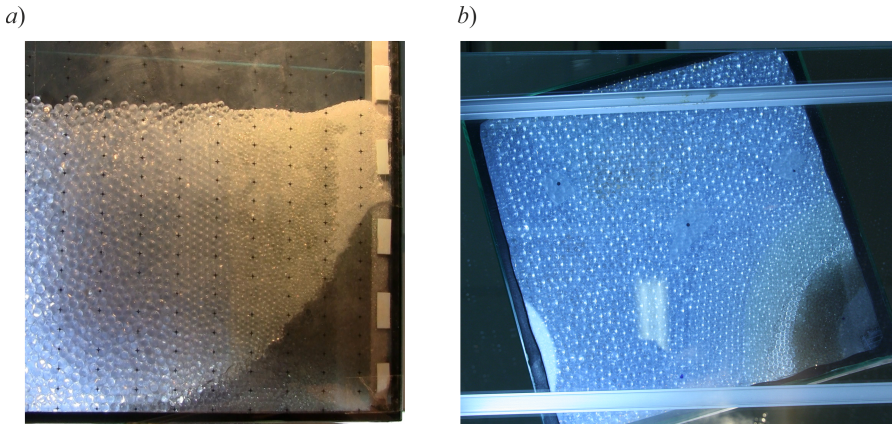
a)

b)

Figure 6.8: Typical images of the side- (*a*) and bottom-view (*b*) for one of the experiments. The radial increment of the diameter of the ballotini can be observed in both images.

6.5.2   Experimental results and discussion

A total of 10 experiments were performed; experimental parameters are summarized in Table 6.4. The horizontal permeability is controlled by the value of β, which was kept constant for all data sets, while the injection rate (α), the fluid rheology (m and n), and the fluid density (ρ) varied among the tests. Figure 6.9 depicts the front position x_n of the current for the various tests, compared with the theoretical prediction. For most tests, with the exception of A1 and A4, experimental results indicate a front position below the theoretical counterpart before reaching it asymptotically in all cases. The good agreement between theoretical and experimental data over time is due to the balance of buoyancy and viscous forces, while the effect of inertial forces influences the position of the front only at the begin-

ning of motion. The comparison between tests A4 and B3, which only differ in the type of fluid (having respectively $n=$ 0.45 and $n =$ 0.6), leads to the conclusion that the more pseudoplastic fluid (A4) best fits the theoretical model, and this result holds true since the beginning of the test. Furthermore, shear-thinning fluids advance slower with decreasing values of n, as showed upon comparing tests A5 and B4 for $\alpha \geq 2$.

The results of tests A2 and A3, characterized by different values of Q, i.e. 2.4 and 4.0 cm^3 s^{-1}, clearly show the same behavior, demonstrating that, all other parameters being equal, Q is not relevant in the evaluation of the front position x_n. Indeed, a little variation of density, e.g. between tests B2 and B5, proves that the fluid density ρ significantly affects the position of the front.

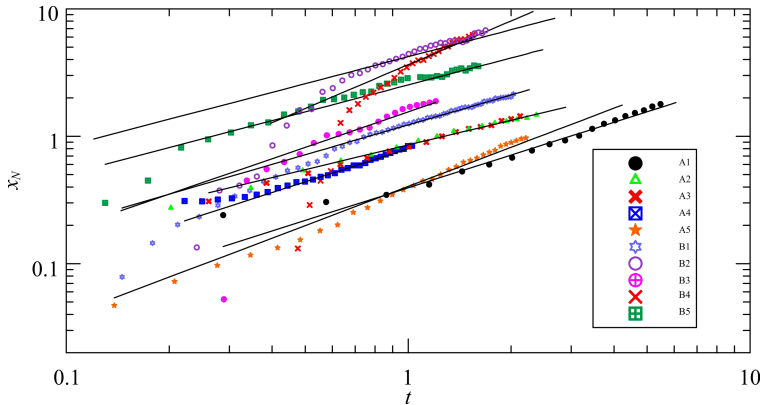| Exp.	Q (cm^3 s$^{-\alpha}$)	α	n	m (Pa s^n)	ρ (g cm^{-3})	β
A1	1.2000	1.0	1.00	0.071	1.221	1.65
A2	2.4000	1.0	0.45	0.800	1.176	1.65
A3	4.0000	1.0	0.45	0.800	1.176	1.65
A4	0.6400	1.5	0.45	0.800	1.176	1.65
A5	0.0292	2.1	0.20	1.020	1.176	1.65
B1	2.4000	1.0	0.80	1.210	1.086	1.65
B2	3.0800	1.0	0.60	0.600	1.086	1.65
B3	0.6400	1.5	0.60	0.600	1.086	1.65
B4	0.0292	2.0	0.60	0.600	1.086	1.65
B5	4.0000	1.0	0.60	0.600	1.088	1.65

Table 6.4: Experimental parameters.

Figure 6.9: The front position of the current. The symbols represent the experiments, the solid lines the theoretical data. The parameters of the experiments are listed in Table 6.4. Values have been translated in the vertical for easy visualization.

6.6 Overview on non-Newtonian porous gravity currents

The present section is devoted to an overview of self-similar solutions governing the propagation of non-Newtonian currents of variable volume with power-law rheology in porous media. The overview is performed by comparing the key parameters governing the propagation, i.e. F_2, F_3 and $F_3 - F_2$, equal to the time exponents of the extension, thickness, and slope of the current (derivation of the exponent of the velocity of the front end of the current, $F_2 - 1$, is trivial) for a variety of combinations of geometries and laws of variation of properties. For the case covered in the present paper (radial propagation in

an horizontally heterogeneous media) F_2,F_3 and $F_3 - F_2$ are reported in Equations (B.2), (B.3), and (6.22), respectively. Results for other geometries and/or laws of variation were derived in previous papers (Di Federico, Archetti, and Longo, 2012a; Di Federico, Archetti, and Longo, 2012b; Di Federico et al., 2014; Longo et al., 2015; Ciriello et al., 2016), always with the parameter α equal to the time exponent of the volume of the current. Table 6.5 covers results for plane geometry: the base unbounded case (Di Federico, Archetti, and Longo, 2012a) is compared to the channelized case of parameter κ (Longo et al., 2015), to vertical heterogeneity of parameter ω (Ciriello et al., 2016), and to horizontal heterogeneity of parameter β (Ciriello et al., 2016); see the Table caption for additional details. Table 6.6 lists results for radial geometry: the base case (Di Federico, Archetti, and Longo, 2012b) is compared to vertical heterogeneity of parameter ω (Di Federico et al., 2014), and to horizontal heterogeneity of parameter β (the present paper); again see caption for details.

Figure 6.10 depicts the behaviour of each key parameter for the homogeneous case as a function of geometry, n, and α. For all cases analyzed, the radial geometry implies lower values of all key parameters, with the exception of a continuous injection of very shear-thinning fluids in narrow cross sections. For an instantaneous fluid release ($\alpha = 0$), an increase of the rheological parameter n in radial geometry leads to F_2 values lower than other geometries, due to mass balance considerations. Among the plane cases, F_2 tends to decrease as the shape factor κ increases, tending to the unbounded case ($\kappa \to \infty$), as the volume of the current remains constant and the front of fluid is forced to move further for lower κ. In constant-flux regime ($\alpha = 1$),

	Plane unbounded (Di Federico, Archetti, and Longo, 2012a)	Plane channelized (Longo et al., 2015)	Plane, vertical heterogeneity (Ciriello et al., 2016)	Plane, horizontal heterogeneity (Ciriello et al., 2016)
F_2	$\dfrac{\alpha + n}{n+2}$	$\dfrac{\alpha\kappa + n(\kappa+1)}{n+1+\kappa(n+2)}$	$\dfrac{\alpha[(n+1)(\omega-1)+2]+2n}{2(n+2)+(n+1)(\omega-1)}$	$\dfrac{2(\alpha+n)}{2(n+2)-\beta(n+1)}$
F_3	$\dfrac{\alpha(n+1)-n}{n+2}$	$\dfrac{\kappa[\alpha(n+1)-n]}{n+1+\kappa(n+2)}$	$\dfrac{2[\alpha(n+1)-n]}{2(n+2)+(n+1)(\omega-1)}$	$\dfrac{\alpha(n+1)(2-\beta)-2n}{2(n+2)-\beta(n+1)}$
$F_3 - F_2$	$\dfrac{n(\alpha-2)}{n+2}$	$\dfrac{n[\alpha\kappa-(2\kappa+1)]}{n+1+\kappa(n+2)}$	$\dfrac{\alpha[2n-(n+1)(\omega-1)]-4n}{2(n+2)+(n+1)(\omega+1)}$	$\dfrac{\alpha[2n-\beta(n+1)]-4n}{2(n+2)-\beta(n+1)}$

Table 6.5: Formulation of parameters F_2, F_3 and $F_3 - F_2$ in plane geometry for the following cases: i) plane unbounded; ii) channelized flow of parameter κ, the width b of the cross-section is related to its height h by $b \propto y^\kappa$, $\kappa < 1/ = / > 1$ corresponds to narrow/triangular/wide cross-sections, with $\kappa \to \infty$ indicating the unbounded case; iii) vertical heterogeneity with permeability varying along y as $k \propto y^{\omega-1}$, $\omega = 1$ corresponds to the homogeneous case; iv) horizontal heterogeneity with permeability varying along x as $k \propto x^\beta$, $\beta = 0$ corresponds to the homogeneous case.

	Radial (Di Federico, Archetti, and Longo, 2012b)	Radial, vertical heterogeneity (Di Federico et al., 2014)	Radial, horizontal heterogeneity [pp]
F_2	$\dfrac{\alpha + n}{n+3}$	$\dfrac{\alpha[(n+1)(\omega-1)+2]+2n}{2(n+3)+2(n+1)(\omega-1)}$	$\dfrac{2(\alpha+n)}{2(n+3)-\beta(n+1)}$
F_3	$\dfrac{\alpha(n+1)-2n}{n+3}$	$\dfrac{\alpha(n+1)-2n}{2(n+3)+2(n+1)(\omega-1)}$	$\dfrac{\alpha(n+1)(2-\beta)-4n}{2(n+3)-\beta(n+1)}$
$F_3 - F_2$	$\dfrac{n(\alpha-3)}{n+3}$	$\dfrac{\alpha[2n-(n+1)(\omega-1)]-6n}{2(n+3)+2(n+1)(\omega-1)}$	$\dfrac{\alpha[2n-\beta(n+1)]-6n}{2(n+3)-\beta(n+1)}$

Table 6.6: Formulation of parameters F_2, F_3 and $F_3 - F_2$ in radial geometry for the following cases: i) pure radial; ii) vertical heterogeneity with permeability varying along y as $k \propto y^{\omega-1}$, $\omega = 1$ corresponds to the homogeneous case; iii) horizontal heterogeneity with permeability varying along r as $k \propto r^\beta$, $\beta = 0$ corresponds to the homogeneous case. *pp* indicates the present paper.
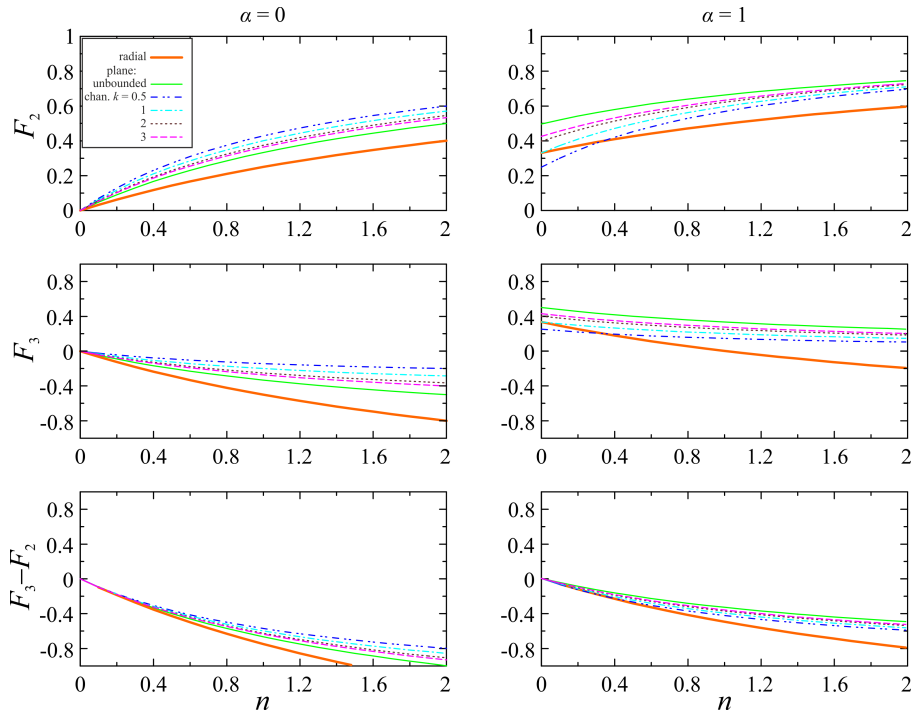
Figure 6.10: Parameters F_2 (upper row), F_3 (intermediate row) and $F_3 - F_2$ (lower row) as a function of n, for instantaneous ($\alpha = 0$, left column) and continuous injection ($\alpha = 1$, right column), with homogeneous permeability ($\omega = 1$, $\beta = 0$), for radial, plane, and plane channelized geometry of various parameters κ.

radial geometry and $n > 0.5$, F_2 behaves as in the constant-volume regime, while for plane geometries it shows an opposite behavior, i.e. F_2 increases with higher values of κ. In constant-volume regime ($\alpha = 0$), the parameter F_3 is negative for all the analyzed geometries. In general, this exponent tends to decrease when moving to plane unbounded geometry. In constant flux regime, F_3 is negative only for radial geometry and dilatant fluids ($n > 1$), whilst in plane geometries F_3 tends to increase with the shape factor κ, as does F_2.

For all geometries, the parameter $F_3 - F_2$ is always negative for $\alpha \leq 1$, because of the higher limit of validity for shear thinning fluids. The parameter reaches lower values in constant-volume regime ($\alpha = 0$), and is larger for plane than for radial geometry. The influence of κ on results is more limited as κ increases. Figure 6.11 illustrates the trend of parameters F_2, F_3 and $F_3 - F_2$, considering vertical permeability variations in plane and radial geometry. The homogeneous case with $\omega = 1$ (Di Federico et al., 2014; Ciriello et al., 2016), is depicted in Figure 6.10. In both plane and radial geometry, for an instantaneous fluid release ($\alpha = 0$) and $\omega < 1$, F_2 is higher than the homogeneous case depicted in Figure 6.10, whilst it is lower if $\omega > 1$. This trend changes for a constant-flux regime ($\alpha = 1$). For $\omega < 1$, and plane geometry, F_2 is lower than the homogeneous case, and it becomes higher if $\omega > 1$. In the radial case, for $\omega < 1$, F_2 is lower than the homogeneous case, but only for a shear thinning fluid ($n < 1$), while it becomes higher for a dilatant fluid ($n > 1$). On the contrary, if $\omega > 1$, F_2 shows an opposite behavior.

Concerning the parameter F_3, in constant-volume regime ($\alpha <= 0$) and both geometries, this parameter is lower than the homogeneous
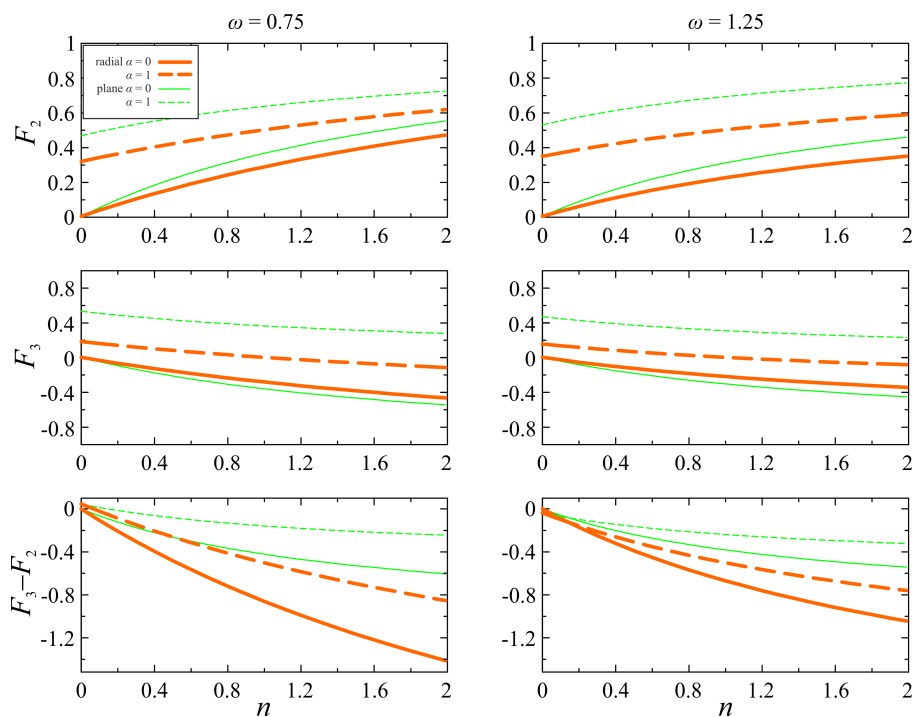
Figure 6.11: Permeability varying in the vertical direction. Parameters F_2 (upper row), F_3 (intermediate row) and $F_3 - F_2$ (lower row) as a function of n, for permeability decreasing ($\omega = 0.75$, left column) and increasing along the vertical ($\omega = 1.25$, right column), radial/plane geometry (orange/green lines) and instantaneous ($\alpha = 0$, solid line)/continuous ($\alpha = 1$, dashed line) injection.

case for $\omega < 1$, while it becomes higher if $\omega > 1$. For continuous injection ($\alpha = 1$), in plane unbounded geometry, F_3 is higher than the homogeneous case if $\omega < 1$, and it reverses its behaviour with $\omega > 1$. In radial case, for $\omega < 1$, F_3 is higher than homogeneous case, only for a shear thinning fluid ($n < 1$), while it becomes lower for a dilatant fluid ($n > 1$). On the contrary, if $\omega > 1$, F_3 has an opposite trend.

For an instantaneous release ($\alpha = 0$), in both geometries, $F_3 - F_2$ is lower than the homogeneous case for $\omega < 1$, while it reverses its behaviour if $\omega > 1$. For continuous injection ($\alpha = 1$), in plane unbounded geometry, $F_3 - F_2$ is higher than the homogeneous case if $\omega < 1$, reversing for $\omega > 1$; in radial geometry, instead, the behavior is similar to F_3. For both geometries, independently on vertical permeability variations, the deviation between homogeneous (Figure 6.10) and heterogeneous values (Figure 6.11) tends to increase if n increases for $\alpha = 0$, and it decreases for constant injections only in plane geometry. Figure 6.12 depicts the behavior of parameters F_2, F_3 and $F_3 - F_2$, considering horizontal permeability variations in plane and radial geometry; the homogeneous case ($\beta = 0$) is depicted in Figure 6.10 (Ciriello et al., 2016). In both geometries and regimes, i.e. constant-volume and constant-flux, for $\beta < 0$, F_2 is lower than homogeneous case, while its behaviour is reversed if $\beta > 0$. For $\beta < 0$, the parameter F_3 is higher than the homogeneous case for all geometries and regimes, whilst it becomes lower if $\beta > 0$. Finally, $F_3 - F_2$ follows the same trend of F_3. For both releases, geometries, and horizontal permeability variations, the deviation between homogeneous and heterogeneous case tends to increase for higher n values.
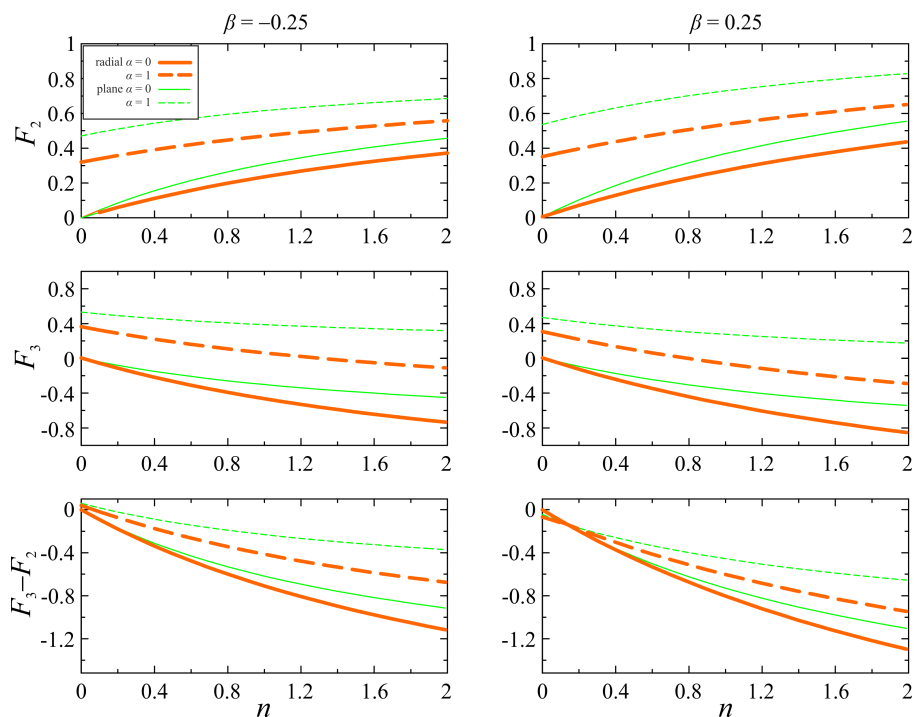
Figure 6.12: Permeability varying in the horizontal direction. Parameters F_2 (upper row), F_3 (intermediate row) and $F_3 - F_2$ (lower row) as a function of n, for permeability decreasing ($\beta = -0.25$, left column) and increasing along the horizontal ($\beta = 0.25$, right column), radial/plane geometry (orange/green lines) and instantaneous ($\alpha = 0$, solid line)/continuous ($\alpha = 1$, dashed line) injection.

6.7   Final remarks

A novel model describing the propagation of axisymmetric power-law GCs in porous media with an horizontal permeability variation has been presented. The problem is amenable to a self-similar solution of the first kind yielding the position of the front end and the thickness of the current as functions of dimensionless parameters describing the volume of the GC (α), its rheological behaviour (n), and the permeability variation (β). The special case of constant volume currents has a closed-form solution. The behaviour of key time exponents governing the rate of propagation, thickness and aspect ratio of the current was discussed in detail, yielding a number of threshold value of model parameters α and β which discriminate between opposite trends in the behaviour of the current over time and govern the sensitivity to model parameters themselves. In turn, these parameters allow to discriminate the conditions for the validity of our solution at large times. A specific laboratory setup was devised to directly reproduce horizontal permeability variations, overcoming the difficulties inherent in the horizontal juxtaposition of layers of glass beads of different diameter. Theoretical results were confirmed by our experiments, with a fairly good agreement except for the early-time regime. It is confirmed that also in presence of space varying permeability (at least with a deterministic variation), disturbances or anomalies near the injection line and near the front of the current, do not affect the current evolution in the intermediate asymptotic regime. Also the discretization of the porous medium to mimic a continuous variation of permeability and capillary effects do not significantly affect the behaviour of the GCs, at least for constant influx rate condition ($\alpha = 1$). More important

disturbances are expected for constant volume experiments ($\alpha = 0$) and, in general, for waning GCs. The theory and experiments herein presented complete a first picture on porous gravity currents of power-law fluid flowing in plane and axisymmetric geometry. The reference solutions are derived by Di Federico *et al.* Di Federico, Archetti, and Longo, 2012a for plane and by Di Federico *et al.* Di Federico, Archetti, and Longo, 2012b for radial flow. The influence of channel shape on plane flow is covered in Longo *et al.* Longo et al., 2015. Heterogeneous, deterministic variations of properties are examined by Ciriello *et al.* Ciriello et al., 2016 considering vertical and horizontal grading in 2-D flows, and by Di Federico *et al.* Di Federico et al., 2014 considering vertical grading in radial flow; horizontal grading is covered in the present paper. An overview of the key time exponents for these cases revealed the combination of geometries and model parameters yielding the fastest/lowest currents, and those having the fastest decrease of thickness and aspect ratio over time.

This study has several connections to geological flows and industrial flows, including flows during fracking procedures, shale gas recovery, drilling wells, CO_2 storage. In all these applications, several fluids exhibiting non–Newtonian effects (often approximated by power-law fluids) are used, almost always in heterogeneous porous media. The radial variation of permeability/porosity around the wells is also due to the adopted technology.

Several promising avenues of investigation remain open in the area of non-Newtonian GCs, e.g.

- inclusion of fluid drainage at the bottom of the current, either distributed or concentrated in fissures;

- inclusion of stratification effects in the advancing current;

- adoption of more realistic rheological models to describe complex fluids, such as Carreau or truncated power-law;

- advanced modeling of heterogeneity.

Chapter 7

Conclusions

This thesis is devoted to the provision of new approaches to deal with groundwater risk assessment under uncertainty. The main results are the following:

i show how it is possible to conjugate the need for accuracy in prediction and reduction of computational cost associated with stochastic analysis by resorting to metamodeling techniques;

ii show the convenience of decomposing the complex problem of groundwater risk assessment into basic events that can be treated separately by means of appropriate conceptual models and Global Sensitivity Analysis/Uncertainty Quantification methods;

iii underline that an appropriate application of European Directive's principles, as well as the construction of summary indicators, can not lie outside the use of an exhaustive risk analysis approach.

These results have been reached:

i by describing an effective set of stochastic methods that can
be effectively contextualized within the Polynomial Chaos Ex-
pansion theory and further extending them in the context of
distribution based Global Sensitivity Analysis (Chapter 2)

ii by analyzing the case (basic event) of LNAPL contamination
and suggesting probabilistic metrics to quantify the correspon-
dent potential impact (Chapter 3; publication: "Impact of Hy-
drogeological Uncertainty on Estimation of Environmental Risks
Posed by Hydrocarbon Transportation Networks", Water Re-
sources Research, 53(11): 8686-8697 (V. Ciriello, I. Lauriola, S.
Bonvicini, V. Cozzani, V. Di Federico, e Daniel M. Tartakovsky,
2017))

iii by showing how the suggested stochastic framework may also
act in the context of the construction of scenarios, such as future
climate scenarios at the river-basin scale (Chapter 4)

iv by describing how the use of Global Sensitivity Analysis can
assist parameter estimation when calibrating models or deriv-
ing indications for practical applications, such as for soil mois-
ture estimation with an innovative indirect technique (Chapter
5; publication: "Impacts of uncertainty in soil texture parame-
ters on estimation of soil moisture through radio waves transmis-
sion", Advances in Water Resources, Vol. 122 pp 131-138, (E.
Di Fusco, I. Lauriola, R. Verdone, V. Di Federico, V. Ciriello,
2018))

v by developing simplified conceptual models for the case (basic event) of intrusions, such as gravity currents, in the subsurface domain (Chapter 6, publication: "Porous gravity currents: axisymmetric propagation in horizontally graded medium and a review of similarity solutions", Advances in Water Resources, Vol. 115 pp 136–150, (Lauriola I., Felisa G., Petrolo D., Di Federico V., Longo S., 2018))

Appendix A

Influence of two-path transmission

Results presented below refer to a couple of devices at a distance $d = 3$ m and depth $z_1 = z_2 = 0.2$ m. In this configuration, the ground surface is responsible for reflection of the signal towards the receiver. Figures A.1 - A.3 depict the same results of Figures 5.2 - 5.4, for the two-path transmission mechanism. The same holds for Table 3.2 and Figure A.4 with respect to Table 2.2 and Figure 5.5. It is possible to observe that GSA results, as well as the variance of the response, are very similar to those derived for the single path model. Main differences involve the trend of $\langle L_p \rangle(f)$ curves for constant m_v, especially for low path loss values. Given these results, and considering that in the most of applications the single path mechanism holds, it seems not relevant to analyze the effect of ground surface reflection if the aim is to understand which parameter influences more the predictive uncertainty. Furthermore, the two-path model includes a couple of ad-

ditional parameters, ϕ and Γ, thus making calibration challenging in practical applications. As such, it seems generally convenient to perform GSA and uncertainty quantification on the single path model, in order to characterize and reduce the predictive uncertainty, by addressing measurements towards the most significant parameters.

Table A.1: Two-path model: GSA outcomes for two possible experimental settings with $d = 3$m and $f = 0.868$ GHz or $f = 0.433$ GHz.

| f	Soil type	$\langle L_p \rangle$ (dB)	m_v range	influential parameters
0.868 GHz	CL	$107 \div 151$	$0.05 \div 0.19$	$S_n = 0.61 \div 0.80$
				$S_S = 0.24 \div 0.03$
				$S_C = 0.14 \div 0.16$
0.868 GHz	L	$100 \div 151$	$0.05 \div 0.31$	$S_n = 0.33 \div 0.41$
				$S_S = 0.17 \div 0.01$
				$S_C = 0.43 \div 0.52$
0.868 GHz	SL	$96 \div 143$	$0.05 \div 0.50$	$S_n = 0.11 \div 0.15$
				$S_S = 0.02 \div 0.19$
				$S_C = 0.63 \div 0.57$
0.433 GHz	CL	$105 \div 151$	$0.05 \div 0.39$	$S_n = 0.65 \div 0.82$
				$S_S = 0.21 \div 0.01$
				$S_C = 0.13 \div 0.16$
0.433 GHz	L	$98 \div 133$	$0.05 \div 0.50$	$S_n = 0.37 \div 0.37$
				$S_S = 0.13 \div 0.10$
				$S_C = 0.42 \div 0.48$
0.433 GHz	SL	$93 \div 106$	$0.05 \div 0.50$	$S_n = 0.11 \div 0.14$
				$S_S = 0.01 \div 0.27$
				$S_C = 0.62 \div 0.50$
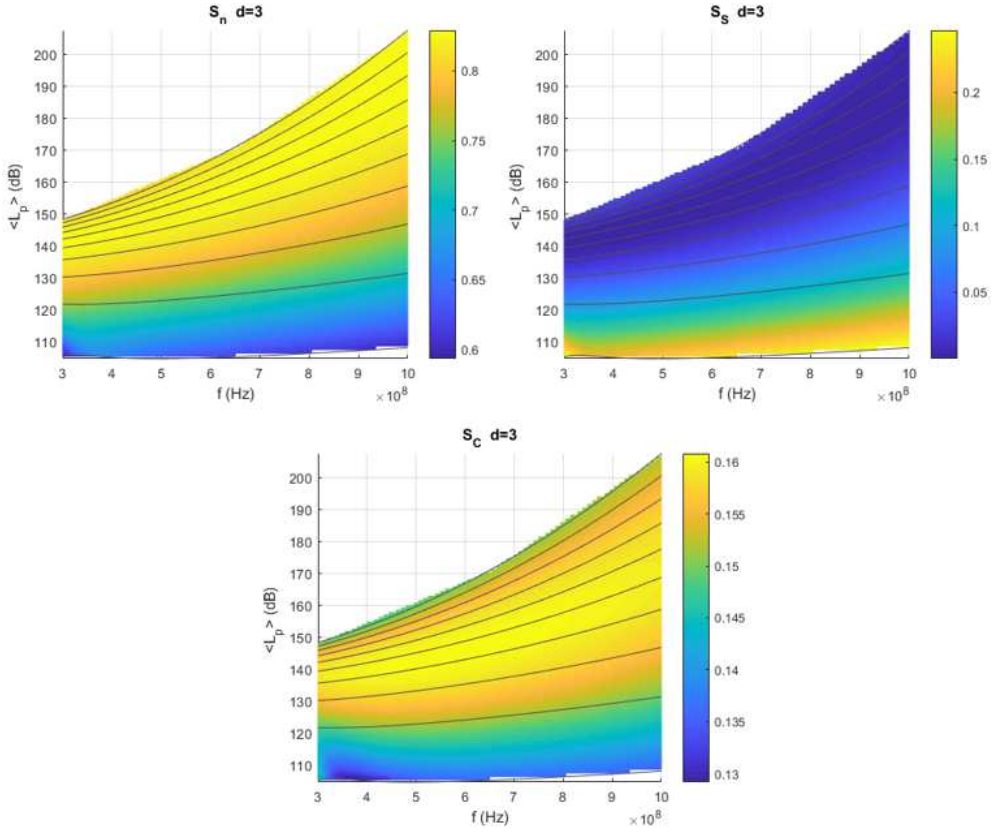
Figure A.1: Two-path model: variations of S_n, S_S, S_C in case of clay-loam in the $(\langle L_p \rangle, f)$ plane. Grey lines denote constant values for m_v between 0.05 (the lowest) and 0.5 (the highest), with a constant step of 0.05.
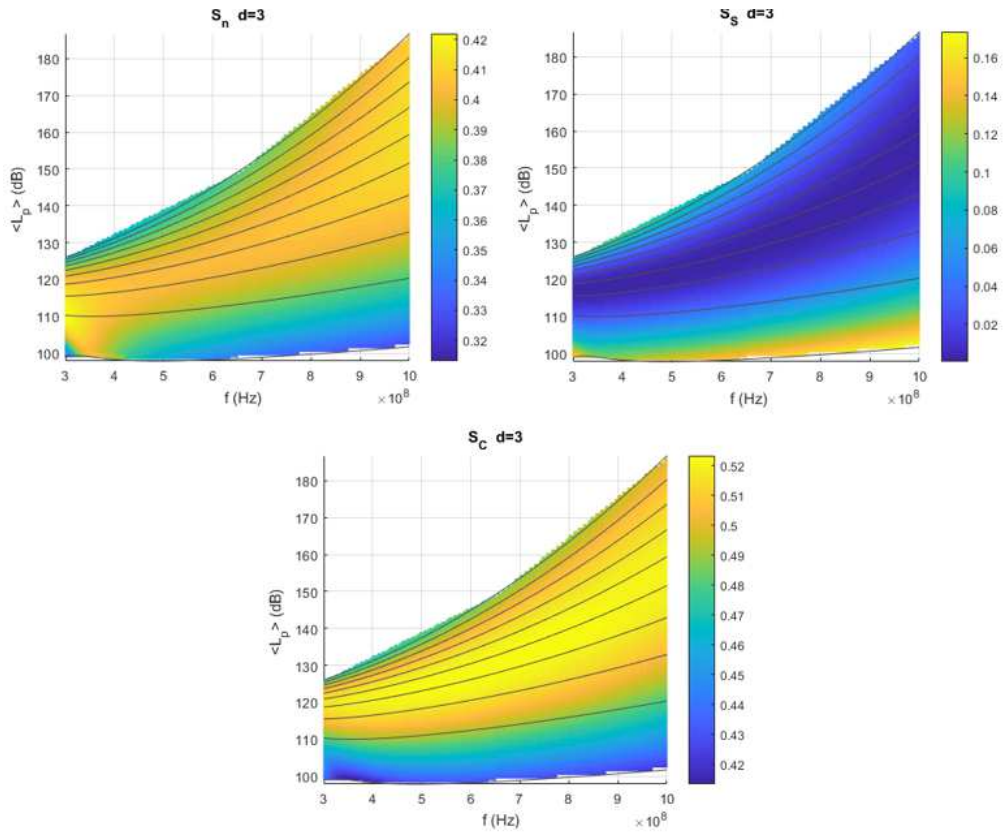
Figure A.2: Two-path model: variations of S_n, S_S, S_C in case of loam in the $(\langle L_p \rangle, f)$ plane. Grey lines denote constant values for m_v between 0.05 (the lowest) and 0.5 (the highest), with a constant step of 0.05.
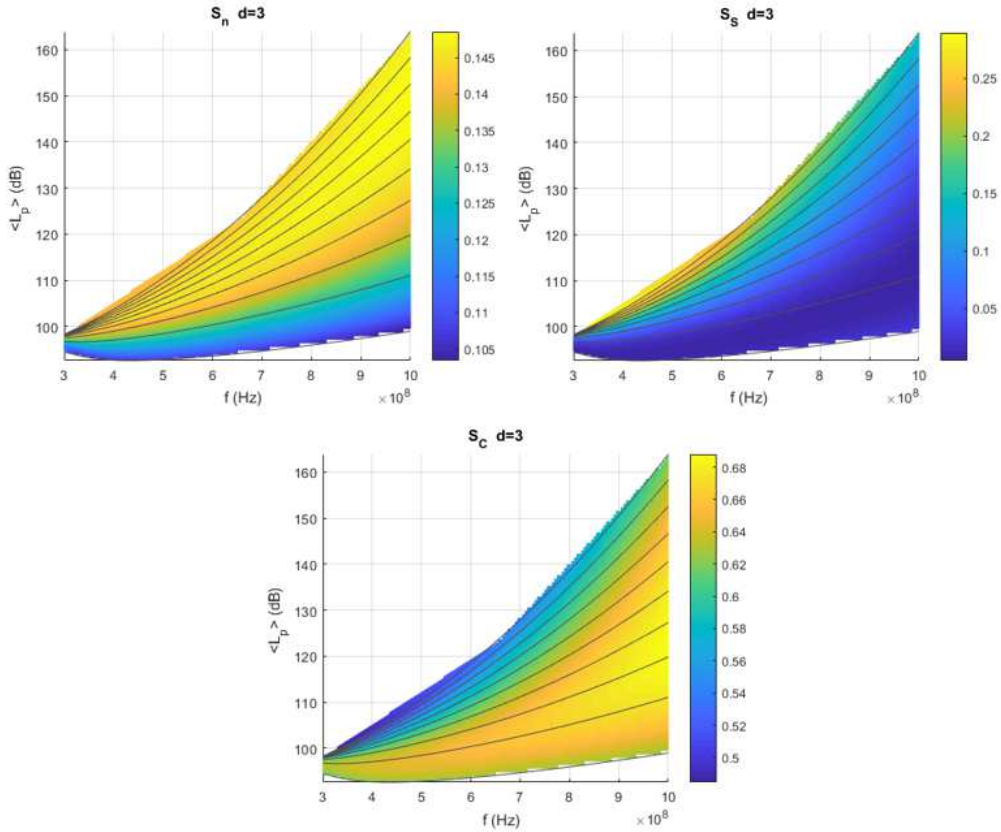
Figure A.3: Two-path model: variations of S_n, S_S, S_C in case of sandy-loam in the $(\langle L_p \rangle, f)$ plane. Grey lines denote constant values for m_v between 0.05 (the lowest) and 0.5 (the highest), with a constant step of 0.05.
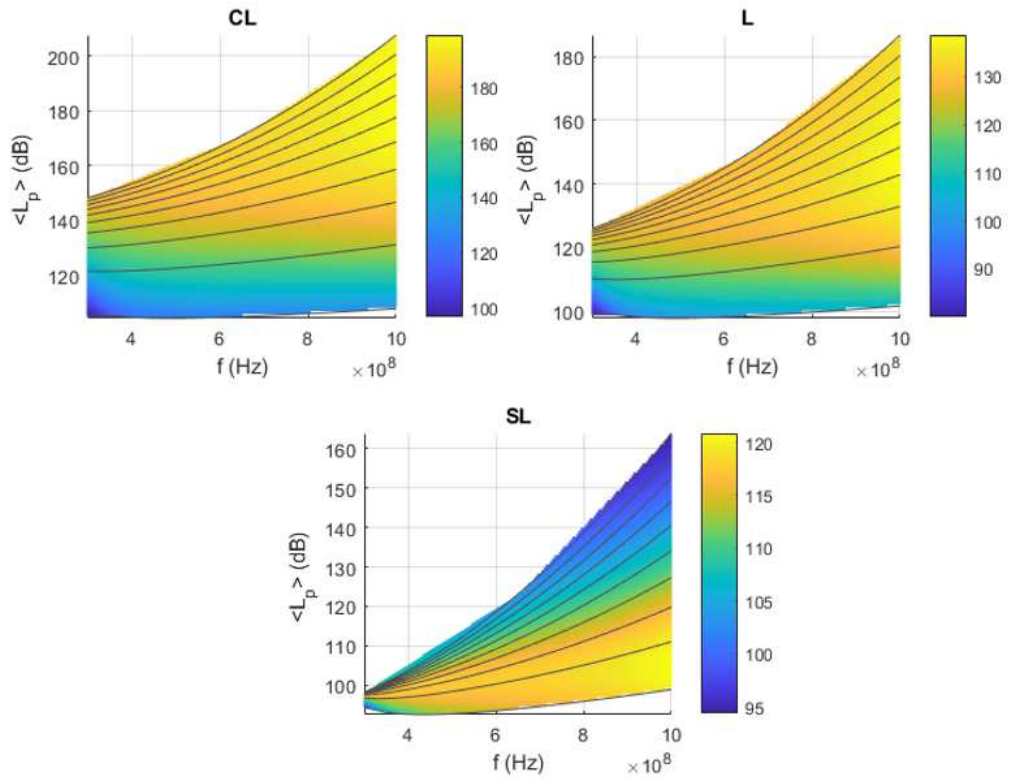
Figure A.4: Two-path model: maps of variance in case of clay-loam (CL), loam (L) and sandy-loam (SL) in the $(\langle L_p \rangle, f)$ plane. Grey lines denote constant values for m_v between 0.05 (the lowest) and 0.5 (the highest), with a constant step of 0.05.

Appendix B

Self-similar solution

Inspection of Eq. (6.10) yields the following time scalings for the length R and thickness H of the current

$$R \sim T^{F_2}, H \sim T^{F_3} \tag{B.1}$$

where

$$F_2 = \frac{2(\alpha + n)}{2(n + 3) - \beta(n + 1)}, \tag{B.2}$$

$$F_3 = \frac{\alpha(n + 1)(2 - \beta) - 4n}{2(n + 3) - \beta(n + 1)}. \tag{B.3}$$

This suggests the adoption of the similarity variable

$$\eta = R/T^{F_2}, \tag{B.4}$$

which in turn leads to the expression of the position of the front and of the thickness respectively as

$$R_N(T) = \eta_N T^{F_2}, \tag{B.5}$$

$$H(R,T) = T^{F_3} f(\eta), \qquad (B.6)$$

where η_N is the η value at the front $R = R_N(T)$. The function $f(\eta)$ may be recast as $f(\eta) = \eta_N^{F_5} \psi(\zeta)$ via the introduction of the normalized similarity variable $\zeta = \eta/\eta_N$, where

$$F_5 = \frac{(n+1)(2-\beta)}{2}, \qquad (B.7)$$

and $\psi(\zeta)$ is the thickness profile. Substituting $f(\eta)$ in (B.6) gives

$$H(R,T) = \eta_N^{F_5} T^{F_3} \psi(\zeta), \qquad (B.8)$$

and adoption of the latter expression for the thickness transforms: i) Eq. (6.10) into the ODE (6.13); ii) the condition (6.12) into (6.15); iii) the boundary condition (6.5) into (6.14). These three equations are reported in the main body of this chapter.

Bibliography

De Marsily, G. (1980). *Hydrogéologie quantitative*. Masson.

Ahmad, M. et al. (2018). "Modelling soil water dynamics and crop water use in a soybean-wheat rotation under chisel tillage in a sandy clay loam soil". In: *Geoderma* 327. cited By 0, pp. 13–24.

Akyildiz, Ian F. and Erich P. Stuntebeck (2006). "Wireless underground sensor networks: Research challenges". In: *Ad Hoc Networks* 4.6, pp. 669 –686. ISSN: 1570-8705.

Akyildiz, Ian F., Zhi Sun, and Mehmet C. Vuran (2009). "Signal propagation techniques for wireless underground communication networks". In: *Physical Communication* 2.3, pp. 167 –183. ISSN: 1874-4907.

Alcamo, J., T. Henrichs, and T. Rösch (2000). *World water in 2025: Global modeling and scenario analysis for the World Commission on Water for the 21st Century, Kassel World Water Ser. Rep. 2*. Tech. rep. Univ. of Kassel, Kassel, Germany.: Cent. for Environ. Syst. Res.

Allen, R. G. et al. (1998). *Crop Evapotranspiration (guidelines for computing crop water requirements)*. FAO Irrigation and Drainage Paper No. 56. Food and Agriculture Organization (FAO).

Antolini, G. et al. (2017). *Atlante climatico dell'Emilia-Romagna 1961-2015*. Tech. rep. Arpae Emilia-Romagna - Servizio IdroMeteoClima.

Archer, G. E. B., A. Saltelli, and I. M. Sobol (1997). "Sensitivity measures, ANOVA like techniques and the use of bootstrap". In: *J. Stat. Comput. Sim.* 58, pp. 99–120.

Arpa (2007). *Elaborazione ed analisi dati raccolti sulle acque superficiali e sotterranee a livello locale per lo sviluppo dei piani di tutela delle acque - Modello di flusso e trasporto di nitrati nelle acque sotterranee della regione Emilia-Romagna*. Rapporto tecnico N. 75. Regione Emilia-Romagna.

— (2008). *Rete regionale di monitoraggio delle acque sotterranee*. Rapportotecnico. Regione Emilia-Romagna.

— (2009). *Applicazione della modellistica matematica di simulazione - Analisi del flusso delle acque sotterranee in relazione a scenari caratterizzati da particolari criticità nel rapporto ricarica prelievi*. Tech. rep. Regione Emilia-Romagna.

Ashraf, M., S. Oladyshkin, and W. Nowak (2013). "Geological storage of CO2: Application, feasibility and efficiency of global sensitivity analysis and risk assessment using the arbitrary polynomial chaos". In: *Int. J. Greenhouse Gas Control* 19.2, pp. 704–719.

Assouline, S., V. Ciriello, and D. M. Tartakovsky (2017). "Estimation of Intrinsic Length Scales of Flow in Unsaturated Porous Media". In: *Water Resources Research* 53.11, pp. 9980–9987.

Balanis, C. A. (2012). *Advanced Engineering Electromagnetics*. Wiley.

Ball, T. V. et al. (2017). "The relaxation time for viscous and porous gravity currents following a change in flux". In: *Journal of Fluid Mechanics* 821, pp. 330–342. DOI: 10.1017/jfm.2017.243.

Barajas-Solano, D. A. and D. M. Tartakovsky (2016). "Stochastic collocation methods for nonlinear parabolic equations with random coefficients". In: *SIAM/ASA J. Uncert. Quant.* 4.1, pp. 475–494. DOI: 10.1137/130930108.

Bayer, P., C. M. Burger, and M. Finkel (2008). "Computationally efficient stochastic optimization using multiple realizations". In: *Adv Water Resour*.

Bayer, P., M. de Paly, and C. M. Burger (2010). "Optimization of high-reliability-based hydrological design problems by robust automatic sampling of critical model realizations". In: *Water Resour Res*.

Bedford, T. and R. Cooke (2006). *Probabilistic Risk Analysis: Foundations and Methods*. Fourth Edition. Cambridge University Press. ISBN: 0 521 77320 2.

Bittelli, M. (2011). "Measuring Soil Water Content: A Review". In: *HortTechnology* 21.3, pp. 293–300.

Bjornara, T. I., J. M. Nordbotten, and J. Park (2016). "Vertically integrated models for coupled two-phase flow and geomechanics in porous media". In: *Water Resources Research* 52.2, pp. 1398–1417. ISSN: 1944-7973. DOI: 10.1002/2015WR017290.

Bolster, D. et al. (2009). "Probabilistic risk analysis of groundwater remediation strategies". In: *Water Resour. Res.* 45(6), W06413.

Bonvicini, S. et al. (2015). "Quantitative assessment of environmental risk due to accidental spills from onshore pipelines". In: *Process Saf. Environ.* 93, pp. 31–49.

Borgonovo, E. (2007). "A new uncertainty importance measure". In: *Reliability Engineering & System Safety* 92.6, pp. 771–784.

Boulay, A. M. et al. (2011). "Regional Characterization of Freshwater Use in LCA: Modeling Direct Impacts on Human Health". In: *Environmental Science & Technology, Environ. Sci. Technol., 45 (20):8948–8957.*

Brandhorst, N., D. Erdal, and I. Neuweiler (2017). "Soil moisture prediction with the ensemble Kalman filter: Handling uncertainty of soil hydraulic parameters". In: *Advances in Water Resources* 110, pp. 360 –370. ISSN: 0309-1708.

Calera, A. et al. (2005). "Irrigation management from space: Towards user-friendly products". In: *Irrigation and Drainage Systems, 19, 337-353.*

Carsel, R. F. and R. S. Parrish (1988). "Developing joint probability distributions of soil water retention characteristics". In: *Water Resour. Res.* 24(5), pp. 755–769.

CCPS (1995). *Guidelines for Chemical Transportation Risk Analysis.* Tech. rep. Centre for Chemical Process Safety, American Institution of Chemical Engineers, New York.

Charbeneau, R. J. and J. W. Weaver (1992). "Modeling contaminant transport through subsurface systems". In: *J. Hazard. Mater.* 32 (2-3), pp. 293–311.

Charbeneau, R. J., J. W. Weaver, and B. K. Lien (1995). *The Hydrocarbon Spill Screening Model (HSSM) Volume 2: Theoretical Background and Source Codes.* Tech. rep. EPA/600/R-94/039b. US Environmental Protection Agency.

Chiapponi, L. (2017). "Water retention curves of multicomponent mixtures of spherical particles". In: *Powder Technology* 320, pp. 646– 655. DOI: `10.1016/j.powtec.2017.07.083`.

Ciriello, V. (2013). "Model reduction of stochastic groundwater flow and transport processes". PhD thesis. Alma Mater Studiorum Università di Bologna. DOI: DOI10.6092/unibo/amsdottorato/5937.

Ciriello, V., S. Longo, and V. Di Federico (2013). "On shear thinning fluid flow induced by continuous mass injection inporous media with variable conductivity". In: *Mech Res Comm* 5, pp. 101–107. DOI: 10.1016/j.mechrescom.2013.07.006.

Ciriello, V. et al. (2013a). "Comparative analysis of formulations for conservative transport in porous media through sensitivity-based parameter calibration". In: *Water Resour. Res.* 49.9, pp. 5206–5220.

Ciriello, V. et al. (2013b). "Effect of variable permeability on the propagation of thin gravity currents in porous media". In: *Int. J. Non-Linear Mech.* 57, pp. 168–175. DOI: 10.1016/j.ijnonlinmec.2013.07.003.

Ciriello, V. et al. (2013c). "Polynomial Chaos Expansion for Global Sensitivity Analysis applied to a model of radionuclide migration in a randomly heterogeneous aquifer". In: *Stoch. Environ. Res. Risk. Assess.* 27, pp. 945–954.

Ciriello, V. et al. (2015). "Multimodel framework for characterization of transport in porous media". In: *Water Resour. Res.* 51(5), pp. 3384–3402.

Ciriello, V. et al. (2016). "Porous gravity currents: A survey to determine the joint influence of fluid rheology and variations of medium properties". In: *Advances in Water Resources* 92, pp. 105 –115. DOI: 10.1016/j.advwatres.2016.03.021.

Ciriello, V. et al. (2017). "Impact of Hydrogeological Uncertainty on Estimation of Environmental Risks Posed by Hydrocarbon Transportation Networks". In: *Water Resour. Res.* 53, WR021368.

Cristopher, R. H. and S. Middleman (1965). "Power-law flow through a packed tube". In: *Ind. Eng. Chem. Fundam.* 4, pp. 422–427. DOI: 10.1021/i160016a011.

Deman, G. et al. (2015). "Sensitivity analysis of groundwater lifetime expectancy to hydro-dispersive parameters: The case of ANDRA Meuse/Haute-Marne site". In: *Reliab. Eng. Syst. Safety* 134, pp. 276–286.

Di, C., X. Yang, and X. Wang (2014). "A Four-Stage Hybrid Model for Hydrological Time Series Forecasting". In: *PLOS ONE, 9(8).*

Di Federico, V., R. Archetti, and S. Longo (2012a). "Similarity solutions for spreading of a two-dimensional non-Newtonian gravity current". In: *J. Non-Newtonian Fluid Mech.* 177–178, pp. 46–53. DOI: 10.1016/j.jnnfm.2012.04.003.

— (2012b). "Spreading of axisymmetric non-Newtonian power-law gravity currents in porous media". In: *J. Non-Newtonian Fluid Mech.* 189–190, pp. 31–39. DOI: 10.1016/j.jnnfm.2012.10.002.

Di Federico, V. et al. (2014). "Radial gravity currents in vertically graded porous media: Theory and experiments for Newtonian and power-law fluids". In: *Advances in Water Resources* 70, pp. 65 –76. ISSN: 0309-1708. DOI: 10.1016/j.advwatres.2014.04.015.

Di Federico, V. et al. (2017). "Gravity-driven flow of Herschel-Bulkley fluid in a fracture and in a 2D porous medium". In: *Journal of Fluid Mechanics* 821, pp. 59–84. DOI: 10.1017/jfm.2017.234.

Dobriyal, Pariva et al. (2012). "A review of the methods available for estimating soil moisture and its implications for water resource management". In: *Journal of Hydrology* 458-459, pp. 110 –117.

Dobson, M. C. et al. (1985). "Microwave dielectric behavior of wet soil - Part II: dielectric mixing models". In: *IEEE Transactions on Geoscience and Remote Sensing* 33(3), pp. 803–807.

Dong, Xin, Mehmet C. Vuran, and Suat Irmak (2013). "Autonomous precision agriculture through integration of wireless underground sensor networks with center pivot irrigation systems". In: *Ad Hoc Networks* 11.7, pp. 1975 –1987. ISSN: 1570-8705.

EC (2003). *Common Implementation Strategy for the Water Framework Directive (2000/60/EC).* Guidance Document No.11. Planning Processes. Working Group 2.9. Office for the Official Publications of the European Communities, Luxembourg.: European Commission.

— (2007a). *Guidance on Groundwater in Drinking Water Protected Areas,* Guidance Document No. 16. Office for the Official Publications of the European Communities, Luxembourg: European Commission.

— (2007b). *Guidance on Groundwater Monitoring.* Guidance Document No. 15. Office for the Official Publications of the European Communities, Luxembourg: European Commission.

— (2007c). *Guidance on Preventing or Limiting Direct and Indirect Inputs in the context of the Groundwater Directive 2006/118/EC.* Guidance Document No 17. Office for the Official Publications of the European Communities, Luxembourg: European Commission.

EC (2009). *Guidance on groundwater status and trend assessment.* Guidance Document No. 18. Office for the Official Publications of the European Communities, Luxembourg: European Commission.

— (2010). *Guidance on risk assessment and the use of conceptual models for groundwater.* Guidance Document No. 26. Office for the Official Publications of the European Communities, Luxembourg: European Commission.

Elenius, M. T., D. V. Voskov, and H. A. Tchelepi (2015). "Interactions between gravity currents and convective dissolution". In: *Advances in Water Resources* 83, pp. 77 –88. ISSN: 0309-1708. DOI: `10.1016/j.advwatres.2015.05.006`.

EP (2000). *Directive 2000/60/EC of 23 October 2000 establishing a framework for Community action in the field of water policy.* Tech. rep. European Parliament and Council.

— (2006). *Directive 2006/118/EC of 12 December 2006 on the protection of groundwater against pollution and deterioration.* Tech. rep. European Parliament and Council.

EPA (1997). *Guiding principle for Monte Carlo Analysis.* Tech. rep. U. S. Environmental Protection Agency.

— (2000). *Risk Characterization handbook.* Tech. rep. U. S. Environmental Protection Agency.

ER (2015a). *DGR 1781/2015 - Aggiornamento del quadro conoscitivo di riferimento ai fini del riesame dei Piani di Gestione Distrettuali 2015-2021.* Tech. rep. All. 5 - VALUTAZIONE DELLO STATO DELLE ACQUE SOTTERRANEE (2010-2013). Regione Emilia-Romagna.

— (2015b). *DGR 1781/2015 - Aggiornamento del quadro conoscitivo di riferimento ai fini del riesame dei Piani di Gestione Distrettuali 2015-2021.* Tech. rep. All. 2 - Bilanci idrici. Regione Emilia-Romagna.

Ferri, D. and M. Marcaccio (2015). *Valutazione dello stato delle acque sotterranee 2010-2013.* Tech. rep. Arpa Emilia-Romagna.

Ghanem, R. G. and P. D. Spanos (1991). *Stochastic finite elements-a spectral approach.* Springer, Berlin.

Gleeson, T. et al. (2012). "Water balance of global aquifers revealed by groundwater footprint". In: *Nature, 488: 197-200.*

Guo, B. et al. (2016). "Flow regime analysis for geologic CO2 sequestration and other subsurface fluid injections". In: *International Journal of Greenhouse Gas Control* 53, pp. 284 –291. ISSN: 1750-5836. DOI: 10.1016/j.ijggc.2016.08.007.

Haas, C. N., J. Anotai, and R. S. Engelbrecht (1996). "Monte Carlo assessment of microbial risk associated with landfilling of fecal material." In: *Water Environ. Res.*

Harbaugh, A. W. (1990). *A Computer Program for Calculating Subregional Water Budgets Using Results from the U.S. Geological Survey Modular Three-dimensional Finite-difference Ground-water Flow Model.* Report 90-392. U.S. Geological Survey.

— (2005). *MODFLOW-2005, The U.S. Geological Survey Modular Ground-Water Model—the Ground-Water Flow Process.* Chapter 16 of Book 6. Modeling techniques, Section A. Ground Water. U.S. Geological Survey.

Hargreaves, G. H. and Z. A. Samani (1982). "Estimating potential evapotranspiration". In: *J. Irrig. and Drain Eng., 108: 223-230.*

Huang, Jingyi et al. (2017). "Monitoring and modelling soil water dynamics using electromagnetic conductivity imaging and the ensemble Kalman filter". In: *Geoderma* 285, pp. 76 –93. ISSN: 0016-7061.

Huang, S., S. Mahadevan, and R. Rebba (2007). "Collocation-based stochastic finite element analysis for random field problems". In: *Probabilistic Engineering Mechanics* 22, pp. 194–205.

Huber, E. J., A. D. Stroock, and D. L. Koch (2016). "Analysis of a time dependent injection strategy to accelerate the residual trapping of sequestered CO2 in the geologic subsurface". In: *International Journal of Greenhouse Gas Control* 44, pp. 185 –198. ISSN: 1750-5836. DOI: `10.1016/j.ijggc.2015.11.024`.

Huppert, H. E., J. A. Neufeld, and C. Strandkvist (2013). "The competition between gravity and flow focusing in two-layered porous media". In: *J. Fluid Mech.* 720, pp. 5–14. DOI: `10.1017/jfm.2012.623`.

Huppert, H. E. and A. W. Woods (1995). "Gravity-driven flows in porous layers". In: *J. Fluid Mech.* 292, pp. 55–69. DOI: `10.1017/S0022112095001431`.

IPCC (2015). *Climate Change 2014*. Synthesis Report. Intergovernmental Panel on Climate Change.

Islam, A. W. et al. (2016). "Numerical experiments of density driven {CO2} saturated brine migration in heterogeneous two-dimensional geologic fabric materials". In: *International Communications in Heat and Mass Transfer* 71, pp. 148 –156. ISSN: 0735-1933. DOI: `10.1016/j.icheatmasstransfer.2015.12.019`.

ISPRA (2016). *Criteri tecnici per l'analisi dello stato quantitativo e il monitoraggio dei corpi idrici sotterranei*. Manuali e Linee Guida

XXX/2016. Istituto Superiore per la Protezione e la Ricerca Ambientale.

Jang, W. et al. (2013). "Source Characterization and Simulation of the Migration of Light Nonaqueous Phase Liquids (LNAPLs) in the Vicinity of the Hadnot Point Industrial Area". In: *Analyses and Historical Reconstruction of Groundwater Flow, Contaminant Fate and Transport, and Distribution of Drinking Water Within the Service Areas of the Hadnot Point and Holcomb Boulevard Water Treatment Plants and Vicinities, U.S. Marine Corps Base Camp Lejeune, North Carolina–Chapter A: Summary and Findings*. Ed. by M. L. Maslia et al. Atlanta, GA: Agency for Toxic Substances and Disease Registry. Chap. Supplement 7.

Jiang, X. W., X.-S. Wang, and L. Wan (2010). "Semi-empirical equations for the systematic decrease in permeability with depth in porous and fractured media". In: *Hydrogeol. J.* 18(4), pp. 839–850. DOI: 10.1007/s10040-010-0575-3.

Jurado, A. et al. (2012). "Probabilistic analysis of groundwater-related risk at subsurface excavation sites". In: *Eng Geol.*

Kessler, J.H. and R. K. McGuire (1999). "Total system performance assessment for waste disposal using a logic tree approach". In: *Risk Analysis*.

Kounina, A. et al. (2013). "Review of methods addressing freshwater use in life cycle inventory and impact assessment". In: *Int J Life Cycle Assessment, 18:707-721*.

Lahkim, M. B. and L. A. Garcia (1999). "Stochastic modeling of exposure and risk in a contaminated heterogeneous aquifer. 1: Monte Carlo uncertainty analysis." In: *Environ Eng Sci.*

Lahkim, M. B., L. A. Garcia, and J. R. Nuckols (1999). "Stochastic modeling of exposure and risk in a contaminated heterogenous aquifer. 2: Application of Latin Hypercube sampling". In: *Environ Eng Sci*.

Laloy, E. et al. (2013). "Efficient posterior exploration of a high - dimensional groundwater model from two-stage Markov Chain Monte Carlo simulation and polynomial chaos expansion". In: *Water. Resour. Res* 49, pp. 2664–2682.

Lauriola, I., V. Ciriello, and M. Marcaccio (2015). "Dinamiche di ricarica nella conoide del Trebbia". In: *ECOSCIENZA* N.2.

Legislative Directive (2010). *D. Lgs. 152/2006 Decreto Legislativo n. 152 del 03/04/2006 (Norme inmateria ambientale) come modificato ed integrato dal D. Lgsn. 128 del 29/06/2010 (Modifiche ed integrazioni al decretolegislativo n. 152 del 03/04/2006, recante norme in materiaambientale (in Italian)*. Roma.

Li, L., M. C. Vuran, and I. F. Akyildiz (2007). "Characteristics of underground channel for wireless underground sensor networks". In: vol. Med-Hoc-Net '07, Corfu, Greece. P. 95.

Lin, G., A. M. Tartakovsky, and D. M. Tartakovsky (2010). "Uncertainty quantification via random domain decomposition and probabilistic collocation on sparse grids". In: *J. Comput. Phys.* 229, pp. 6995–7012.

Linkov, I. and D. Burmistrov (2003). "Model uncertainty and choices made by modelers: lesson learned from the international atomic energy agency model intercomparisons". In: *Risk Analysis* Vol.23.No.6, p. 1297–1308.

Longo, S. et al. (2013b). "Experimental verification of power-law non-Newtonian axisymmetric porous gravity currents". In: *J. Fluid Mech.* 731, R2, pp. 1–12. DOI: `10.1017/jfm.2013.389`.

Longo, S. et al. (2015). "Combined effect of rheology and confining boundaries on spreading of porous gravity currents". In: *Advances in Water Resources* 79, pp. 140–152. DOI: `10.1016/j.advwatres.2015.02.016`.

Lyle, S. et al. (2005). "Axisymmetric gravity currents in a porous medium". In: *J. Fluid Mech.* 543, pp. 293–302. DOI: `10.1017/S0022112005006713`.

Maji, R. and E. A. Sudicky (2008). "Influence of mass transfer characteristics for DNAPL source depletion and contaminant flux in a highly characterized glaciofluvial aquifer". In: *J. Contam. Hydrol.* 102.1, pp. 105–119. DOI: `j.jconhyd.2008.08.005`.

Marrel, A., N. Perot, and C. Mottet (2015). "Development of a surrogate model and sensitivity analysis for spatio-temporal numerical simulators". In: *Stoch. Environ. Res. Risk. Assess.* 29.3, pp. 959–974.

Martínez-Fernández, J. et al. (2015). "A soil water based index as a suitable agricultural drought indicator". In: *Journal of Hydrology* 522, pp. 265 –273. ISSN: 0022-1694.

McLaren, R. et al. (2012). "Numerical simulation of DNAPL emissions and remediation in a fractured dolomitic aquifer". In: *J. Contam. Hydrol.* 136-137, pp. 56–71.

Moghadas, Davood, Khan Zaib Jadoon, and Matthew F. McCabe (2017). "Spatiotemporal monitoring of soil water content profiles in an irrigated field using probabilistic inversion of time-lapse EMI

data". In: *Advances in Water Resources* 110, pp. 238 –248. ISSN: 0309-1708.

Moon, Y. I., B. Rajagopalan, and U. Lall (1995). "Estimation of mutual information using Kernel density estimators". In: *Physical Review E*.

Narasimhan, B. and R. Srinivasan (2005). "Development and evaluation of Soil Moisture Deficit Index (SMDI) and Evapotranspiration Deficit Index (ETDI) for agricultural drought monitoring". In: *Agricultural and Forest Meteorology* 133.1, pp. 69 –88. ISSN: 0168-1923.

Ngo, T. D., E. Mouche, and P. Audigane (2016). "Buoyant flow of CO_2 through and around a semi-permeable layer of finite extent". In: *Journal of Fluid Mechanics* 809, pp. 553–584. DOI: `10.1017/jfm.2016.684`.

NRC (1997). *Review of Recommendations for Probabilistic Seismic Hazard Analysis: Guidance on Uncertainty and Use of Experts*. Tech. rep. US National Research Council.

— (2010). *Safety Evaluation Report Related to Disposal of High-Level Radioactive Wastes in a Geological Repository at Yucca Mountain, Nevada*. Tech. rep. US Nuclear Regulatory Commission.

OECD (1997). *Report of the OECD Workshop on Pipelines (Prevention of, Preparedness for, and Response to Releases of Hazardous Substances), Series on Chemical Accidents n.2, Paris*. Tech. rep. OECD.

Pascal, H. (1983). "Nonsteady flow of non-Newtonian fluids through a porous medium". In: *Int. J. Eng. Sci.* 21, pp. 199–210. DOI: `10.1016/0020-7225(83)90021-6`.

Pattle, R. E. (1959). "Diffusion from an instantaneous point source with a concentration - dependent coefficient". In: *Q. J. Mechanics Appl. Math.* 4, pp. 407–409. DOI: `10.1093/qjmam/12.4.407`.

Pegler, S. S., H. E. Huppert, and J. A. Neufeld (2016). "Stratified gravity currents in porous media". In: *Journal of Fluid Mechanics* 791, pp. 329–357. DOI: `10.1017/jfm.2015.733`.

Peplinski, N. R., F. T. Ulaby, and M. C. Dobson (1995). "Dielectric properties of soils in the 0.3–1.3-GHz range". In: *IEEE Transactions on Geoscience and Remote Sensing* 33(3), pp. 803–807.

Rajabi, M. M., B. Ataie-Ashtiani, and C. T. Simmons (2015). "Polynomial chaos expansions for uncertainty propagation and moment independent sensitivity analysis of seawater intrusion simulations". In: *J. Hydrol.* 520, pp. 101–122.

Rodak, C. and S. Silliman (2011). "Probabilistic risk analysis and fault trees: initial discussion of application to identification of risk at a wellhead". In: *Adv Water Resour*.

Rubin, Y. (2003). *Applied Stochastic Hydrogeology*. Oxford Univ. Press, New York.

Sahu, C. K. and M. R. Flynn (2017). "The Effect of Sudden Permeability Changes in Porous Media Filling Box Flows". In: *Transport in Porous Media* 119.1, pp. 95–118. ISSN: 1573-1634. DOI: `10.1007/s11242-017-0875-3`.

Saltelli, A., S. Tarantola, and F. Campolongo (2000). "Sensitivity analysis as an ingredient of modeling". In: *Stat. Sci.* 15.4, pp. 377–395.

Sheffield, J. and E. F. Wood (2008). "Global Trends and Variability in Soil Moisture and Drought Characteristics, 1950–2000, from

Observation-Driven Simulations of the Terrestrial Hydrologic Cycle". In: *Journal of Climate* 21.3, pp. 432–458.

Shenoy, A. V. (1995). "Non-Newtonian fluid heat transfer in porous media". In: *Adv. Heat Trans.* 24, pp. 102–190. DOI: 10.1016/S0065-2717(08)70233-8.

Sinsbeck, M. and D. M. Tartakovsky (2015). "Impact of data assimilation on cost-accuracy tradeoff in multifidelity models". In: *SIAM/ASA J. Uncert. Quant.* 3.1, pp. 954–968. DOI: 10.1137/141001743.

Skaggs, T. H. and D. H. Barry (1997). "The first-order reliability method of predicting cumulative mass flux in heterogeneous porous formations." In: *Water Resour Res.*

Slider, H. C. (1983). *Worldwide practical petroleum reservoir engineering methods*. PennWell Books.

Smakhtin, V., C. Revenga, and P. Döll (2004). "A pilot global assessment of environmental water requirements and scarcity". In: *Water Int., 29, 307–317.*

Sobol', I. M. (1993). "Sensitivity estimates for nonlinear mathematical models". In: *Math. Modeling Comput.* 1, pp. 407–414.

— (2001). "Global sensitivity indices for nonlinear mathematical models and their Monte Carlo estimates". In: *Math. Comput. Simulation* 55, pp. 271–280.

Sudicky, E. A. et al. (2013). "A semi-analytical solution for simulating contaminant transport subject to chain-decay reactions". In: *J. Contam. Hydrol.* 144.1, pp. 20–45.

Sudret, B. (2008). "Global sensitivity analysis using polynomial chaos expansions". In: *Reliab. Eng. Syst. Safety* 93, pp. 964–979.

Tartakovsky, D. M. (2007). "Probabilistic risk analysis in subsurface hydrology". In: *Geophys. Res. Lett.* 34(5), p. L05404.

Tartakovsky, D. M (2013). "Assessment and management of risk in subsurface hydrology: A review and perspective". In: *Adv. Water Resour.* 51, pp. 247–260.

Tartakovsky, D. M., A. Guadagnini, and M. Riva (2003). "Stochastic averaging of nonlinear flows in heterogeneous porous media". In: *J. Fluid Mech.* 492, pp. 47–62. DOI: 10.1017/S002211200300538X.

Tartakovsky, D. M., S. P. Neuman, and Z. Lu (1999). "Conditional stochastic averaging of steady state unsaturated flow by means of Kirchhoff transformation". In: *Water Resour. Res.* 35.3, pp. 731–745.

TNO (1999). *Committee for the Prevention of Disasters, Guidelines for Quantitative Risk Assessment CPR18E*. Tech. rep. Sdu Uitgevers. The Hague.

Troldborg, M. et al. (2008). "Risk assessment and prioritisation of contaminated sites on the catchment scale". In: *J Contam Hydrol.*

Tsakiris, G., D. Pangalou, and H. Vangelis (2007). "Regional drought assessment based on the Reconnaissance Drought Index (RDI)". In: *Water Resour. Manage.* 21.5, pp. 821–833.

Tsakiris, G. and H. Vangelis (2005). "Establishing a drought index incorporating evapotranspiration". In: *European Water* 9.10, pp. 3–11.

UNESCO (1979). *Map of the world distribution of arid regions*. Tech. rep. The United Nations Educational, Scientific and Cultural Organization (UNESCO).

Ungarish, M. (2009). *An Introduction to Gravity Currents and Intrusions*. CRC Press.

Unwin, H. G. T., G. N. Wells, and A. W. Woods (2016). "CO_2 dissolution in a background hydrological flow". In: *Journal of Fluid Mechanics* 789, pp. 768–784. DOI: 10.1017/jfm.2015.752.

Vella, D. and H. E. Huppert (2006). "Gravity currents in a porous medium at an inclined plane". In: *J. Fluid Mech.* 555, pp. 353–362. DOI: 10.1017/S0022112006009578.

Vesely, W. E. and N. H. Roberts (1981). *Fault Tree Handbook*. Tech. rep. US Nuclear Regulatory Commission.

Vörösmarty, C. J. et al. (2000). "Global water resources: vulnerability from climate change and population growth". In: *Science, 289, 284*.

Vörösmarty, C. J. et al. (2005). "Geospatial Indicators of Emerging Water Stress: An Application to Africa, AMBIO". In: *A Journal of the Human Environment 34(3):230-236*.

Vuran, M. C. and A. R. Silva (2009). "Communication through soil in wireless underground sensor networks–theory and practice". In: *Sensor Networks*, pp. 309–318.

Wada, Y. et al. (2010). "Global depletion of groundwater resources". In: *Geophys. Res. Lett., 37, L20402*.

Weaver, J. W. et al. (1994). *The Hydrocarbon Spill Screening Model (HSSM) Volume1: User's Guide*. Tech. rep. EPA/600/R-94/039a. US Environmental Protection Agency.

Webster, M., M. A. Tatang, and G. J. McRae (1996). *Application of the probabilistic collocation method for an uncertainty analysis of a simple ocean model*. Tech. rep. MIT joint program on the science

and policy of global change reports series No. 4. Cambridge, MA: MIT.

Wiener, N. (1938). "The homogeneous chaos". In: *Am. J. Math.* 60, pp. 897–936.

Winter, C. L. and D. M. Tartakovsky (2000). "Mean flow in composite porous media". In: *Geophys. Res. Lett.* 27.12, pp. 1759–1762.

Xiu, D. and G. E. Karniadakis (2002). "The Wiener-Askey polynomial chaos for stochastic differential equations". In: *J. Sci. Comput.* 24(2), pp. 619–644.

Yoon, H. et al. (2009). "An environmental screening model to assess the consequences to soil and groundwater from railroad-tank-car spills of light non-aqueous phase liquids". In: *J. Hazard. Mater.* 165, pp. 332–344.

Yu, Y. E., Z. Zheng, and H. A. Stone (2017). "Flow of a gravity current in a porous medium accounting for drainage from a permeable substrate and an edge". In: *Phys. Rev. Fluids* 2 (7), p. 074101. DOI: `10.1103/PhysRevFluids.2.074101`.

Zhang, Y., P. Vouzis, and N. V. Sahinidis (2011). "GPU simulations for risk assessment in CO2 geologic sequestration." In: *Comput Chem Eng.*

Zheng, Z., I. C. Christov, and H. A. Stone (2014). "Influence of heterogeneity on second-kind self-similar solutions for viscous gravity currents". In: *J. Fluid Mech.* 747, pp. 218–246. DOI: `10.1017/jfm.2014.148`.

Zheng, Z. et al. (2013). "Fluid drainage from the edge of a porous reservoir". In: *J. Fluid Mech.* 718, pp. 558–568. DOI: `10.1017/jfm.2012.630`.